

# Advances in Low-Profile Antennas in Wireless Communications 2015

Guest Editors: Guo Qing Luo, Xiao Ping Chen, Zhang Cheng Hao, Bing Liu,  
and Yu Jian Cheng



---



# **Advances in Low-Profile Antennas in Wireless Communications 2015**

International Journal of Antennas and Propagation

---

## **Advances in Low-Profile Antennas in Wireless Communications 2015**

Guest Editors: Guo Qing Luo, Xiao Ping Chen,  
Zhang Cheng Hao, Bing Liu, and Yu Jian Cheng



---

Copyright © 2015 Hindawi Publishing Corporation. All rights reserved.

This is a special issue published in "International Journal of Antennas and Propagation." All articles are open access articles distributed under the Creative Commons Attribution License, which permits unrestricted use, distribution, and reproduction in any medium, provided the original work is properly cited.

## Editorial Board

- |                                 |                                  |                                 |
|---------------------------------|----------------------------------|---------------------------------|
| Ana Alejos, Spain               | Flaminio Ferrara, Italy          | N. Nasimuddin, Singapore        |
| Mohammod Ali, USA               | Vincenzo Galdi, Italy            | Miguel Navarro-Cia, UK          |
| Jaume Anguera, Spain            | Claudio Gennarelli, Italy        | Mourad Nedil, Canada            |
| Rodolfo Araneo, Italy           | Sotirios K. Goudos, Greece       | Symeon Nikolaou, Cyprus         |
| Ercument Arvas, USA             | Rocco Guerriero, Italy           | Giacomo Oliveri, Italy          |
| Alexei Ashikhmin, USA           | Kerim Guney, Turkey              | Pablo Otero, Spain              |
| Herve Aubert, France            | Song Guo, Japan                  | Athanasiос Panagopoulos, Greece |
| Paolo Baccarelli, Italy         | Mohamed Himdi, France            | Ikmo Park, Korea                |
| Xiulong Bao, Ireland            | Tamer S. Ibrahim, USA            | Josep Parrón, Spain             |
| Toni Björninen, Finland         | Mohammad Islam, Malaysia         | Matteo Pastorino, Italy         |
| Stefania Bonafoni, Italy        | M. R. Kamarudin, Malaysia        | Massimiliano Pieraccini, Italy  |
| Djuradj S. Budimir, UK          | Kyeong Jin Kim, USA              | Xianming Qing, Singapore        |
| Paolo Burghignoli, Italy        | Ahmed A. Kishk, Canada           | Ahmad Safaai-Jazi, USA          |
| Shah N. Burokur, France         | Slawomir Koziel, Iceland         | Safieddin Safavi-Naeini, Canada |
| Giuseppe Castaldi, Italy        | Luis Landesa, Spain              | Magdalena Salazar-Palma, Spain  |
| Felipe Cátedra, Spain           | Ding-Bing Lin, Taiwan            | Stefano Selleri, Italy          |
| Marta Cavagnaro, Italy          | Angelo Liseno, Italy             | John J. Shynk, USA              |
| Deb Chatterjee, USA             | Pierfrancesco Lombardo, Italy    | Prabhakar Singh, India          |
| Shih Yuan Chen, Taiwan          | Giampiero Lovat, Italy           | Raffaele Solimene, Italy        |
| Yu Jian Cheng, China            | Lorenzo Luini, Italy             | Gino Sorbello, Italy            |
| Renato Cicchetti, Italy         | Atsushi Mase, Japan              | Seong-Youp Suh, USA             |
| Lorenzo Crocco, Italy           | Diego Masotti, Italy             | Sheng Sun, Hong Kong            |
| Claudio Curcio, Italy           | David W. Matolak, USA            | Larbi Talbi, Canada             |
| Francesco D'Agostino, Italy     | Giuseppe Mazzarella, Italy       | Luciano Tarricone, Italy        |
| Maria E. De Cos, Spain          | C. F. Mecklenbräuker, Austria    | Parveen Wahid, USA              |
| Tayeb A. Denidni, Canada        | Massimo Migliozi, Italy          | Yuanxun Ethan Wang, USA         |
| Giuseppe Di Massa, Italy        | Mark Mirotznik, USA              | Wen-Qin Wang, China             |
| Michele D'Urso, Italy           | Ahmed T. Mobashsher, Australia   | Shiwen Yang, China              |
| Hala A. Elsadek, Egypt          | Ananda S. Mohan, Australia       | Yuan Yao, China                 |
| Francisco Falcone, Spain        | J.-M. Molina-Garcia-Pardo, Spain | Jingjing Zhang, Denmark         |
| Miguel Ferrando Bataller, Spain | Marco Mussetta, Italy            |                                 |

## Contents

**Advances in Low-Profile Antennas in Wireless Communications 2015**, Guo Qing Luo, Xiao Ping Chen, Zhang Cheng Hao, Bing Liu, and Yu Jian Cheng  
Volume 2015, Article ID 356245, 2 pages

**Substrate Integrated Waveguide Leaky-Wave Antenna Conforming to Conical Shape Surface**, W. N. Huang, Y. J. Cheng, and H. Deng  
Volume 2015, Article ID 359670, 7 pages

**Gain Enhancement of a Microstrip Patch Antenna Using a Reflecting Layer**, Anwer Sabah Mekki, Mohd Nizar Hamidon, Alyani Ismail, and Adam R. H. Alhawari  
Volume 2015, Article ID 975263, 7 pages

**Novel Miniaturized Octaband Antenna for LTE Smart Handset Applications**, Haixia Liu, Bo Lu, and Long Li  
Volume 2015, Article ID 861016, 8 pages

**Equilateral Triangular Dielectric Resonator Nantenna at Optical Frequencies for Energy Harvesting**, Waleed Tariq Sethi, Hamsakutty Vettikalladi, Habib Fathallah, and Mohamed Himdi  
Volume 2015, Article ID 589459, 10 pages

**A Multiple Resonant Frequencies Circular Reconfigurable Antenna Investigated with Wireless Powering in a Concrete Block**, Shishir Shanker Punjala, Niki Pissinou, and Kia Makki  
Volume 2015, Article ID 413642, 9 pages

**High Gain Superstrate Loaded Membrane Antenna Based on Substrate Integrated Waveguide Technology**, Hamsakutty Vettikalladi  
Volume 2015, Article ID 385125, 8 pages

**A Miniaturized Triple Band Monopole Antenna for WLAN and WiMAX Applications**, Yingsong Li and Wenhua Yu  
Volume 2015, Article ID 146780, 5 pages

**A Low-Profile and Compact Split-Ring Antenna with Horizontally Polarized Omnidirectional Radiation**, Kittima Lertsakwimarn, Chuwong Phongcharoenpanich, and Takeshi Fukusako  
Volume 2015, Article ID 954562, 11 pages

## Editorial

# Advances in Low-Profile Antennas in Wireless Communications 2015

**Guo Qing Luo,<sup>1</sup> Xiao Ping Chen,<sup>2</sup> Zhang Cheng Hao,<sup>3</sup> Bing Liu,<sup>4</sup> and Yu Jian Cheng<sup>5</sup>**

<sup>1</sup>School of Electronics and Information, Hangzhou Dianzi University, Hangzhou 310018, China

<sup>2</sup>Poly-Grames Research Centre, Department of Electrical Engineering, University of Montreal, Montreal, QC, Canada H3T 1J4

<sup>3</sup>School of Information Science and Engineering, Southeast University, Nanjing 210096, China

<sup>4</sup>College of Electronic and Information Engineering, Nanjing University of Aeronautics and Astronautics, Nanjing 210016, China

<sup>5</sup>School of Electronic Engineering, University of Electronic Science and Technology of China, Chengdu 611731, China

Correspondence should be addressed to Guo Qing Luo; gqluo@emfield.org

Received 7 September 2015; Accepted 7 September 2015

Copyright © 2015 Guo Qing Luo et al. This is an open access article distributed under the Creative Commons Attribution License, which permits unrestricted use, distribution, and reproduction in any medium, provided the original work is properly cited.

Although low-profile antennas designs have been widely studied in the past years, there are still many challenging issues in low-profile antennas in wireless communications. In this special issue, the accepted papers include the designs of multiple frequency antenna, conformal substrate integrated waveguide (SIW) antenna, membrane antenna, reconfigurable antenna, on-chip antenna, and handset antenna. Their operating frequency ranges cover from several hundred MHz to several hundred THz.

T. Fukusako (Kumamoto University of Japan) and colleagues proposed a low-profile and compact printed antenna having an omnidirectional radiation pattern with horizontal polarization to the ground. The proposed antenna consists of an inner small fed ring, an outer coupled split ring, and a ground plane. The proposed antenna covers the 920 MHz RFID band, and its gain is 1.45 dBi in the parallel direction to the ground plane.

H. Liu et al. (Xidian University of China) proposed a novel octaband LTE mobile phone antenna. The miniaturized octaband antenna is implemented by a simple prototype of three parts which include a folded monopole as feeding element, main radiator element, and parasitic radiator element. The main and parasitic radiator elements are excited by the folded monopole feeding element coupling and shorting to the handset ground plane. The antenna has the total efficiency up to 30% in low bands and up to 75% in high bands, respectively.

A. S. Mekki et al. (Universiti Putra Malaysia of Malaysia) proposed a gain enhanced and size reduced microstrip patch antenna. The proposed unidirectional and low-profile microstrip patch antenna of  $0.069\lambda_0$  operates at 2.45 GHz and has an impedance bandwidth of 2%, a gain of 5.2 dBi, and a front to back ratio of 9.5 dB.

Y. Li (Harbin Engineering University of China) and W. Yu proposed a miniaturized triple band monopole antenna for microwave access (WiMAX) and wireless local area network (WLAN) communication applications. Its three resonance frequencies are realized by using a toothbrush-shaped patch (TSP), a meander line (ML), and an inverted U-shaped patch (IUSP). The center frequencies of the triple bands can be controlled by adjusting the dimensions of the TSP, ML, and IUSP, respectively.

S. S. Punjala (Tata Consultancy Services of India) and colleagues proposed a novel broadband reconfigurable antenna covering different frequency bands for wireless powering application in a concrete block. The reconfigurable antenna contains a circular patch, three concentric circular rings around the circular patch, and RF MEMS switches connected to the neighbored circular rings.

W. N. Huang et al. (University of Electronic Science and Technology of China) proposed a conical conformal leaky-wave antenna based on SIW technology. This antenna conforms to a conical shape surface with the angle of 40°. It has a narrow beam that scans from 80° to 97° with varying frequency from 34 GHz to 37 GHz.

H. Vettikalladi from King Saud University of Saudi Arabia proposed a single slot coupled SIW fed membrane antenna loaded with a superstrate layer for 94 GHz communication system. The membrane antenna consists of 6 layers. The microstrip patch antenna (MPA) placed on the top substrate layer is excited by means of a longitudinal rectangular slot placed over the SIW structure in the bottom substrate. The maximum gain achieved is 14.4 dBi with an efficiency of 77.6% at 94 GHz.

M. Himdi (University of Rennes of France) and colleagues proposed an equilateral triangular dielectric resonator nanoantenna at optical frequencies for solar energy harvesting application. The proposed antenna is composed of an “Ag-SiO<sub>2</sub>-Ag” structure with a nanosilver “Ag” transmission line that excites a triangular dielectric made of “Si” material. It has a wide impedance bandwidth of 2.58% with a high directive radiation pattern of 8.6 dBi at 193.5 THz with an end-fire radiation pattern.

We hope that, through this special issue, the readers will find not only new designs about different low-profile antennas but also their valuable applications.

## Acknowledgment

The editors thank all the contributors and the anonymous reviewers for their contributions to this special issue.

*Guo Qing Luo  
Xiao Ping Chen  
Zhang Cheng Hao  
Bing Liu  
Yu Jian Cheng*

## Research Article

# Substrate Integrated Waveguide Leaky-Wave Antenna Conforming to Conical Shape Surface

W. N. Huang,<sup>1</sup> Y. J. Cheng,<sup>1,2</sup> and H. Deng<sup>1</sup>

<sup>1</sup> Fundamental Science on Extreme High Frequency Laboratory, School of Electronic Engineering, University of Electronic Science and Technology of China, Chengdu 611731, China

<sup>2</sup> State Key Laboratory of Millimeter Waves, Southeast University, Nanjing 210096, China

Correspondence should be addressed to Y. J. Cheng; [yjcheng@emfield.org](mailto:yjcheng@emfield.org)

Received 28 August 2014; Accepted 22 October 2014

Academic Editor: Guo Qing Luo

Copyright © 2015 W. N. Huang et al. This is an open access article distributed under the Creative Commons Attribution License, which permits unrestricted use, distribution, and reproduction in any medium, provided the original work is properly cited.

A conical conformal leaky-wave antenna based on substrate integrated waveguide (SIW) technology is proposed and demonstrated in this paper. This antenna conforms to a conical shape surface with the angle of 40°. It has a narrow beam that scans from 80° to 97° with varying frequency (34 GHz~37 GHz). Both conformal and nonconformal antennas are fabricated through the standard PCB process. Their performances are compared within the desired frequency.

## 1. Introduction

Conformal antennas have been of wide interest to scholars due to the purpose of integrating with the structures such as part of airplane, train, or other vehicles. The theory and design of conformal antennas are fully described in [1]. Different surfaces can be used in conformal antennas, such as a cylindrical shape, a conical shape, and a spherical shape. Among them, the conical shape surface can be of special interest for applications in the noses of missile, aircraft, and instrument.

As is well known, leaky-wave antennas are a member of the family of traveling-wave antennas that permit the power leaking along one of their sides, and the radiation patterns can be scanned by varying frequency [2]. Many researchers have studied numerous types of leaky-wave antennas. The leaky-wave antenna in [3] generates leakage when the period length between the vias is sufficiently large. A leaky-wave antenna based on the half-mode substrate integrated waveguide (HMSIW) discussed in [4] possesses the qualities of compact size, wide bandwidth, and quasi-omnidirectional radiation pattern. The long slot leaky-wave antenna [5] has the controllable side lobe level by changing the position of vias in its sidewall. A microstrip leaky-wave antenna (MLWA) performance on a curved surface [6] provides an alternative

to the traditional resonant microstrip antennas. A fixed-frequency beam-scanning MLWA array [7] has the capability of scanning the main lobe continuously at the fixed frequency by controlling the relative phase between two elements. An HMSIW leaky-wave antenna with a series of ±45° slots published in [8] can provide four states of polarization (linear or circular) according to the different input ports. A novel leaky-wave antenna with transverse slots is proposed in [9] that has the advantage of scanning to endfire. It radiates from a periodic set of transverse slots on the top of the substrate. The leaky-wave antenna designed on a composite right/left-handed (CRLH) SIW [10] has beam scanning from the backward to the forward direction and operates in two frequency bands. A low temperature cofired ceramic (LTCC) leaky-wave antenna based on the substrate integrated image guide (SIIG) is realized in [11], and it has both the simplicity in designing procedures and better fabrication reliability.

The conformal leaky-wave antenna has a simple structure, high efficiency, and ability of frequency scanning. Therefore, some useful conformal leaky-wave antennas have been introduced. The cylindrical microstrip leaky-wave antennas implemented in [12] have the high gain and wide bandwidth, similar to those of the planar ones. A novel theory to analyze and design tapered conformal leaky-wave antennas [13] shows how it can maintain the desired high-directive

scanning performance in spite of the curved shape. By comparing among the nontapered rectilinear antenna, nontapered conformal antenna, and the tapered conformal antenna [14], it presents how the antenna width needs to be tapered along the antenna length to properly synthesize the complex propagation constant and therefore to produce a desired radiation pattern.

As a new guided-wave structure, substrate integrated waveguide (SIW) has attractive advantages including low loss, low cost, easy fabrication, and convenient integration with planar circuit [15–17]. Meanwhile, SIW has the good conformability and full-closed topology to avoid the unwanted leakage, which is a great impetus for the deployment of millimeter-wave integrated conformal array antennas [18]. In this work, a SIW leaky-wave antenna conforming to a conical shape surface with the angle of 40° is introduced. It is fed by the standard WR-28 waveguide. The antenna is designed and simulated using the full-wave simulation software Ansoft HFSS. S-parameter and radiation patterns are also investigated. The experimental results agree well with simulations.

## 2. Conformal SIW Leaky-Wave Antenna Design

The prototype SIW leaky-wave antenna is shown in Figure 1(a). The antenna leaks power through the SIW side wall by changing the window gap  $p$  [3]. This antenna is embedded in a conical base as shown in Figure 1(b). The conformal cone has the angle of  $\theta_c = 40^\circ$ ; the conformal beam direction is in the  $xoy$  plane (about theta = 90°). To realize this, the leaky-wave antenna should have the beam direction of  $\theta_0 = 130^\circ$  (the angle between the  $z$ -axis and the beam direction in Figure 1(a)). Here, the antenna radiates at the backward direction.

Firstly, the leaky-wave antenna will be designed. The substrate used here is the Rogers 5880 substrate with the thickness of 1.575 mm, the relative permittivity of 2.2, and the loss tangent of 0.0009. The main parameters of the leaky-wave antenna are the SIW width,  $l_1$ , the distance between the leaky-wave part and the edge of the substrate,  $l_2$ , the length of the leaky-wave part,  $l_3$ , and the leaky-wave window gap,  $p = l_3/n$ , where  $n$  is the number of windows. The designed frequency is at 35 GHz.

The complex propagation constant of the leaky-wave antenna is

$$k = \beta - j\alpha, \quad (1)$$

where  $\alpha$  is the leakage rate and  $\beta$  is the leaky-mode phase constant. The beam direction of the leaky-wave antenna mainly depends on  $\beta$  [2]. Consider

$$\sin \theta_m = \frac{\beta}{k_0}. \quad (2)$$

In (2),  $\theta_m = \theta_0 - 90^\circ$ . The desired beam direction can be realized when changing  $\beta$  appropriately. The radiation efficiency

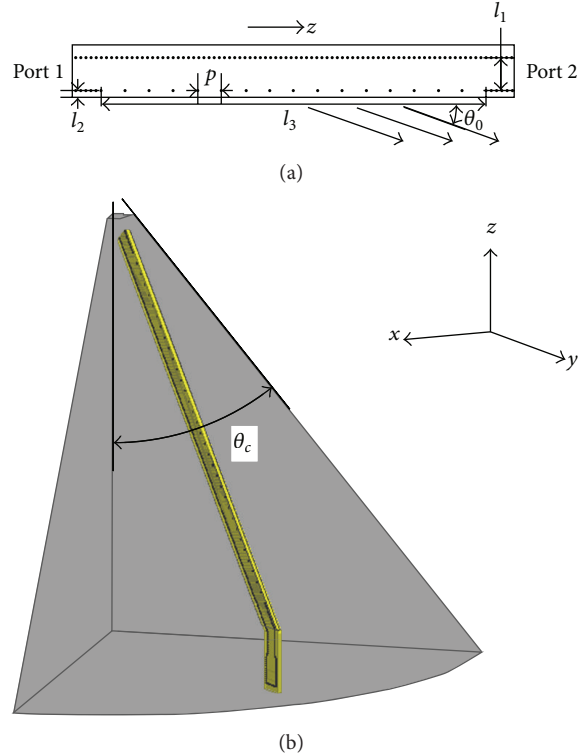


FIGURE 1: (a) Configuration of the SIW leaky-wave antenna. (b) Configuration of the conformal SIW leaky-wave antenna.

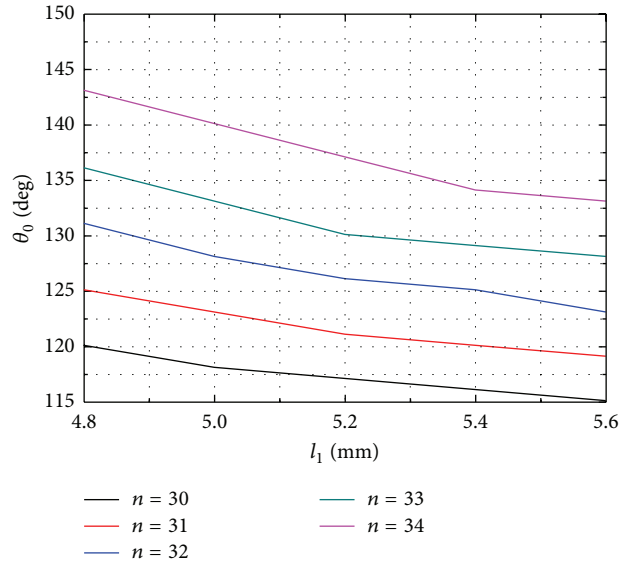


FIGURE 2: The window gap  $p = l_3/n$  versus beam direction  $\theta_0$ .

due to the absorbed load directly depends on the normalized leakage rate  $\alpha/k_0$  and the leaky-wave part length  $l_3$

$$e^r = 1 - e^{-2\alpha l_3} = 1 - e^{-4\pi(\alpha/k_0)(l_3/\lambda_0)}. \quad (3)$$

A typical choice for the radiation efficiency is 90%.

For the proposed antenna,  $\alpha$  and  $\beta$  can be easily controlled by changing the parameters  $l_1$  and  $p$ . Figures 2, 3, 4,

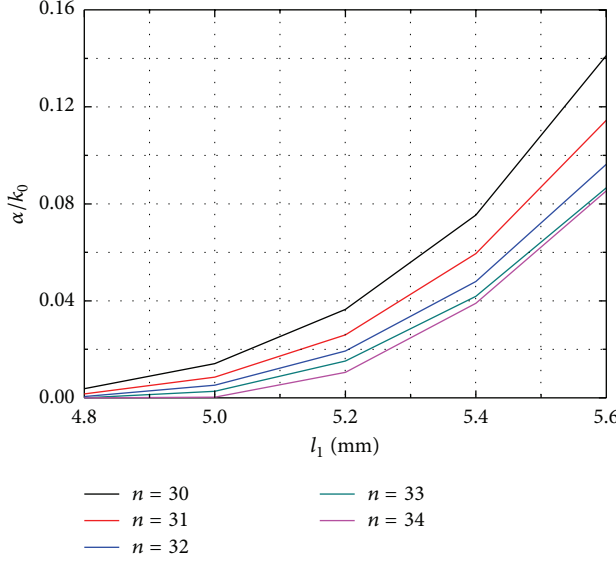


FIGURE 3: The window gap  $p = l_3/n$  versus normalized leakage rate  $\alpha/k_0$ .

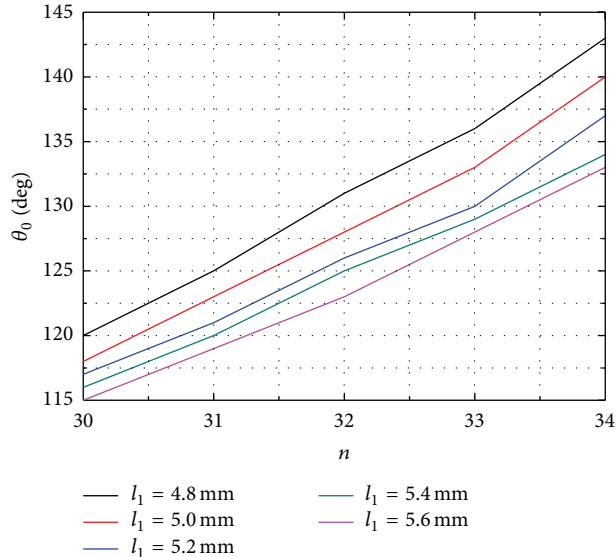


FIGURE 4: The SIW width  $l_1$  versus beam direction  $\theta_0$ .

and 5 show the performances of  $\alpha/k_0$  and  $\theta_0$  when  $p$  and  $l_1$  are varied. In order to avoid the appearance of undesired channel modes,  $l_2$  is usually set to less than  $\lambda/4$  [2]. The length  $l_3$  mainly influences the radiation efficiency due to the absorbed load. The relationship between  $l_3$  and radiation efficiency is listed in Table 1.

To synthesize the desired radiation properties, we finally choose the parameters of leaky-wave antenna as follows:  $l_1 = 5.2$  mm,  $l_2 = 1$  mm,  $l_3 = 150$  mm, and  $p = 4.54$  mm ( $n = 33$ ). The beam direction of single antenna is  $130^\circ$ . As shown in Figure 6,  $S_{21}$  of such a two-port antenna is below  $-13$  dB within  $34\sim37$  GHz. Considering 95% energy leaking along

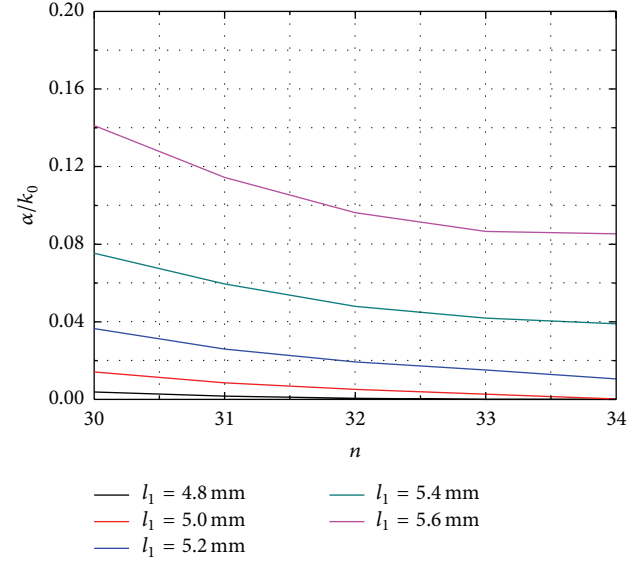


FIGURE 5: The SIW width  $l_1$  versus normalized leakage rate  $\alpha/k_0$ .

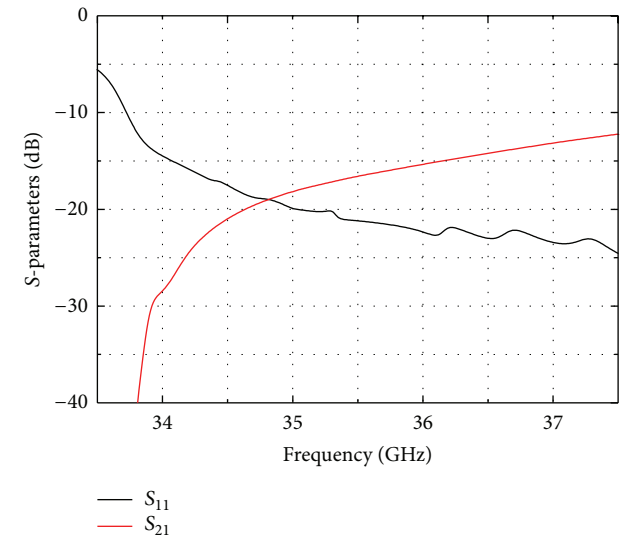


FIGURE 6: Simulated S-parameter of the designed two-port leaky-wave antenna.

TABLE 1: Length  $l_3$  versus radiation efficiency.

Length $l_3$ (mm)	Radiation efficiency (%)
80	84.5
100	88.9
150	93.2
200	94.4

SIW, only one port architecture is used in the later simulation and fabrication.

The designed one-port leaky-wave antenna is conformed to the cone. A long groove is cut on the surface of cone, and the antenna is inserted into the groove. The S-parameter and radiation patterns of the conformal and nonconformal

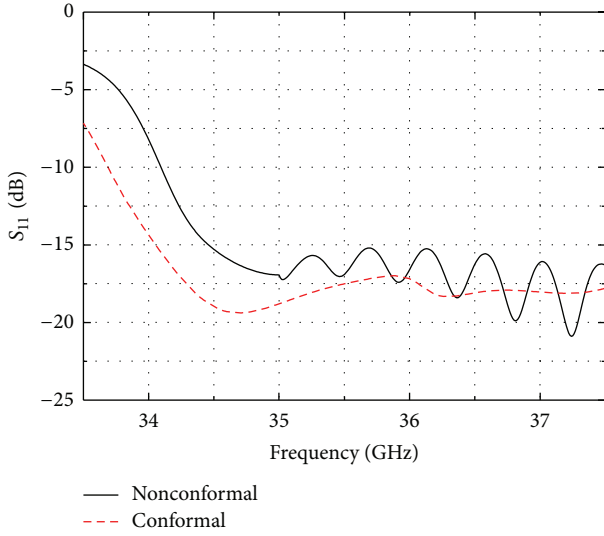


FIGURE 7: Simulated S-parameter of the designed conformal and nonconformal one-port antenna.

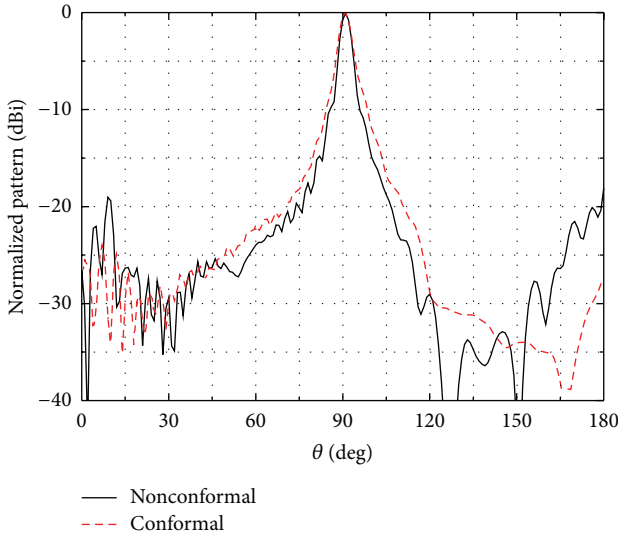


FIGURE 8: Simulated radiation pattern of the designed conformal and nonconformal antenna in the elevation plane.

antennas are compared in Figures 7, 8, and 9. As shown in Figure 7, their  $S_{11}$  are almost below  $-10$  dB within  $34\sim37$  GHz. The conformal gain ( $15.5$  dBi) is higher than the nonconformal one ( $15.2$  dBi) because of the secondary reflection after conforming to the cone. Moreover, the conformal beam is wider than the nonconformal one in the azimuth plane.

Figure 10 shows the conformal beam scanned from  $80^\circ$  to  $97^\circ$  by varying frequency in the elevation plane. When the frequency is increased, the beam moves to a small theta angle. In the azimuth plane, the beam-width is mostly affected by the conformal geometry. As shown in Figure 11, by decreasing the curvature of conformal cone from  $13\text{ m}^{-1}$  to  $10.5\text{ m}^{-1}$ , the  $3$  dB beam-width is narrowed from  $34.6^\circ$  to  $31.3^\circ$ . Meanwhile, the gain increases by  $0.5$  dB.

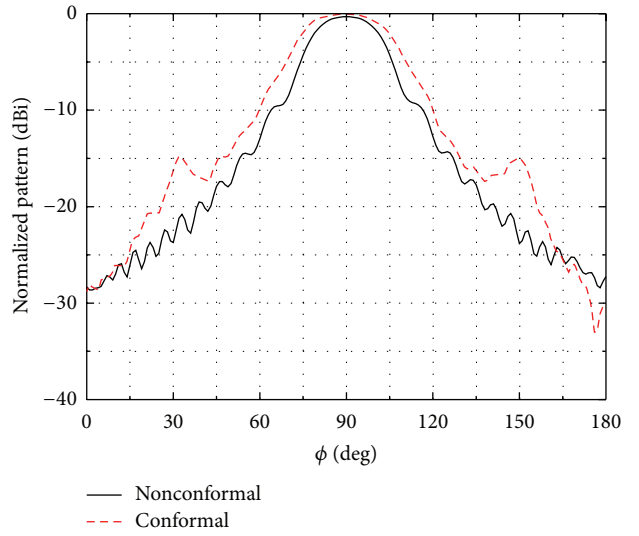


FIGURE 9: Simulated radiation pattern of the designed conformal and nonconformal antenna in the azimuth plane.

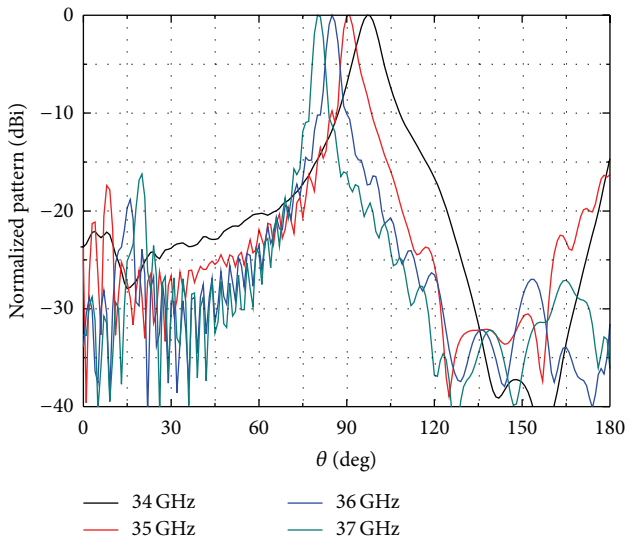


FIGURE 10: Scanned radiation patterns in the elevation plane.

### 3. Measurement Results

A prototype antenna is fabricated to validate our design as shown in Figure 12. The antenna is excited by the standard WR-28 waveguide; the transition between standard waveguide and SIW has the similar configuration as described in [19]. A coupled aperture is etched on the top conductor layer as shown in Figure 12(a). The purpose of the designed corner in Figure 12(a) is to make the excitation vertical to the horizontal plane. The reflection coefficients of the conformal and nonconformal antennas are measured by the network analyzer. As shown in Figure 13, the measured S-parameters are almost below  $-10$  dB within  $34\sim37$  GHz.

The radiation patterns of conformal and nonconformal antennas are measured in a microwave anechoic chamber. As

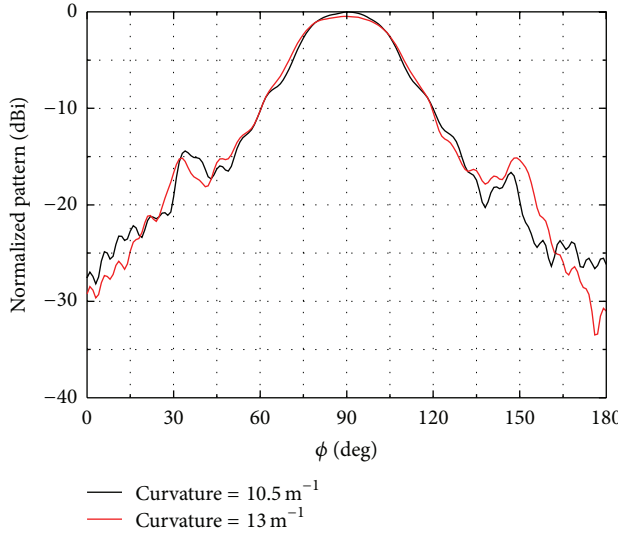


FIGURE 11: Radiation patterns in the azimuth plane by decreasing the curvature.

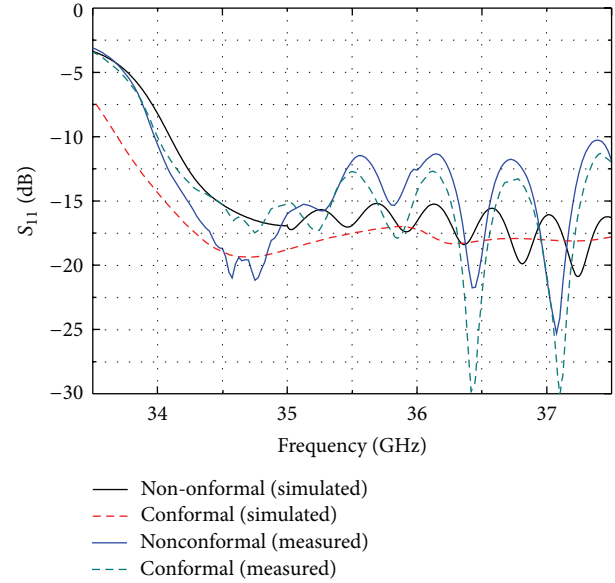


FIGURE 13: Measured S-parameters of the fabricated SIW leaky-wave antennas.

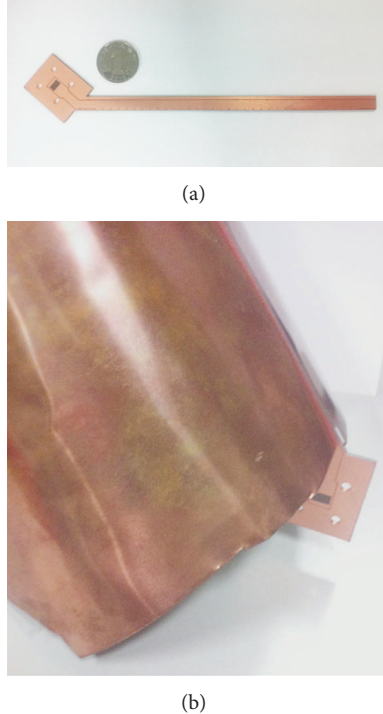


FIGURE 12: (a) Photograph of the fabricated leaky-wave antenna. (b) Photograph of the fabricated conformal leaky-wave antenna.

shown in Figures 14-15, the measured results have the same trend of the simulated ones.

Then, the radiation patterns of conformal antenna are measured at different frequencies from 34 GHz to 37 GHz as shown in Figure 16. Table 2 summarizes the measured data. In the azimuth plane, it can cover an angular region of  $40.9^\circ$ . The radiation patterns with different conformal curvatures are also measured as the simulation as shown in Figure 17. The 3 dB beam-width is narrowed with  $3.2^\circ$ .

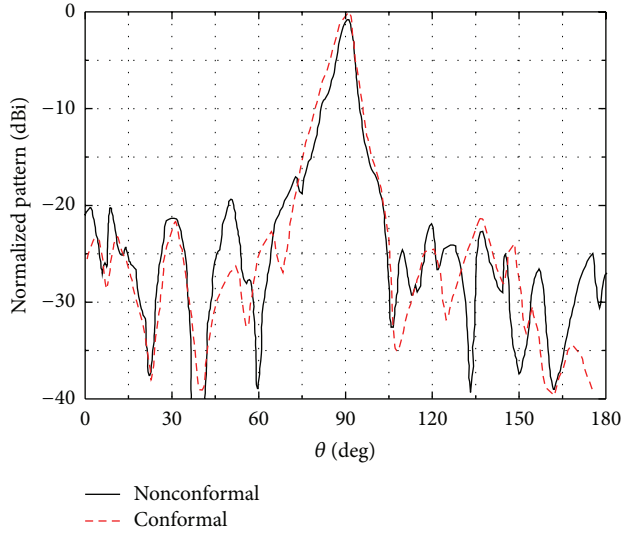


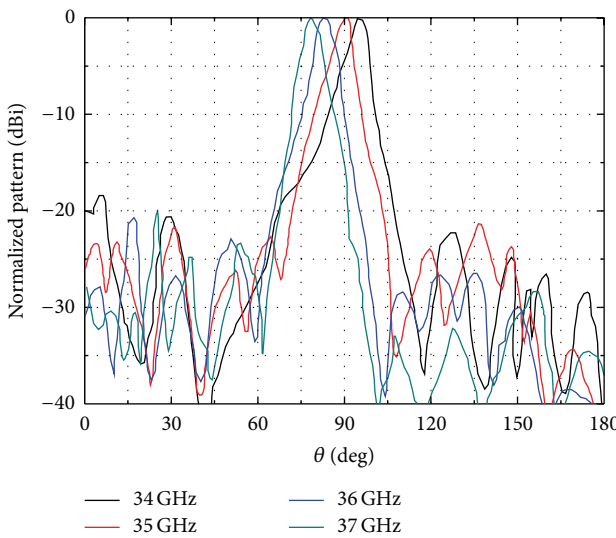
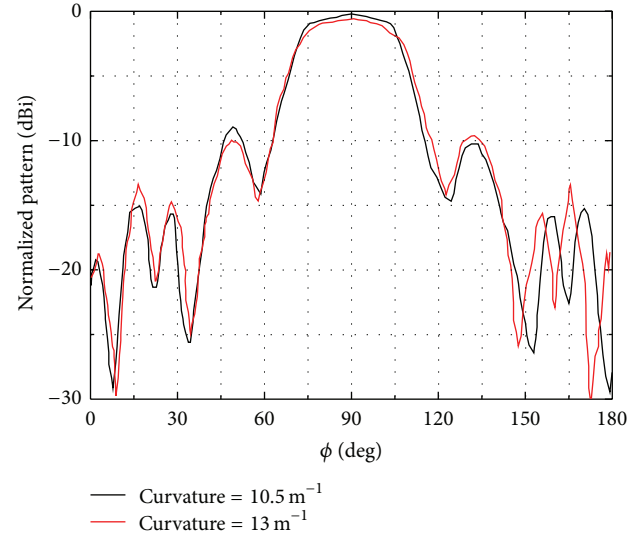
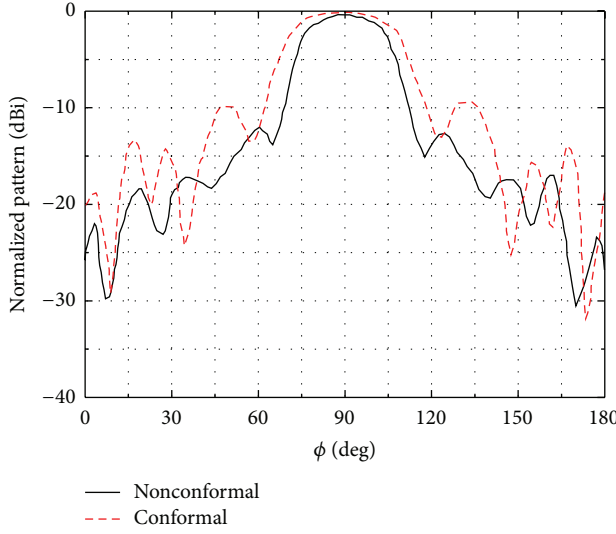
FIGURE 14: Measured radiation pattern in the elevation plane of the fabricated SIW leaky-wave antennas.

TABLE 2: Measurements of antenna at different frequency.

Frequency (GHz)	Simulated gain (dBi)	Measured gain (dBi)	Beam direction
34	14.95	14.38	$96.5^\circ$
35	15.5	15.55	$90.7^\circ$
36	16.35	16.13	$84.1^\circ$
37	17.36	17.07	$79.6^\circ$

#### 4. Conclusion

A conical conformal leaky-wave antenna based on the SIW technology is designed and experimented. It presents a wide



beam-width in the azimuth plane and a narrow beam-width in the elevation plane. This conformal antenna can scan from 80° to 97° with varying frequency (34 GHz~37 GHz). The measured antenna characteristics agree well with the simulations. Besides, the antenna has the advantages of low loss, high efficiency, and simple configuration.

## Conflict of Interests

The authors declare that there is no conflict of interests regarding the publication of this paper.

## Acknowledgments

This work is supported in part by Program for New Century Excellent Talents in University under Grant NCET-13-0089 and by the State Key Laboratory of Millimeter Waves under Grant K201315.

## References

- [1] L. Josefsson and P. Persson, *Conformal Array Antenna Theory and Design*, Wiley-Interscience, Hoboken, NJ, USA, 2006.
- [2] A. A. Oliner and D. R. Jackson, "Leaky-wave antennas," in *Antenna Engineering Handbook*, J. L. Volakis, Ed., chapter 11, McGraw Hill, New York, NY, USA, 4th edition, 2007.
- [3] D. Deslandes and K. Wu, "Substrate integrated waveguide leaky-wave antenna: concept and design considerations," in *Proceedings of the Asia-Pacific Microwave Conference (APMC '05)*, vol. 1, December 2005.
- [4] J. Xu, W. Hong, H. Tang, Z. Kuai, and K. Wu, "Half-mode substrate integrated waveguide (HMSIW) leaky-wave antenna for millimeter-wave applications," *IEEE Antennas and Wireless Propagation Letters*, vol. 7, pp. 85–88, 2008.
- [5] Y. J. Cheng, W. Hong, K. Wu, and Y. Fan, "Millimeter-wave substrate integrated waveguide long slot leaky-wave antennas and two-dimensional multibeam applications," *IEEE Transactions on Antennas and Propagation*, vol. 59, no. 1, pp. 40–47, 2011.
- [6] J. Radcliffe, G. Thiele, R. Penno, S. Schneider, and L. Kempel, "Microstrip leaky-wave antenna performance on a curved surface," in *Proceedings of the IEEE Antennas and Propagation Society International Symposium (APSURSI '06)*, pp. 4247–4250, July 2006.
- [7] Y. Li, Q. Xue, E. K.-N. Yung, and Y. Long, "A fixed-frequency beam-scanning microstrip leaky wave antenna array," *IEEE Antennas and Wireless Propagation Letters*, vol. 6, pp. 616–618, 2007.
- [8] Y. J. Cheng, W. Hong, and K. Wu, "Millimeter-wave half mode substrate integrated waveguide frequency scanning antenna

- with quadri-polarization,” *IEEE Transactions on Antennas and Propagation*, vol. 58, no. 6, pp. 1848–1855, 2010.
- [9] J. Liu, D. R. Jackson, and Y. Long, “Substrate integrated waveguide( SIW) leaky-wave antenna with transverse slots,” *IEEE Transactions on Antennas and Propagation*, vol. 60, no. 1, pp. 20–29, 2012.
  - [10] J. Machac, M. Polivka, and K. Zemlyakov, “A dual band leaky wave antenna on a CRLH substrate integrated waveguide,” *IEEE Transactions on Antennas and Propagation*, vol. 61, no. 7, pp. 3876–3879, 2013.
  - [11] Y. J. Cheng, Y. X. Guo, X. Y. Bao, and K. B. Ng, “Millimeter-wave low temperature co-fired ceramic leaky-wave antenna and array based on the substrate integrated image guide technology,” *IEEE Transactions on Antennas and Propagation*, vol. 62, no. 2, pp. 669–676, 2014.
  - [12] L.-C. Lin, H. Miyagawa, T. Kitazawa, R. B. Hwang, and Y.-D. Lin, “Characterization and design of cylindrical microstrip leaky-wave antennas,” *IEEE Transactions on Antennas and Propagation*, vol. 56, no. 7, pp. 1853–1859, 2008.
  - [13] J. L. Gómez-Tornero, “Analysis and design of conformal tapered leaky-wave antennas,” *IEEE Antennas and Wireless Propagation Letters*, vol. 10, pp. 1068–1071, 2011.
  - [14] A. J. Martínez-Ros, J. L. Gómez-Tornero, and G. Goussetis, “Conformal tapered microstrip leaky-wave antennas,” in *Proceedings of the 6th European Conference on Antennas and Propagation (EuCAP '12)*, pp. 154–158, March 2012.
  - [15] Y. J. Cheng, P. Chen, W. Hong, T. Djerafi, and K. Wu, “Substrate-integrated-waveguide beamforming networks and multibeam antenna arrays for low-cost satellite and mobile systems,” *IEEE Antennas and Propagation Magazine*, vol. 53, no. 6, pp. 18–30, 2011.
  - [16] G. Q. Luo, X. H. Zhang, L. X. Dong, W. J. Li, and L. L. Sun, “A gain enhanced cavity backed slot antenna using high order cavity resonance,” *Journal of Electromagnetic Waves and Applications*, vol. 25, no. 8-9, pp. 1273–1279, 2011.
  - [17] G. Q. Luo, Z. F. Hu, L. X. Dong, and L. L. Sun, “Planar slot antenna backed by substrate integrated waveguide cavity,” *IEEE Antennas and Wireless Propagation Letters*, vol. 7, pp. 236–239, 2008.
  - [18] Y. J. Cheng, H. Xu, D. Ma, J. Wu, L. Wang, and Y. Fan, “Millimeter-wave shaped-beam substrate integrated conformal array antenna,” *IEEE Transactions on Antennas and Propagation*, vol. 61, no. 9, pp. 4558–4566, 2013.
  - [19] Y. J. Cheng, W. Hong, and K. Wu, “94 GHz substrate integrated monopulse antenna array,” *IEEE Transactions on Antennas and Propagation*, vol. 60, no. 1, pp. 121–129, 2012.

## Research Article

# Gain Enhancement of a Microstrip Patch Antenna Using a Reflecting Layer

Anwer Sabah Mekki,<sup>1</sup> Mohd Nizar Hamidon,<sup>1,2</sup> Alyani Ismail,<sup>3</sup> and Adam R. H. Alhawari<sup>3</sup>

<sup>1</sup>Functional Devices Laboratory, Institute of Advanced Technology, Universiti Putra Malaysia (UPM), 43400 Serdang, Selangor, Malaysia

<sup>2</sup>Department of Electrical and Electronic Engineering, Universiti Putra Malaysia (UPM), 43400 Serdang, Selangor, Malaysia

<sup>3</sup>Wireless and Photonic Network Research Center, Department of Computer and Communication Systems Engineering, Universiti Putra Malaysia (UPM), 43400 Serdang, Selangor, Malaysia

Correspondence should be addressed to Anwer Sabah Mekki; [asmekki68@gmail.com](mailto:asmekki68@gmail.com)

Received 20 December 2014; Revised 5 March 2015; Accepted 5 March 2015

Academic Editor: Giampiero Lovat

Copyright © 2015 Anwer Sabah Mekki et al. This is an open access article distributed under the Creative Commons Attribution License, which permits unrestricted use, distribution, and reproduction in any medium, provided the original work is properly cited.

A low profile, unidirectional, dual layer, and narrow bandwidth microstrip patch antenna is designed to resonate at 2.45 GHz. The proposed antenna is suitable for specific applications, such as security and military systems, which require a narrow bandwidth and a small antenna size. This work is mainly focused on increasing the gain as well as reducing the size of the unidirectional patch antenna. The proposed antenna is simulated and measured. According to the simulated and measured results, it is shown that the unidirectional antenna has a higher gain and a higher front to back ratio (F/B) than the bidirectional one. This is achieved by using a second flame retardant layer (FR-4), coated with an annealed copper of 0.035 mm at both sides, with an air gap of  $0.04\lambda_0$  as a reflector. A gain of 5.2 dB with directivity of 7.6 dBi, F/B of 9.5 dB, and -18 dB return losses ( $S_{11}$ ) are achieved through the use of a dual substrate layer of FR-4 with a relative permittivity of 4.3 and a thickness of 1.6 mm. The proposed dual layer microstrip patch antenna has an impedance bandwidth of 2% and the designed antenna shows very low complexity during fabrication.

## 1. Introduction

Microstrip patch antennas have been of interest for a long time due to their low profile, low cost, easy printability, and fabrication, as well as the capability of being embedded within other devices. However, there are many disadvantages, such as low gain and narrow bandwidth [1, 2]. The gain of an antenna refers to the ratio of its radiation power in a specific direction to its power in the isotropic direction [3]. Many researchers are working to enhance the gain of the patch antennas using different designs, ideas, and materials [4–11]. On the other hand, narrow bandwidth system implementation improves system selectivity in a number of applications, including military, security, digital enhanced cordless telecommunications, and low power systems [12]. At the same time, due to the new technologies, most designers tend to reduce the size and increase the efficiency of the devices.

One of the common methods to enhance the gain and directivity is the use of reflector planes. In [13], using the concept of complementary antennas, a planer antenna is presented with a U-shaped metal reflector to achieve a unidirectional propagation; the resultant antenna has a low profile, high F/B, and high gain along the operating frequency range. Moreover, in [14], a multiple metal back reflector is proposed for a wideband slot antenna. In [15], using a metallic cavity shaped as a reflector with a magnetoelectric dipole antenna, the proposed antenna exhibits a high gain with high F/B in the operating frequency range with relatively large dimensions.

But in [16], using a substrate rather than metal as a reflector is introduced to enhance the F/B radiation with aperture coupled antennas. In [17], a high impedance surface (HIS), in the shape of arrays of square cells, is used to reduce the back lobe propagation. The design shows an enhancement in the gain along the frequency range and high F/B. In [18],

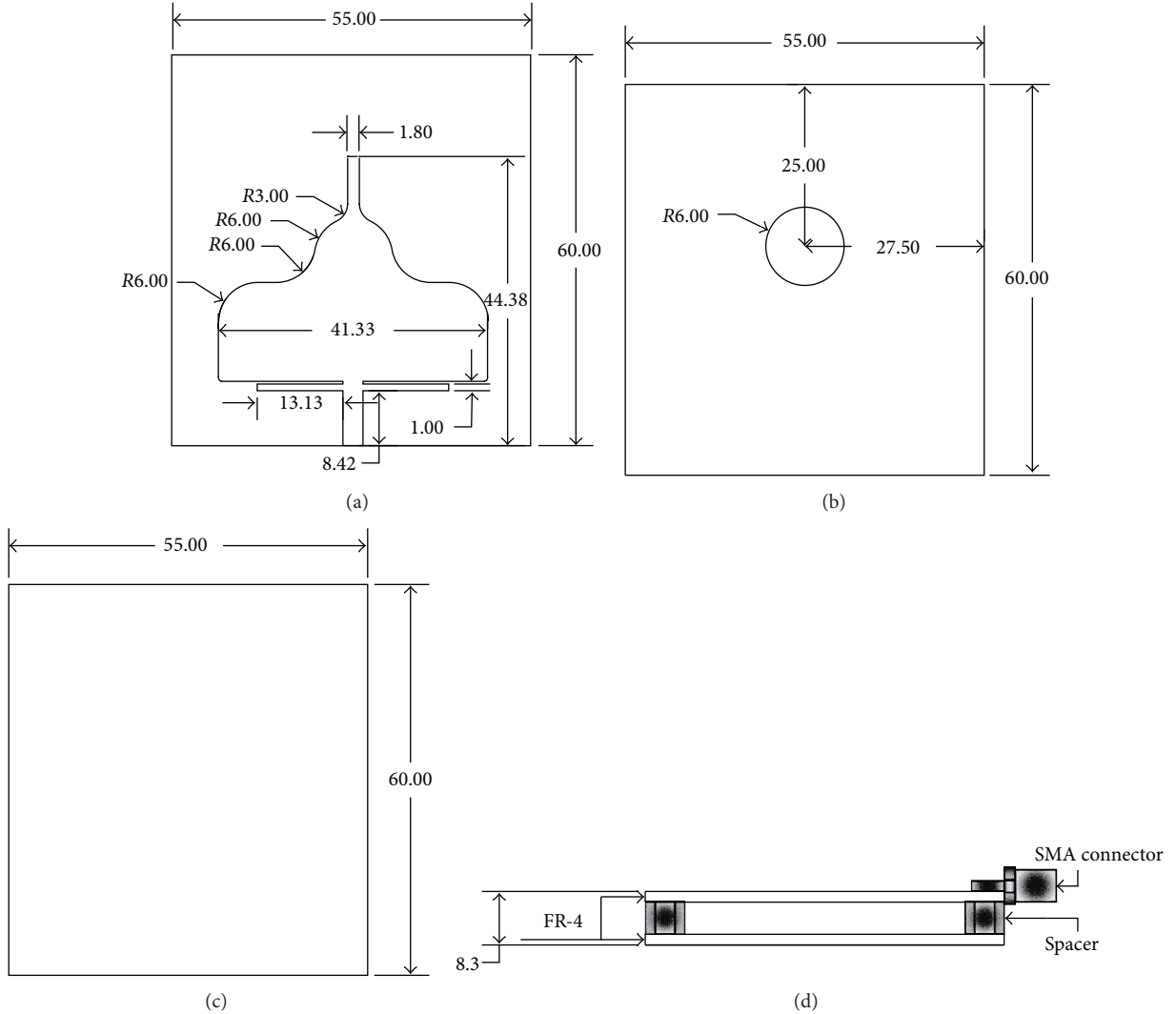


FIGURE 1: Proposed antenna design. (a) Patch antenna geometry, (b) ground side with circular slot, (c) second FR-4 layer (both sides), and (d) side view of the proposed antenna.

a dual band, unidirectional coplanar waveguide fed antenna (DB-CPWFA) is proposed. The reflector contains the ground plane, dielectric material, and artificial magnetic conductor. However, the dimensions of the antennas in the previous works are considered relatively large [13–18]. Therefore, achieving high gain while minimizing the size of the antenna is crucial.

In this paper, a new microstrip patch antenna is designed, simulated, and fabricated. The effect of the reflector layer on the gain and directivity is studied and evaluated. Furthermore, the air gap thickness between the two layers of the substrates is investigated. By tuning and optimization, the desired characteristics are achieved and the effect of the multigeometrical shapes is shown. The simulation results are compared to the DB-CPWFA [18] and the conventional microstrip patch antenna [19]. The simulated results are validated by the measurements and the effect of the reflector layer is verified. The measurement results demonstrate that the gain, directivity, and F/B ratio of the antenna have been significantly improved.

## 2. Proposed Antenna

The proposed dual-layer microstrip patch antenna design was developed by taking the design of the conventional square patch antenna, then changing it by removing symmetrical parts from the left and right sides, changing the right angles to curves, and finally introducing a circular slot in the ground plane. Finally, the proposed design is accomplished using a second layer of FR-4, which is coated with a copper film at both sides, spaced  $0.04\lambda_0$  from the ground layer.

In order to make the patch antenna operate at the desired characteristics, a tuning and optimization technique is introduced. Therefore, in order to make the design more flexible and workable during this procedure the proposed antenna contains multigeometrical details. In antenna designs, sacrificing some parameters is compulsory in order to enhance others [20].

Figure 1 illustrates the dimensions of the proposed antenna. The overall dimensions are  $60 \text{ mm} \times 55 \text{ mm} \times 8.3 \text{ mm}$ . The substrate is FR-4, with a permittivity of 4.3 and loss

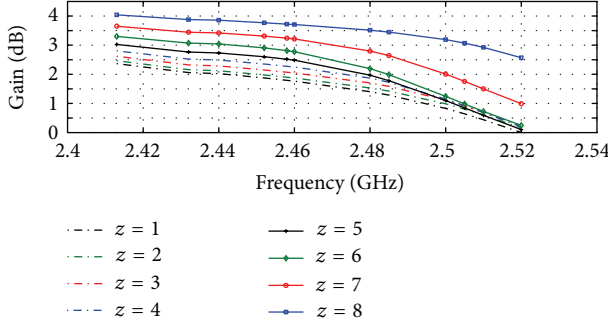


FIGURE 2: Effect of ground circular slot on the gain.

tangent of 0.025, coated with annealed copper of 0.035 mm thickness at both sides. Four spacers are used, which are made of Teflon PTFE (polytetrafluoroethylene), which is a lossy material, with 2.1 relative permittivity. A second FR-4 layer, which is coated with annealed copper of 0.035 mm thickness at both sides, is placed at a distance of  $0.04\lambda_0$  from the first FR-4 layer. The second FR-4 layer acts as a reflector to redirect the propagation density from the back lobe to the main lobe. Hence, for the same radiation efficiency, increasing the directivity,  $D$ , means increasing the gain,  $G$ , as follows [3]:

$$G = \eta D, \quad (1)$$

where  $\eta$  is the radiation efficiency.

The patch antenna is fed using a microstrip feed transmission line with  $50\Omega$  characteristic impedance, 8.2 mm length, and 3 mm width. The inset feed transmission line is connected to the port using a subminiature version A (SMA) connector.

### 3. Simulation Results

The proposed design was simulated using CST-MW studio; the design was done through three main stages. The first stage consisted of a primary design, which contained a single layer antenna with a full ground plane. The characteristics of the first stage antenna were enhanced in the second stage by introducing a circular slot of 6 mm radius in the ground layer. The slot radius was chosen through sweeping the radius in the simulation from zero to 8 mm. Figure 2 shows the effect of the radius ( $z$ ) in mm of the circular slot on the gain of the second stage. From Figure 2, it can be shown that the gain can be increased by increasing the radius of the slot. However, this will increase the return losses; therefore, it is a matter of trade-off between the gain and return losses. At the last stage, a second substrate layer, which is coated with 0.035 mm copper films at both sides, is added at a distance of  $0.04\lambda_0$  from the ground layer and fixed using four cylindrical PTFE spacers with outer diameter of 6.5 mm and inner diameter of 3 mm as shown in Figure 3.

The characteristics of the three stages, the DB-CPWFA [18], and the conventional square patch antenna [19] are illustrated in Table 1. It can be observed that, from Table 1, the proposed antenna outperforms both the conventional

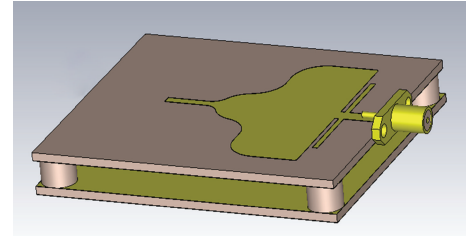


FIGURE 3: Perspective view of the proposed antenna.

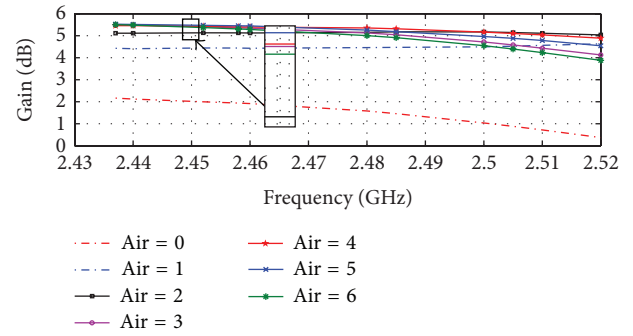


FIGURE 4: Effect of air gap thickness on the gain at desired frequency.

one in terms of matching impedance and gain and the DB-CPWFA in terms of matching impedance, complexity, and a significant size reduction of 67.4% with a comparable gain. Since the gain is directly proportional to the effective area of the antenna [3], the resultant simulated gain of the proposed antenna is considered comparable to that of the DB-CPWFA.

The effect of the air gap distance on the gain of the dual layer microstrip patch antenna at the desired frequency is shown in Figure 4. The values of air, in Figure 4, represent the distance in mm between the two-substrate layers. In comparison with the conventional microstrip patch antenna, it is clear that there is an increment in the gain along the distance range from air = 1 mm to air = 6 mm. The curve reaches the maximum value at the desired frequency with an air gap distance of 5 mm.

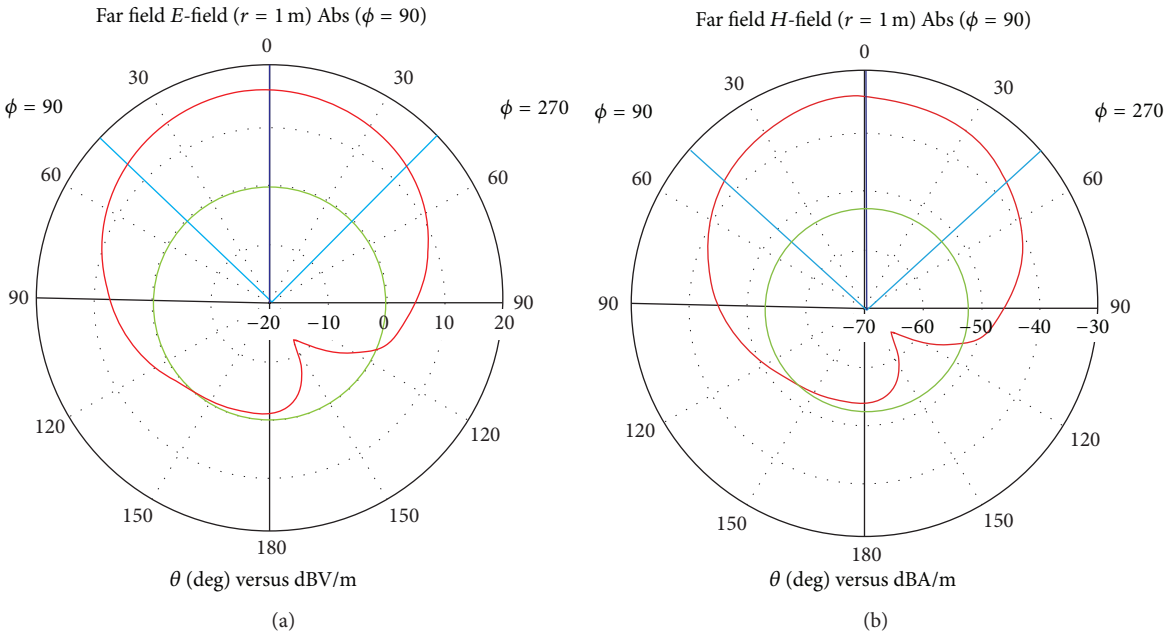
The directivity of the three stages and the conventional microstrip patch antenna are listed in Table 2.

Figures 5–8 show the far field directivity of the three stages and the conventional square patch antenna. The red color indicates the far field region, the angle of the main lobe direction is colored with blue, and the green color indicates the maximum value of the back lobe direction. With the spacing value chosen of  $0.04\lambda_0$ , the reflected radiation from the second layer reinforces the main lobe radiation. As a result, the main lobe is increased. Accordingly, the gain is increased by 2.16 dB as compared to the conventional microstrip patch antenna. Moreover, an approximately perfect matching is achieved; the impedance of the proposed antenna is  $(49.3 + j3.88)\Omega$  with a quality factor of 16.8 and F/B ratio of 9.5 dB.

TABLE 1: Comparison of the antennas' parameters.

Design	$f_r$ (GHz)	$S_{11}$ (dB)	G (dB)		$D$ (dBi)	$\eta$	VSWR	Impedance BW (MHz)	Size ( $L_s \times W_s \times H$ ) mm <sup>3</sup>
			Sim.	Mrd.					
First stage	2.423	-7.85	2.22		6.340	0.386	2.326	—	55 × 60 × 1.6
Second stage	2.411	-25.028	3.30		5.938	0.544	1.118	42.8	55 × 60 × 1.6
Third stage (proposed design)	2.45	-28.028	5.4	5.2	7.747	0.582	1.082	44.7	55 × 60 × 8.37
DB-CPWFA [18]	2.45 & 5.8	-15 & -37	7 & 6.8	6 & 8.5	—	—	—	245 & 745	100 × 120 × 7
Conventional [19]	2.344	-12.617	3.11		5.02	0.64	1.61	64.8	40 × 40 × 1.6

$f_r$  is the resonance frequency, Sim. is the simulated gain, Mrd. is the measured gain, VSWR is the voltage standing wave ratio,  $W_s$  is the width of the substrate,  $L_s$  is the length of the substrate, and  $H$  is the height of the antenna.

FIGURE 5: First stage of proposed antenna. (a)  $E$ -field and (b)  $H$ -field.

#### 4. Fabrication and Measurements

Using FR-4 substrates with  $\epsilon_r$  of 4.3, the proposed antenna has been fabricated. The second layer is fixed at 5 mm using four Teflon spacers and thin films of solvent adhesive with  $\epsilon_r$  of 2. The dual layer microstrip patch antenna is connected to  $50\Omega$  SMA connector. The overall dimensions are 60 mm × 55 mm × 8.3 mm; the 8.3 mm equals  $0.069\lambda_0$ . The  $S_{11}$  parameter of the fabricated antenna is measured using a vector network analyzer (Anritsu 37347D). The gain of the fabricated antenna is measured using a vector signal generator (Anritsu MG3700A), a spectrum analyser (Advantest R3267), and a two-horn antenna with dual polarization (A-INFOMW). Figure 9 shows the fabricated dual layer of the proposed microstrip patch antenna.

The differences in values between the simulation and measurement results are due to the effect of analogue losses and deficiencies. These factors cannot be taken into account using the currently available simulation software.

In Figure 10, a comparison of  $S_{11}$  parameter between simulated and measured results is shown. The measured value of  $S_{11}$  is -18 dB while the simulated value is -28 dB. The measured gain of the proposed antenna is 5.2 dB and it is comparable with the simulated gain, which is 5.4 dB. In comparison with the DB-CPWFA, the measured gain of the proposed antenna is close to the measured gain of the DB-CPWFA, which is 6 dB, as shown in Table 1.

#### 5. Conclusion

A unidirectional and low profile microstrip patch antenna of  $0.069\lambda_0$  has been introduced. Using a second layer of FR-4, which is coated with copper, reduced the back lobe and enhanced the gain up to 5.4 dB as well as increased the directivity up to 7.74 dBi with F/B ratio of 9.5 dB. Moreover, the proposed antenna shows flexibility during the optimization technique and the simulation results are evaluated by measurements.

TABLE 2: Comparison of the directivity of the proposed antenna (three stages) and the conventional microstrip patch antenna [19].

Design	$f_r$ (GHz)	Main lobe magnitude (E-field) dBV/m	Main lobe magnitude (H-field) dBA/m	Main lobe direction (degree)	Angular width at 3 dB (degree)	F/B (dB)
First stage	2.365	-35.3	16.2	0.0	92.2	16.7
Second stage	2.353	-33.5	18.1	6	84.4	7.6
Third stage (proposed antenna)	2.392	-31.4	20.2	6	71.6	9.5
Conventional [19]	2.344	-34.2	17.4	8	100.1	7.6

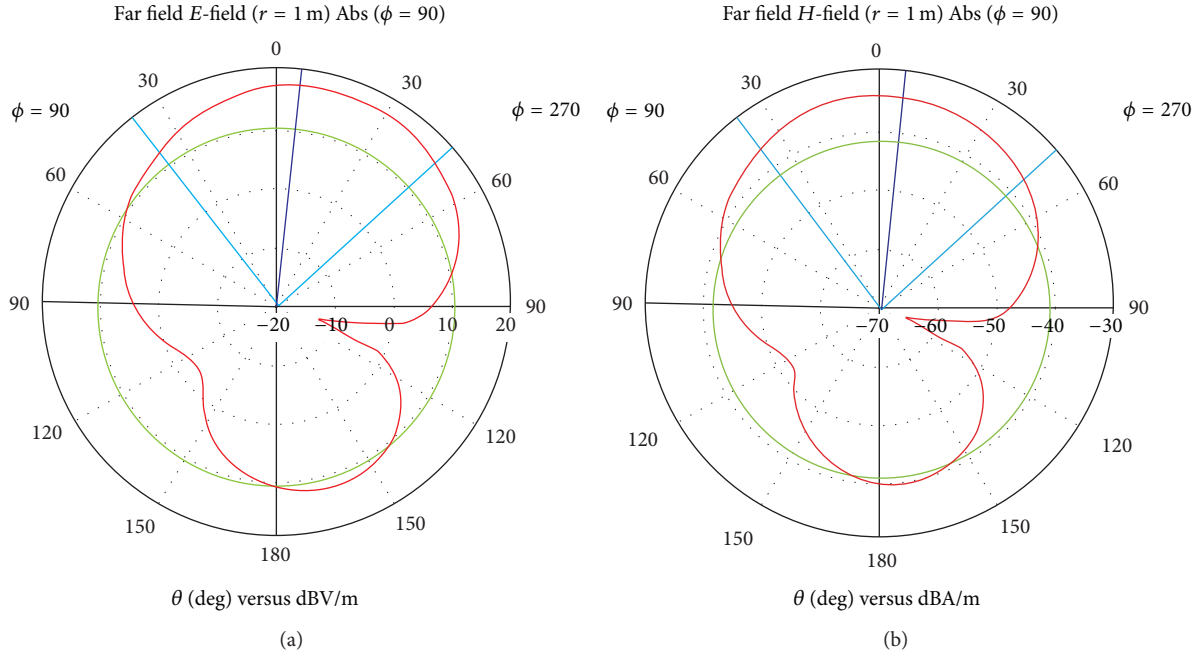


FIGURE 6: Second stage of proposed antenna. (a) E-field and (b) H-field.

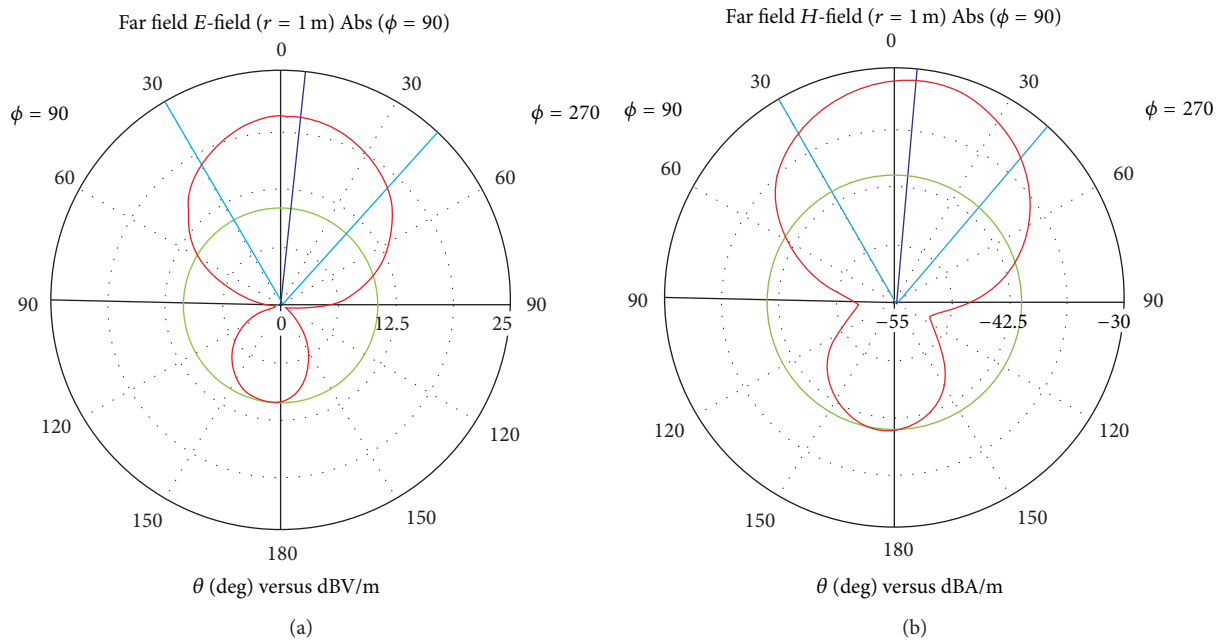


FIGURE 7: Third stage (final) of proposed antenna. (a) E-field and (b) H-field.

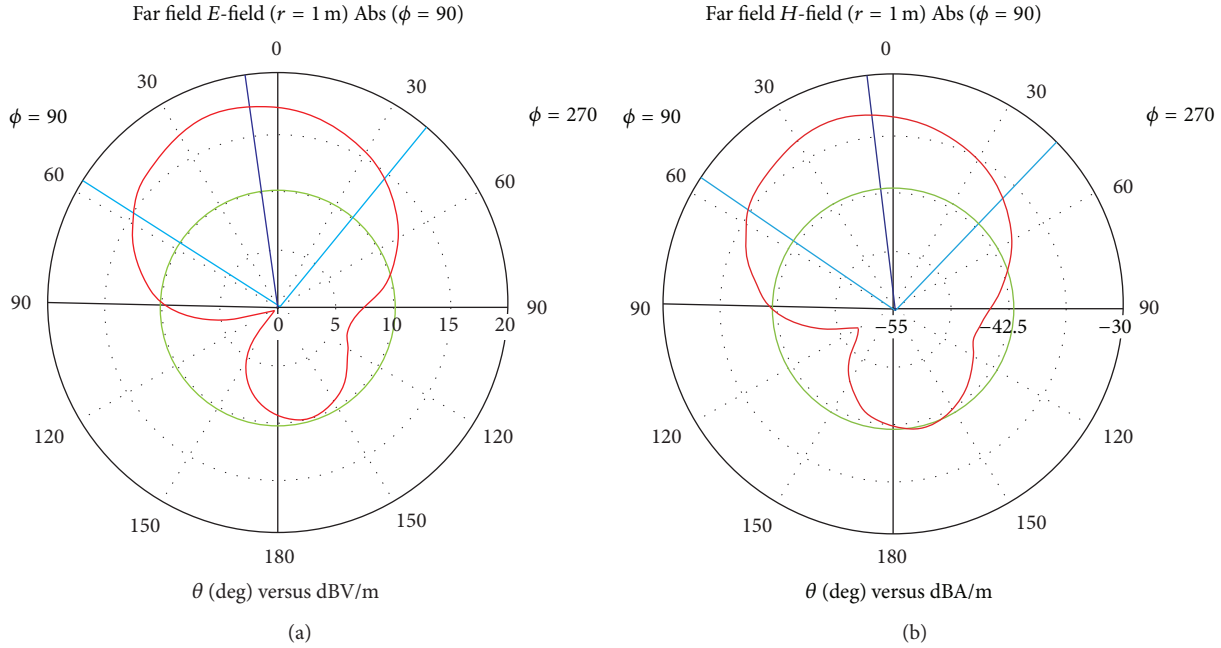


FIGURE 8: Conventional microstrip patch antenna. (a)  $E$ -field and (b)  $H$ -field.

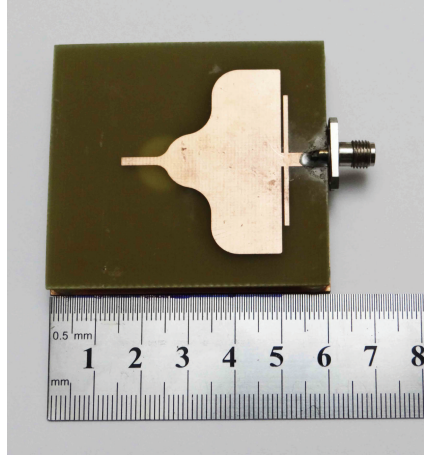


FIGURE 9: Fabricated antenna.

The proposed antenna is compatible for specific applications, such as security and military systems, due to considerable gain, small size, low profile, and unidirectional propagation. Furthermore, it is easily fabricated at low cost and low complexity.

The proposed antenna outperforms both the conventional one in terms of the matching impedance and gain and the DB-CPWFA in terms of matching impedance and a significant size reduction of 67.4% with a comparable gain.

## Conflict of Interests

The authors declare that there is no conflict of interests regarding the publication of this paper.

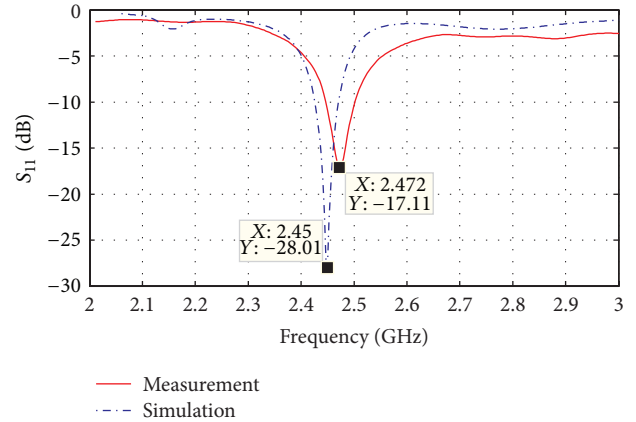


FIGURE 10: Simulated and measured return losses.

## References

- [1] C.-L. Mak, H. Wong, and K.-M. Luk, "High-gain and wide-band single-layer patch antenna for wireless communications," *IEEE Transactions on Vehicular Technology*, vol. 54, no. 1, pp. 33–40, 2005.
- [2] J.-W. Kim, T.-H. Jung, H.-K. Ryu, J.-M. Woo, C.-S. Eun, and D.-K. Lee, "Compact multiband microstrip antenna using inverted-L- and T-shaped parasitic elements," *IEEE Antennas and Wireless Propagation Letters*, vol. 12, pp. 1299–1302, 2013.
- [3] D. M. Pozar, *Microwave Engineering*, John Wiley & Sons, New York, NY, USA, 4th edition, 2012.
- [4] I. Zivkovic and K. Scheffler, "A new innovative antenna concept for both narrow band and UWB applications," *Progress in Electromagnetics Research*, vol. 139, pp. 121–131, 2013.

- [5] H. A. Majid, M. K. A. Rahim, and T. Masri, "Microstrip antenna's gain enhancement using left-handed metamaterial structure," *Progress In Electromagnetics Research M*, vol. 8, pp. 235–247, 2009.
- [6] B. Yildirim and B. A. Cetiner, "Enhanced gain patch antenna with a rectangular loop shaped parasitic radiator," *IEEE Antennas and Wireless Propagation Letters*, vol. 7, pp. 229–232, 2008.
- [7] S. B. Yeap and Z. N. Chen, "Microstrip patch antennas with enhanced gain by partial substrate removal," *IEEE Transactions on Antennas and Propagation*, vol. 58, no. 9, pp. 2811–2816, 2010.
- [8] K. Mandal and P. P. Sarkar, "High gain wide-band U-shaped patch antennas with modified ground planes," *IEEE Transactions on Antennas and Propagation*, vol. 61, no. 4, pp. 2279–2282, 2013.
- [9] Z. Park, C. Li, and J. Lin, "A broadband microstrip antenna with improved gain for noncontact vital sign radar detection," *IEEE Antennas and Wireless Propagation Letters*, vol. 8, pp. 939–942, 2009.
- [10] Z. Liu, P. Wang, and Z. Zeng, "Enhancement of the gain for microstrip antennas using negative permeability metamaterial on low temperature co-fired ceramic (LTCC) substrate," *IEEE Antennas and Wireless Propagation Letters*, vol. 12, pp. 429–432, 2013.
- [11] A. Rivera-Albino and C. A. Balanis, "Gain enhancement in microstrip patch antennas using hybrid substrates," *IEEE Antennas and Wireless Propagation Letters*, vol. 12, pp. 476–479, 2013.
- [12] C. A. Balanis, *Antenna Theory Analysis and Design*, John Wiley & Sons, 3rd edition, 2005.
- [13] M. Li and K.-M. Luk, "A low-profile wideband planar antenna," *IEEE Transactions on Antennas and Propagation*, vol. 61, no. 9, pp. 4411–4418, 2013.
- [14] X. Gao, Y. Qi, and Y.-C. Jiao, "Design of multiplate back-reflector for a wideband slot antenna," *IEEE Antennas and Wireless Propagation Letters*, vol. 12, pp. 773–776, 2013.
- [15] L. Ge and K. M. Luk, "A low-profile magneto-electric dipole antenna," *IEEE Transactions on Antennas and Propagation*, vol. 60, no. 4, pp. 1684–1689, 2012.
- [16] Q. Rao, T. A. Denidni, and R. H. Johnston, "Dielectric reflector backed aperture-coupled antennas for reduced back radiation," *IEEE Transactions on Electromagnetic Compatibility*, vol. 48, no. 2, pp. 287–291, 2006.
- [17] X. Mu, W. Jiang, S.-X. Gong, and F.-W. Wang, "Dual-band low profile directional antenna with high impedance surface reflector," *Progress in Electromagnetics Research Letters*, vol. 25, pp. 67–75, 2011.
- [18] Q. Luo, H. Tian, Z. Huang, X. Wang, Z. Guo, and Y. Ji, "Unidirectional dual-band CPW-fed antenna loaded with an AMC reflector," *International Journal of Antennas and Propagation*, vol. 2013, Article ID 875281, 10 pages, 2013.
- [19] C. Kamtongdee and N. Wongkasem, "A novel design of compact 2.4 GHz microstrip antennas," in *Proceedings of the 6th International Conference on Electrical Engineering/Electronics, Computer, Telecommunications and Information Technology*, vol. 4, pp. 766–769, May 2009.
- [20] W. L. Stutzman and G. A. Thiele, *Antenna Theory and Design*, John Wiley & Sons, 3rd edition, 2013.

## Research Article

# Novel Miniaturized Octaband Antenna for LTE Smart Handset Applications

**Haixia Liu, Bo Lu, and Long Li**

*School of Electronic Engineering, Xidian University, Xi'an, Shaanxi 710071, China*

Correspondence should be addressed to Long Li; longliee@foxmail.com

Received 27 February 2015; Revised 30 April 2015; Accepted 5 May 2015

Academic Editor: Jaume Anguera

Copyright © 2015 Haixia Liu et al. This is an open access article distributed under the Creative Commons Attribution License, which permits unrestricted use, distribution, and reproduction in any medium, provided the original work is properly cited.

A novel octaband LTE mobile phone antenna is presented, which has a compact size with the overall dimension of 35 mm × 9 mm × 3 mm. The miniaturized octaband antenna is implemented by a simple prototype of three parts which include a folded monopole as feeding element, main radiator element, and parasitic radiator element. The main and parasitic radiator elements are excited by the folded monopole feeding element coupling and shorting to the handset ground plane. A wide bandwidth in low-frequency bands covering from 747 MHz to 960 MHz (LTE Band13/GSM850/GSM900) is contributed by both main and parasitic radiator elements. In addition, the folded monopole is designed to resonate at 2530 MHz, and the coupling between the feeding element and main radiator element is designed to resonate at 1840 MHz. Subsequently, the wide bandwidth in high-frequency bands covering from 1710 MHz to 2690 MHz (DCS1800/PCS1900/WCDMA2100/LTE2300/LTE2500) is contributed by both structures. The antenna has the total efficiency up to 30% in low bands and up to 75% in high bands, respectively. At the same time, the proposed miniaturized octaband LTE mobile phone antenna is fabricated and tested to verify the design.

## 1. Introduction

Nowadays, with the rapid development of wireless communication technology, there is a great demand for high-performance, multifunction, slight, and thin wireless terminal products. Therefore, it gives rise to a challenging demand for miniaturized, low-profile, broadband, high-efficiency, highly integrated, and low-cost antennas [1–6]. With the development and promotion of the LTE standards, the smart mobile phones will be popular and widely used, and the design of new LTE antenna has been becoming a research hotspot. It is worth noting that the LTE mobile antennas should have wideband characteristics covering the working frequency bands of 2G, 3G, and 4G, which further increase the difficulty of cell phone antenna design [4–7]. Some kinds of miniaturized LTE handset antennas are proposed in [8–14]. Simultaneously, some design methods of decreasing antenna dimension and improving antenna performance were adopted [9–16]. An electrically small, wideband, and 4G handset antenna printed on a ceramic material with a high relative permittivity of 6.45 is reported in [9], where

the dimension of the antenna is 35 mm × 11 mm × 5 mm. But the material with high relative permittivity may lead to some undesired loss and the increase of cost. It is demonstrated that meander-line is suitable for miniaturizing dimension of the LTE handset antenna [10–13]. A planar printed antenna with folded monopole and folded shorting strip to cover the frequency bands of 698–960 MHz and 1710–2690 MHz is reported in [10], and the whole dimension of the antenna is 64 mm × 15 mm. The antenna with dimension of 40 mm × 15 mm × 3 mm is presented in [11], which has three wide operating bands 698–960 MHz, 1710–2690 MHz, and 5150–5825 MHz. Integrating lumped components into the antenna is another way to achieve miniaturization [8, 12–15]. A series chip capacitor (C) of 1.2 pF and a series chip inductor of 5.6 nH were used as matching circuit in the front of the antenna in [12] and a wide frequency band from 704 to 960 MHz and 1710 to 2690 MHz can be obtained. The area of the antenna is 34.5 mm × 10 mm, but the antenna is mounted along an edge and at a corner of the device ground plane of size 150 × 200 mm<sup>2</sup>, which is a reasonable size for the tablet computer with a 10 in display panel. Table 1 gives

TABLE 1: Comparison of the dimension, working bandwidth, and radiation efficiency of the antennas reported in references.

References	Dimension of substrate (mm <sup>3</sup> )	Dimension of antenna (mm <sup>3</sup> )	Frequency (MHz)	Radiation efficiency
[3]	100 × 60 × 0.8	9.5 × 60 × 3	698–960, 1710–2690	52–75% (L) 53–78% (H)
[6]	122 × 46 × 1	11 × 46 × 7	698–960, 1710–2690	55.3–71.3% (L) 32.5–98.1% (H)
[7]	115 × 40 × 1	15 × 40 × 1	685–1345, 1685–2985	50–70% (L) 50–82% (H)
[8]	110 × 55 × 1	12 × 55 × 4	809–975, 1675–2703	24%–44% (L) 40%–78% (H)
[12]	150 × 200 × 0.8	10 × 34.5 × 0.8	704–960, 1710–2690	40%–62% (L) 64%–92% (H)

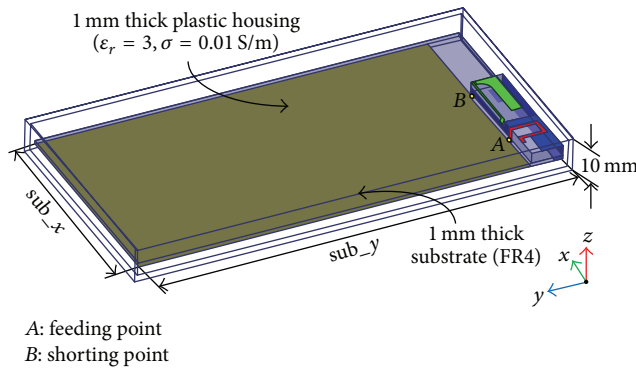


FIGURE 1: Overall structure of the proposed octaband LTE handset antenna.

the comparison of the dimension, working bandwidth, and radiation efficiency of the reported references.

Among these presented small-size LTE antennas, the methods of mender-line, lumped components, and high relative permittivity are applied to achieve the characteristics of miniature, low-profile, and high performance. In this paper, a new miniaturized octaband antenna for LTE smart mobile phone is introduced. The proposed antenna consists of three parts: the folded monopole feeding element, main radiator shorting element, and the parasitic radiator shorting element. It has a compact size with the overall dimension of 9 mm × 35 mm × 3 mm. Additionally, the parasitic radiator element is loaded with a lumped inductance of 4.7 nH, which can reduce the length of the antenna with good matching. Wide octaband operating bands covering the LTE Band13/GSM850/GSM900/DCS1800/PCS1900/WCDMA2100/LTE2300/LTE2500 (747–960 MHz, 1710–2690 MHz) can be obtained. The paper is arranged as follows. Section 2 will introduce the geometry and configuration of the proposed miniaturized LTE antenna. The operating mechanism of the proposed antenna is analyzed in Section 3. Moreover, the miniaturized LTE antenna is fabricated and measured. The measured and simulated results indicate the good performance of the proposed antenna. Finally, a conclusion is given in Section 4.

## 2. Antenna Design

The overall structure of the proposed new miniaturized octaband LTE handset is shown in Figure 1. The total dimension of the substrate is 60 mm × 120 mm, which is suitable for the actual smart handset platform. The 1 mm thick FR4 substrate with relative permittivity 4.4 and loss tangent 0.024 is used as the system circuit board. The proposed antenna is mounted on a 3 mm thick antenna holder that is also made of FR4 material. Note that a plastic casing made of a 1 mm thick plastic plate with relative permittivity 3.0 and loss tangent 0.02 encloses the system circuit board to simulate the practical mobile phone casing [7]. Figure 2 shows 3D view of the proposed octaband handset antenna and the detailed 2D topology. Note that the red dash-lines shown in Figure 2(b) represent the bending lines. The proposed antenna has a compact size with an overall volume of 35 mm × 9 mm × 3 mm, which is smaller than the proposed antennas in Table 1.

The proposed antenna has a simple structure. Table 2 shows the structural parameters in detail. It consists of a folded monopole feeding element, a main radiator element, and a parasitic radiator element. The folded monopole operates at upper band about 2530 MHz. The main and parasitic radiator elements are excited by the folded monopole feeding element coupling and shorting to the handset ground plane.

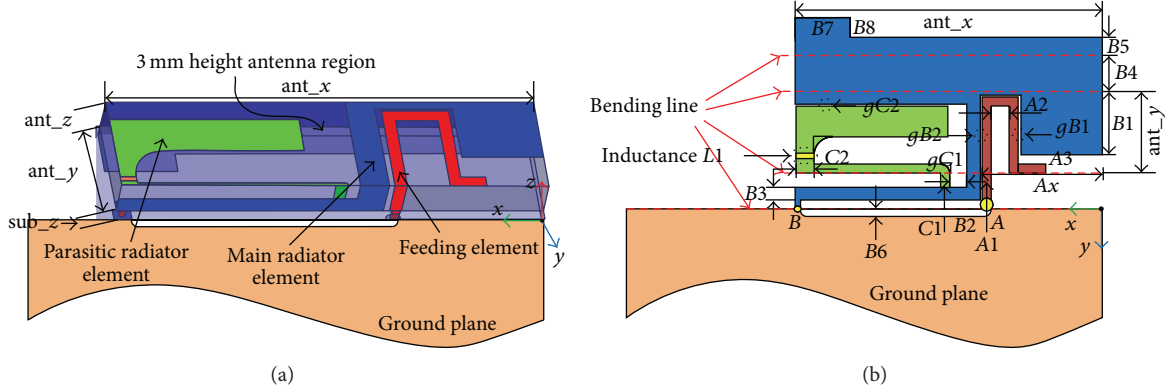


FIGURE 2: Configuration of the proposed octaband handset antenna, (a) 3-dimensional view and (b) 2-dimensional view (red dash-lines represent the bending lines).

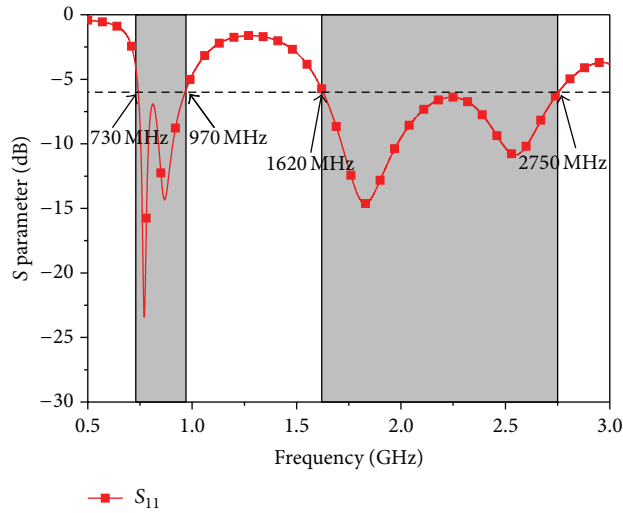


FIGURE 3: Simulated S parameter for proposed antenna.

TABLE 2: Detailed structural parameters of the proposed antenna (unit: mm).

ant_x	ant_y	ant_z	Ax	A1	A2	A3
35	9	3	12.6	1	3.5	2
$gB1$	$B1$	$gB2$	$B2$	$B3$	$B4$	$B5$
0.35	5.95	0.5	2.35	1.5	4	2
$B6$	$B7$	$B8$	$C1$	$gC1$	$C2$	$gC2$
0.7	6	2	1	1	1.35	0.6

The  $\text{sub}_z$  is referred to as the thickness of substrate, that is, 1 mm. The main radiator element can be excited by the capacitive coupling and generate a resonant mode at about 770 MHz, and the parasitic radiator element is also excited about 860 MHz. A lumped inductor (4.7 nH) is embedded in the parasitic radiator element to further reduce the size. A similar concept of using a short driven element coupled to a parasitic element was proposed for achieving operation at 2G and 3G bands in [17]. More importantly, the etched slit on the ground plane and the shorting strip with

the truncated corners are adopted to achieve a good impedance matching. And the etched ground plane can be regarded as a part of the antenna in order to realize the miniaturization. Therefore, a wide bandwidth covering lower frequency bands from 747 MHz to 960 MHz (LTE Band13/GSM850/GSM900) can be obtained. The strong capacitive coupling between the folded monopole and the main radiator element can generate a resonant mode at about 1840 MHz, which combines with the high resonant mode contributed by the folded monopole at 2530 MHz to produce wide high-frequency bands from 1710 to 2690 MHz (covering DCS1800/PCS1900/WCDMA2100/LTE2300/LTE2500). Therefore, the proposed antenna can cover the octaband operation in the 747–960 MHz and 1710–2690 MHz.

### 3. Results and Discussion

Figure 3 shows the simulated S parameter of the proposed antenna by using Ansys HFSS software based on finite-element full-wave analysis. It is clearly shown that a wide low-frequency band from 747 MHz to 960 MHz can be

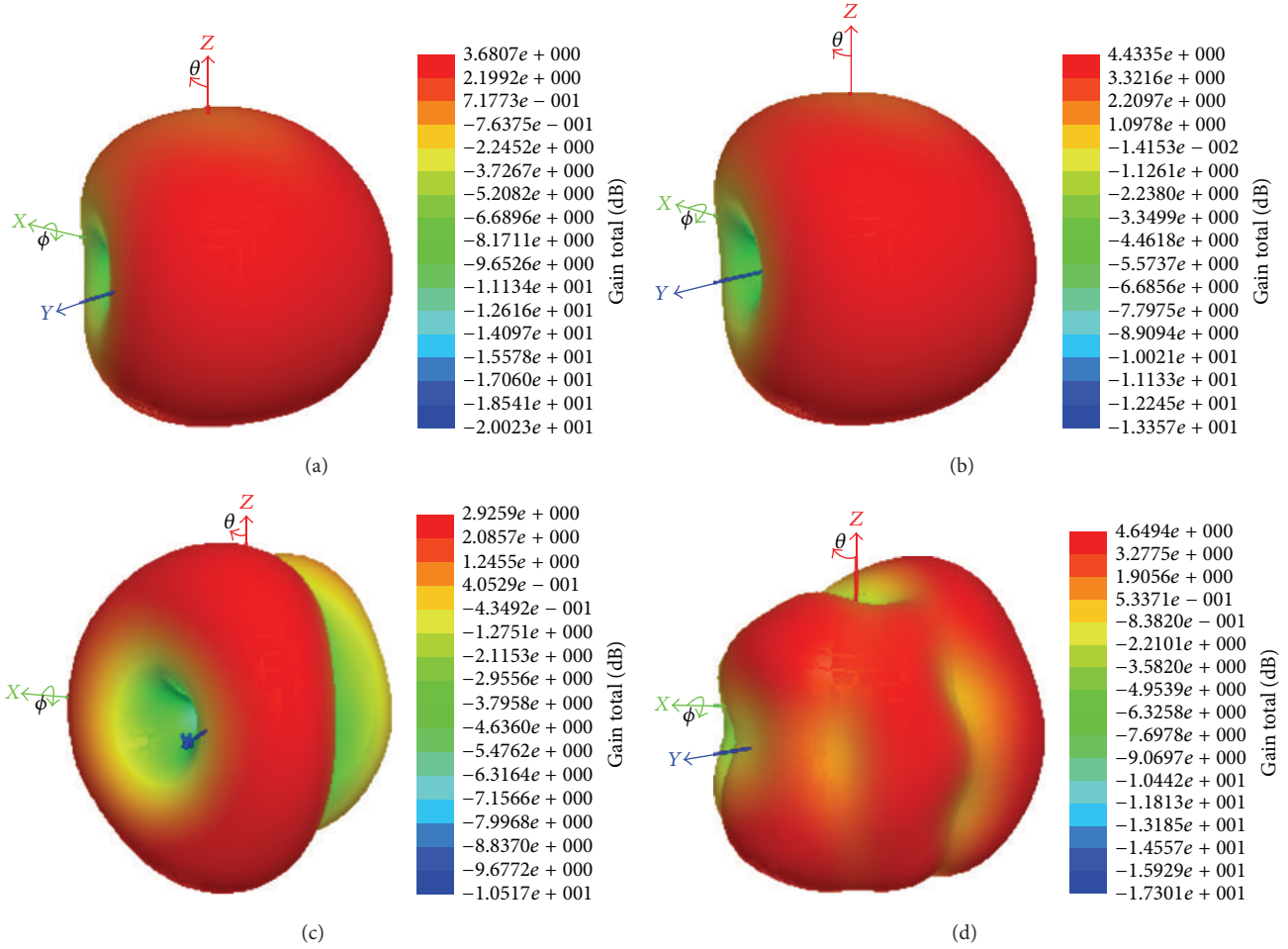


FIGURE 4: Simulated three-dimensional radiation patterns of proposed antenna, (a) 770 MHz, (b) 860 MHz, (c) 1840 MHz, and (d) 2530 MHz.

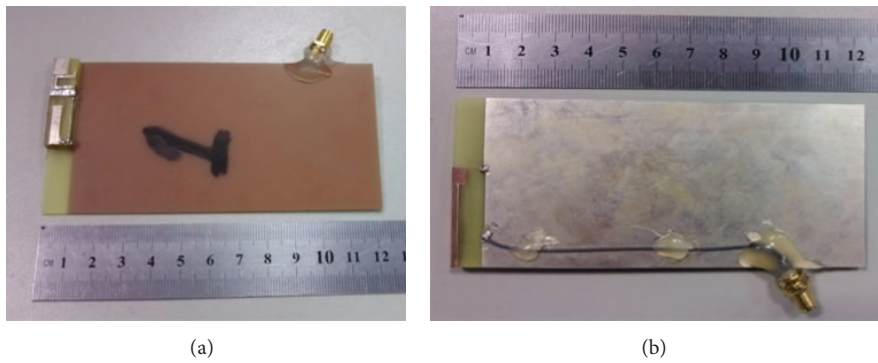


FIGURE 5: Prototype of the fabricated LTE handset antenna, (a) front view and (b) back view.

obtained based on the definition of  $-6 \text{ dB } S_{11}$  in the handset application. This allows the antenna to cover the LTE Band13/GSM850/GSM900 operation. Simultaneously, a wide high-frequency band from 1710 to 2690 MHz can be achieved. Therefore, the octaband operation of the LTE Band13/GSM850/GSM900/DCS1800/PCS1900/WCDMA2100/LTE 2300/LTE2500 can be obtained for the proposed antenna.

The simulated three-dimensional radiation patterns of the proposed antenna are shown in Figure 4 and the characteristics of omnidirectional radiation can be achieved.

The proposed octaband miniaturized LTE antenna prototype was fabricated and tested, as shown in Figure 5. The simulated results were obtained by the Ansys HFSS and the measured results were tested by an Agilent 8719ES



FIGURE 6: Test environment of LTE handset antenna in microwave anechoic chamber.

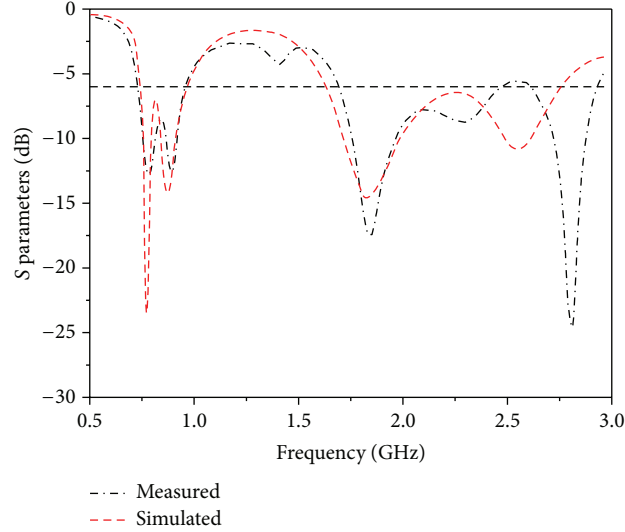
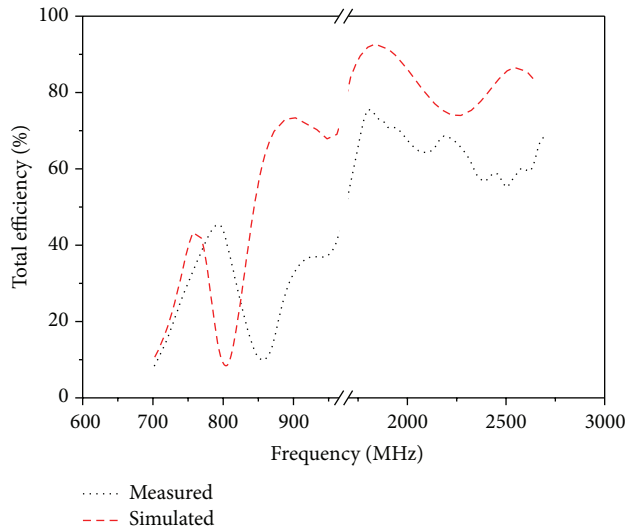
FIGURE 7: Comparison of simulated and measured  $S_{11}$ .

FIGURE 8: Comparison of simulated and measured total antenna efficiency.

vector network analyzer in a microwave anechoic chamber. Test environment of LTE handset antenna is shown in Figure 6. Figure 7 shows the comparison of the simulated and measured  $S_{11}$  of the antenna, and the good agreements are obtained between the measured and simulated results.

It is noteworthy that an additional resonance is produced at 2750 MHz, possibly because of the strong capacitive coupling of the radiation strips. The measured total antenna efficiency and three-dimensional radiation patterns of the proposed antenna are shown in Figures 8 and 9, respectively. It can

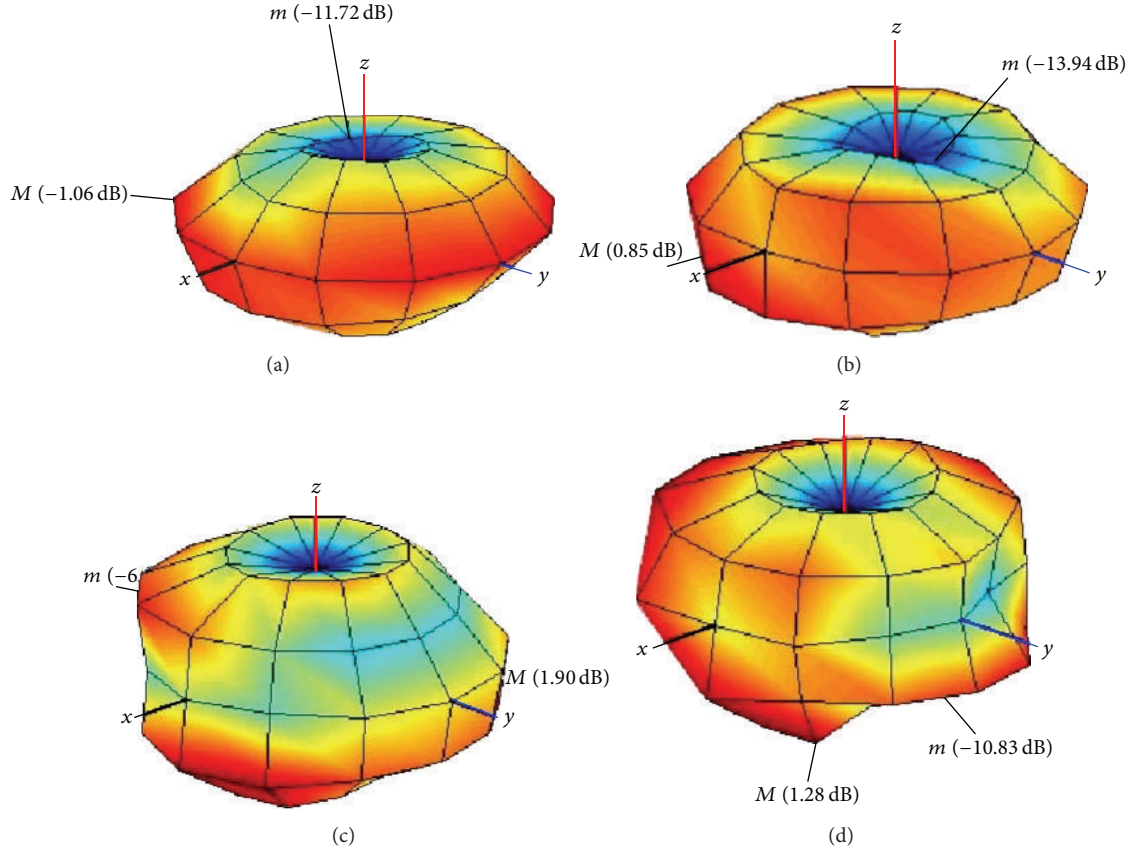


FIGURE 9: Measured three-dimensional radiation patterns of proposed antenna, (a) 767 MHz, (b) 885 MHz, (c) 1806 MHz, and (d) 2500 MHz.

be seen that the measured total efficiency of the antenna has some degradation and shift compared to the simulated results. The main reason is due to the material loss and fabrication errors. A surface-mount technology chip inductor of 4.7 nH (LQW15AN4N7B00D) was used, which is from Murata Manufacturing Co., Ltd. Because the inductor losses were not considered in the simulation, the measured results have some difference with the simulated results. Overall, the total efficiency of the proposed antenna is up to 75% in upper bands and up to 30% in lower bands. It can be seen from Figure 9 that the measured 3D radiation patterns of the antenna are close to omnidirectional radiation characteristics.

In order to analyze the characteristics of the proposed antenna in detail, the surface current distributions on the antenna and ground plane at the different operating frequencies are shown in Figure 10. It is clearly observed that the current is mainly distributed on the main radiator shorting element at 770 MHz, as shown in Figure 10(a), and on the parasitic radiator shorting element at 860 MHz, as shown in Figure 10(b). It can be seen that both main and parasitic radiator elements are excited to cover a broadband frequency range from 747 MHz to 960 MHz. The strong surface current on the folded monopole can be seen at 2530 MHz, as shown in Figure 10(d), which demonstrates that the mode is contributed by the folded monopole. Moreover,

the surface current between the folded monopole and the main radiator element is strengthened at 1840 MHz, as shown in Figure 10(c), which proves that the resonant mode is excited. Thus, a wide operating band from 1710 MHz to 2690 MHz can be obtained.

#### 4. Conclusions

In this paper, a new miniaturized LTE handset antenna is designed, fabricated, and measured, which exhibits an octaband operation in LTE Band13/GSM850/GSM900/DCS 1800/PCS1900/LTE2300/LTE2500 (747 MHz–960 MHz, 1710 MHz–2690 MHz) with high performance. It has a compact size with overall dimensions of 35 mm × 9 mm × 3 mm, which is smaller than the reported handset antenna. The antenna efficiency is generally larger than 30% in lower band and larger than 75% in upper band. It is worth pointing out that the proposed miniaturized octaband LTE antenna can be suitable for the application of next generation of wireless communications.

#### Conflict of Interests

The authors declare that there is no conflict of interests regarding the publication of this paper.

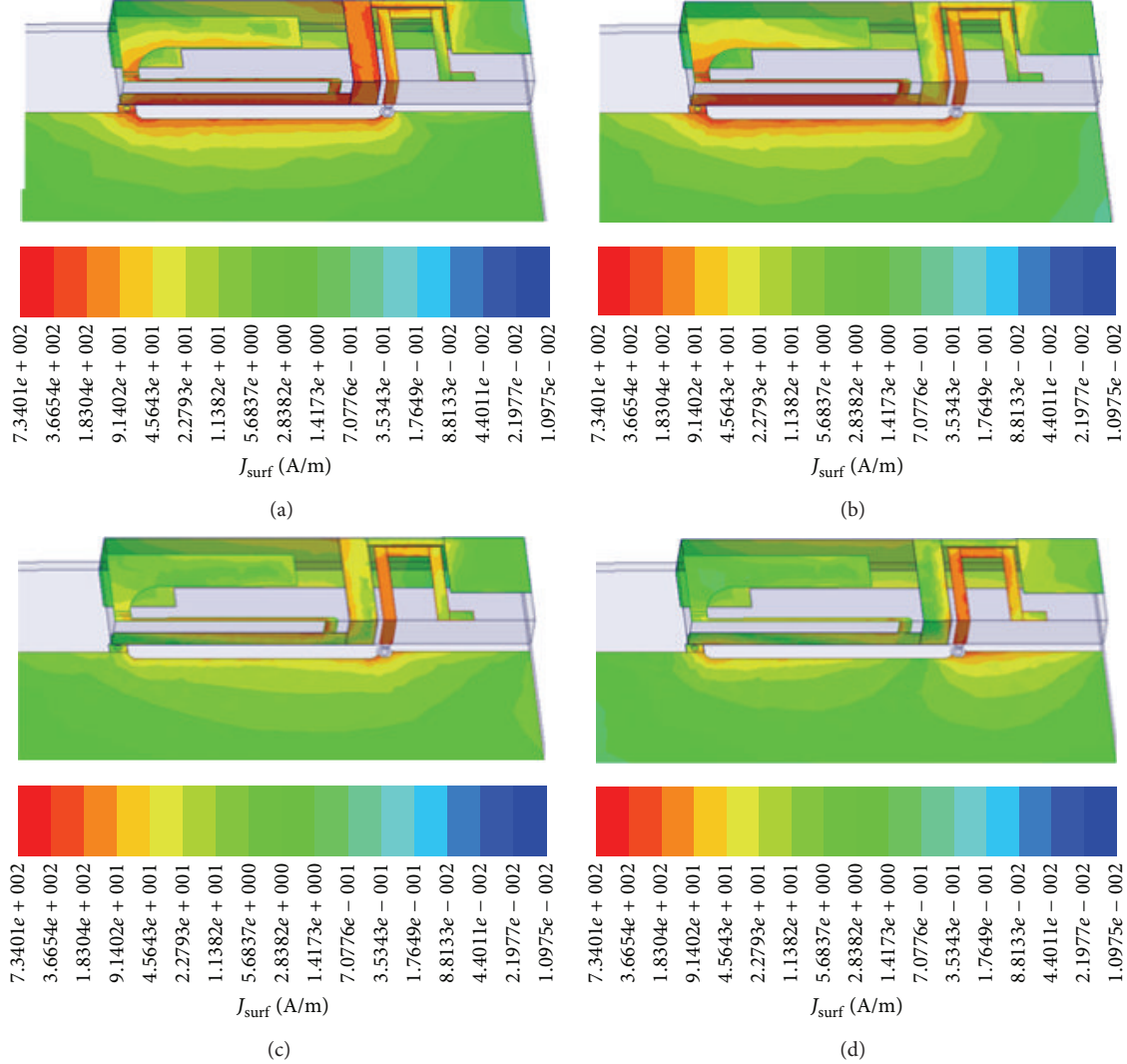


FIGURE 10: Characteristics of the current distribution on the antennas and ground plane, (a) 770 MHz, (b) 860 MHz, (c) 1840 MHz, and (d) 2530 MHz.

## Acknowledgments

This work is supported by National Natural Science Foundation of China under Contract no. 51477126 and supported partly by Natural Science Basic Research Plan in Shaanxi Province of China (no. 2013JZ019), Technology Innovation Research Project of the CETC, and Fundamental Research Funds for the Central Universities (K5051202051, K5051302025).

## References

- [1] M. Kim, W. Lee, W. Kim, and Y. J. Yoon, "A multi-band internal antenna for all commercial mobile communication bands and 802.11a/b/g/n WLAN," in *Proceedings of the Asia-Pacific Microwave Conference (APMC '11)*, pp. 171–174, Melbourne, Australia, December 2011.
- [2] J. Villanen, J. Ollikainen, O. Kivekäs, and P. Vainikainen, "Coupling element based mobile terminal antenna structures," *IEEE Transactions on Antennas and Propagation*, vol. 54, no. 7, pp. 2142–2153, 2006.
- [3] K.-L. Wong, W.-Y. Chen, C.-Y. Wu, and W.-Y. Li, "Small-size internal eight-band LTE/WWAN mobile phone antenna with internal distributed LC matching circuit," *Microwave and Optical Technology Letters*, vol. 52, no. 10, pp. 2244–2250, 2010.
- [4] J. Anguera, A. Andújar, M.-C. Huynh, C. Orlenius, C. Picher, and C. Puente, "Advances in antenna technology for wireless handheld devices," *International Journal of Antennas and Propagation*, vol. 2013, Article ID 838364, 25 pages, 2013.
- [5] Y.-L. Ban, J.-H. Chen, J.-L.-W. Li, and Y. Wu, "Small-size printed coupled-fed antenna for eight-band LTE/GSM/UMTS wireless wide area network operation in an internal mobile handset," *IET Microwaves, Antennas and Propagation*, vol. 7, no. 6, pp. 399–407, 2013.
- [6] C.-W. Yang, Y.-B. Jung, and C. W. Jung, "Octaband internal antenna for 4G mobile handset," *IEEE Antennas and Wireless Propagation Letters*, vol. 10, pp. 817–819, 2011.
- [7] K.-L. Wong and W.-Y. Chen, "Small-size printed loop-type antenna integrated with two stacked coupled-fed shorted strip

- monopoles for eight-band LTE/GSM/UMTS operation in the mobile phone,” *Microwave and Optical Technology Letters*, vol. 52, no. 7, pp. 1471–1476, 2010.
- [8] Y. Hong, J. Tak, J. Baek, B. Myeong, and J. Choi, “Design of a multiband antenna for LTE/GSM/UMTS band operation,” *International Journal of Antennas and Propagation*, vol. 2014, Article ID 548160, 9 pages, 2014.
  - [9] Y.-J. Ren, “Ceramic based small LTE MIMO handset antenna,” *IEEE Transactions on Antennas and Propagation*, vol. 61, no. 2, pp. 934–938, 2013.
  - [10] F.-H. Chu and K.-L. Wong, “Planar printed strip monopole with a closely-coupled parasitic shorted strip for eight-band LTE/GSM/UMTS mobile phone,” *IEEE Transactions on Antennas and Propagation*, vol. 58, no. 10, pp. 3426–3431, 2010.
  - [11] S.-C. Chen and K.-L. Wong, “Small-size 11-band LTE/WWAN/WLAN internal mobile phone antenna,” *Microwave and Optical Technology Letters*, vol. 52, no. 11, pp. 2603–2608, 2010.
  - [12] K.-L. Wong and M.-T. Chen, “Small-size LTE/WWAN printed loop antenna with an inductively coupled branch strip for bandwidth enhancement in the tablet computer,” *IEEE Transactions on Antennas and Propagation*, vol. 61, no. 12, pp. 6144–6151, 2013.
  - [13] R. Valkonen, J. Ilvonen, C. Icheln, and P. Vainikainen, “Inherently non-resonant multi-band mobile terminal antenna,” *Electronics Letters*, vol. 49, no. 1, pp. 11–13, 2013.
  - [14] L. Li, Z. Jia, F. F. Huo, and W. Q. Han, “A novel compact multi-band antenna employing dual-band CRLH-TL for smart mobile phone application,” *IEEE Antennas and Wireless Propagation Letters*, vol. 12, pp. 1688–1691, 2013.
  - [15] T.-W. Kang, K.-L. Wong, and M.-F. Tu, “Internal handset antenna array for LTE/WWAN and LTE MIMO operations,” in *Proceedings of the 5th IEEE European Conference on Antennas and Propagation (EUCAP '11)*, pp. 557–560, April 2011.
  - [16] J. M. J. W. Jayasinghe and D. Uduwawala, “A novel multiband miniature planar inverted F antenna design for bluetooth and WLAN applications,” *International Journal of Antennas and Propagation*, vol. 2015, Article ID 970152, 6 pages, 2015.
  - [17] S. Risco, J. Anguera, A. Andújar, A. Pérez, and C. Puente, “Coupled monopole antenna design for multiband handset devices,” *Microwave and Optical Technology Letters*, vol. 52, no. 2, pp. 359–364, 2010.

## Research Article

# Equilateral Triangular Dielectric Resonator Nantenna at Optical Frequencies for Energy Harvesting

**Waleed Tariq Sethi,<sup>1,2</sup> Hamsakutty Vettikalladi,<sup>3</sup> Habib Fathallah,<sup>1,3</sup> and Mohamed Himdi<sup>2</sup>**

<sup>1</sup>KACST Technology Innovation Center in Radio Frequency and Photonics for the e-Society (RFTONICS), King Saud University, Riyadh 11451, Saudi Arabia

<sup>2</sup>Institute of Electronics and Telecommunications of Rennes University (IETR), University of Rennes 1, 35700 Rennes, France

<sup>3</sup>Electrical Engineering Department, King Saud University, P.O. Box 800, Riyadh 11421, Saudi Arabia

Correspondence should be addressed to Waleed Tariq Sethi; wsethi@ksu.edu.sa

Received 7 May 2015; Revised 20 August 2015; Accepted 31 August 2015

Academic Editor: Giuseppe Mazzarella

Copyright © 2015 Waleed Tariq Sethi et al. This is an open access article distributed under the Creative Commons Attribution License, which permits unrestricted use, distribution, and reproduction in any medium, provided the original work is properly cited.

The last decade has witnessed a remarkable growth in the telecommunication industry. With the introduction of smart gadgets, the demand for high data rate and bandwidth for wireless applications have increased exponentially at the cost of exponential consumption of energy. The latter is pushing the research and industry communities to devise green communication solutions that require the design of energy saving devices and techniques in one part and ambient energy harvesting techniques in the other part. With the advent of nanocomponents fabrication technology, researchers are now able to tap into the THz frequency regime and fabricate optical low profile antennas at a nanoscale. Optical antennas have proved their potential and are revolutionizing a class of novel optical detectors, interconnectors, sensors, and energy harvesting related fields. Authors in this paper propose an equilateral triangular dielectric resonator nantenna (ETDRNA) working at 193.5 THz standard optical frequency. The simulated antenna achieves an impedance bandwidth from 192.3 THz to 197.3 THz with an end-fire directivity of 8.6 dBi, covering the entire standard optical window of C-band. Numerical demonstrations prove the efficiency of the nantenna at the frequencies of interest, making it a viable candidate for future green energy harvesting and high speed optical applications.

## 1. Introduction

Antennas are found around us in abundance when we are in the midst of communicating either locally or globally via radio frequencies or microwave technologies. Since the inception of classical electromagnetics to the wonders of modern electromagnetism [1], antennas in any size or form have and are still working diligently to uphold their purpose, that is, to convert the electromagnetic energy available in free space into confined electric signals and vice versa. As the telecommunication industry is reaching new technological heights, the demand for energy consumption is also surging, resulting in an increase in environmental problems in the form of carbon emissions [2]. One proposed solution is the concept of “green communication,” which primarily aims at improving the energy efficiency while reducing the CO<sub>2</sub>

emissions and energy consumption of communication networks [3]. In order to realize this concept, researchers are now persuaded on designing antennas by utilizing the electromagnetic spectrum in the high frequency bands (THz), which fulfills the bandwidth hunger requirements of smart devices, provides low cost designs with high connectivity, and satisfies the consumer needs while keeping the environment clean and energy consumption to a minimum. The antennas designed in the THz regime are given the name of optical antennas.

Optical antennas are a quite new concept in physical optics. They were initially developed for optical microscopic applications. Their basic principle of operation lies in their ability to confine light to subwavelength volumes, plasmonic nanoparticles, and nanoantennas, providing a fundamental link between electronic and photonic circuits by associating the large size mismatch between the electronic and photonic

wave functions [4]. Optical antennas have some similarities to their radio frequency (RF) and microwave counterparts, but major differences arise with their physical properties and scalable behaviors. The major difference among the two counterparts is in terms of interaction of electromagnetic waves with metals. This term is known as Plasmon's at optical frequencies, where the EM waves interact with noble metals, that is, silver, gold, and aluminum, which are not perfect conductors. These noble metals are defined and solved via Drude model equations [5]. Optical antennas have now started to gain popularity among the researchers and scientists. Few years back, optical antennas were not so popular because of limited fabrication techniques and equipment. With the advent of nanoscience and nanotechnology machine fabrication, optical antennas can now be realized to solve the problem of high data rates, wide bandwidth, and environmental problems, that is, CO<sub>2</sub> emissions. Also working with antennas at higher frequency bands (THz), the researchers are introduced to an insight to the natural and analytical properties of nanofabrication and nanoantenna designs. Figure 1 shows various fabrication techniques. Interested readers, about these techniques, are referred to the list of pioneering research publications [6–10]. Apart from fabrication, some of the excitation techniques for optical nantennas can be performed (1) through a coupling of light using the so called nanotapers [11, 12]. Since nanoantennas cannot handle much power because of their small footprints, this makes them ideal candidates for being excited by micro lasers such as micro disks and photonic crystal lasers. Another method of excitation, which outperforms the former micro laser based technique by reducing the reflection induced power loss, exploits (2) slot dielectric waveguides [13]. It is evident that the fabrication of optical antenna structures provides an emerging opportunity for realizing new optoelectronic devices with importance in applications such as photo detection, light emission, sensing, energy harvesting, and spectroscopy.

Analysis of traditional antenna design provides great opportunity for the research industry to design and analyze nanoantennas at optical frequencies. Apart from many designs, keeping in view of wide band characteristics at THz regime, one such design is making use of dielectric resonator antennas (DRAs), firstly proposed and realized in 1939 by Richtmyer, and their modes were first analyzed by Okaya and Barash in the 1960s [14, 15]. DRAs' physical and electrical properties allow them to be flexible and diversely suited to any communication application. In microwaves, DRAs are nonmetallized dielectric objects normally made of ceramics with high permittivity (relative dielectric constants of the order of 10–300) which are used as resonant cavities for storage of electromagnetic (EM) energy. Compared to metallic antennas, which produce high radiation losses at higher frequencies, DRAs with low loss dielectric materials have some advantages such as high radiation efficiency due to lack of surface waves, small size proportion to wavelength, wide impedance bandwidth, many feeding arrangements, numerous geometries, and different excitation methods with several modes producing broadside or end-fire radiation patterns [16–24].

In this paper, drawing inspiration from traditional radio and microwave design [24] and benefiting from DR characteristics, we propose and explore simulated design of an equilateral triangular dielectric resonating nantenna (ETDRNA), for the first time to the best of our knowledge, at optical frequencies. Apart from many applications [9, 10], in this paper, we address the nantenna design for solar energy harvesting application. Since the introduction of the preliminary concept four decades ago, very limited work has been done because of the unavailability of nanomaterial fabrication techniques [25–27]. Nowadays, whether nanofabrication progressively became less challenging, the testing, measurement, and characterization of nantennas are still experimentally hard and very expensive. However, these limitations did not stop research community from continuing their work with high frequencies designs using theoretical and numerical modelling and performance investigation [28–31]. Keeping with the state of the art, we propose, numerically simulate, and investigate a nantenna consisting of "Ag-SiO<sub>2</sub>-Ag" structure. The dielectric resonator is made of "Si" having an equilateral triangular shape. The nantenna is excited via a nanostrip transmission line made of a noble metal silver "Ag." The theory of Drude model is used to analyze and examine the conductive properties of the noble metal "Ag." It is worthy to note that the proposed nantenna can be operated as a receiving antenna for future green communication systems. The antenna exhibits a wide impedance bandwidth of 2.58% (192.3 THz–197.3 THz) at a center frequency of 193.5 THz, covering the entire standard optical C-band transmission widow. The achieved directivity of the nantenna is 8.6 dBi with end-fire radiation pattern. The obtained results make it a viable candidate for a green-field approach that takes into account the reduction of carbon footprints generated by human activity in the last decade.

## 2. Proposed Antenna Configuration

The proposed configuration (side view and top view) of the equilateral triangular dielectric resonator nantenna (ETDRNA), designed to operate as a receiving antenna for capturing energy in free space, in the standard optical communication band at a wavelength of 1.55 μm, is shown in Figures 2(a) and 2(b). The corresponding central frequency is 193.5 THz. The dimensions of the simulated antenna consist of a "SiO<sub>2</sub>" substrate with a thickness of  $h_1 = 0.150 \mu\text{m}$ ,  $\epsilon_r = 2.09$ , and loss tangent  $\tan \delta = 0$  [32]. The ground plane is on the bottom side with a partial rectangular geometry with optimized dimensions of  $W_g \times L_g$  having a thickness of  $t = 0.010 \mu\text{m}$  and nanostrip on the top side with a thickness,  $h_2 = 0.025 \mu\text{m}$ . The ground and the nanostrip are made up of silver (Ag). The dimensions of the substrate are taken as  $W \times L = 5 \times 5 \mu\text{m}^2$ . The equilateral triangular dielectric is made of silicon "Si," with  $\epsilon_r = 11.9$  and estimated loss tangent  $\tan \delta = 0.003$  at 100 THz [33, 34]. The antenna is excited via the 50 Ω silver nanostrip feed that has a width of  $W_f$  and optimized length of  $L_f$ . In order to control the matching at the central frequency of 193.5 THz and to achieve a wide bandwidth with acceptable radiation patterns the same "SiO<sub>2</sub>" substrate material with thickness  $h_3 = 0.015 \mu\text{m}$

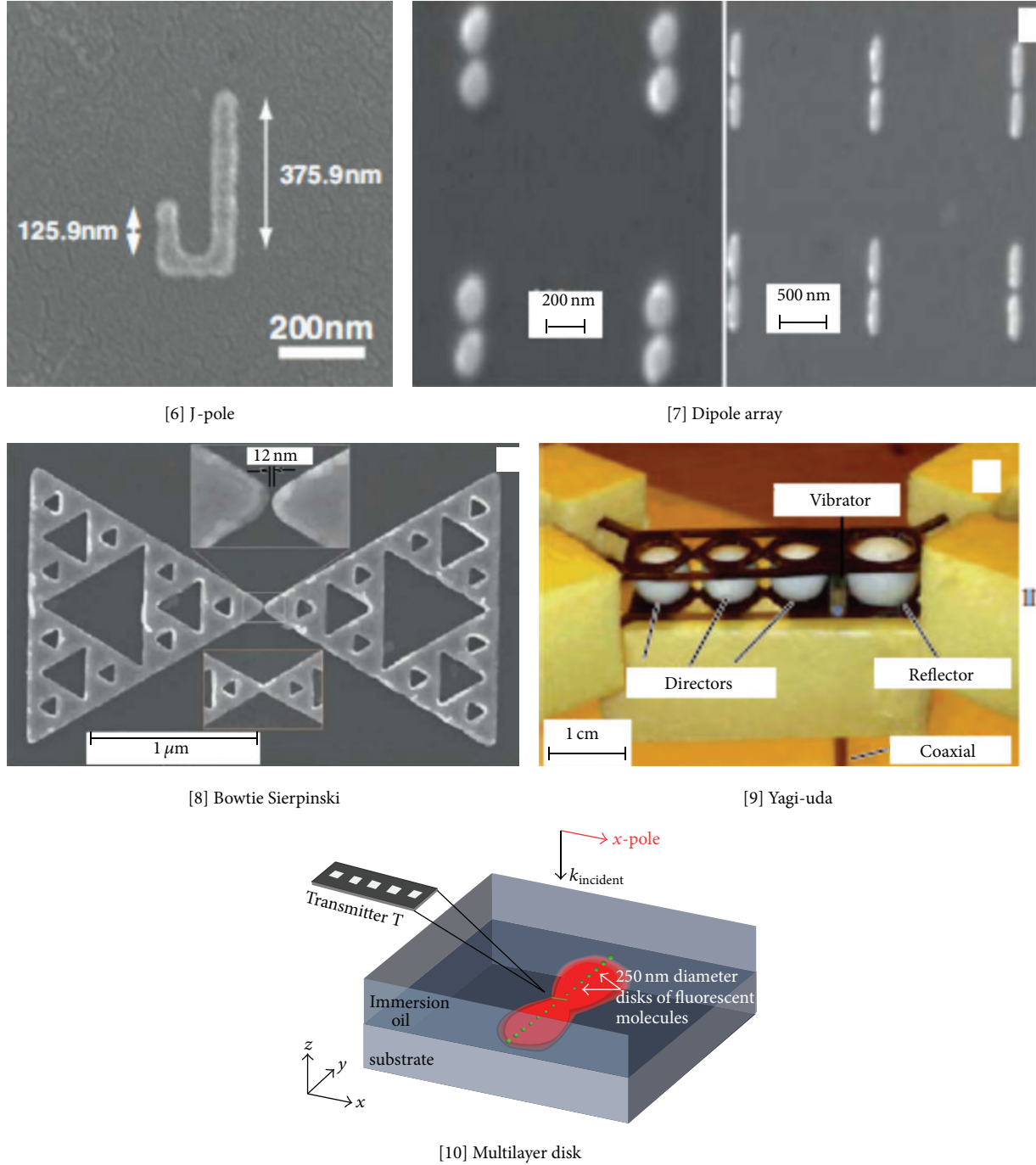


FIGURE 1: Various nanoantennas fabricated with different techniques. Source [6–10].

has been introduced between the equilateral triangle and the nanostrip. The dimensions of the equilateral triangular dielectric are calculated from the following [23, 24]:

$$f_{mn} = \frac{c}{2\sqrt{\epsilon_r}} \left[ \sqrt{\left(\frac{4}{3a}\right)^2 + \left(\frac{p}{h}\right)^2} \right]^{1/2}, \quad (1)$$

where “ $a$ ” is the side length of the equilateral triangular DRA,  $\epsilon_r$  is the dielectric constant of the DRA, “ $h$ ” is two times

the height of the triangular DRA to account for the image effect of the ground plane, and  $p = 1$  for the fundamental mode [24]. The three integers  $l$ ,  $m$ , and  $n$  have a relation of  $(l + mn + n = 0)$  but are not zero simultaneously. For a low-profile triangular DRA, we have  $a \gg h$ , and therefore the following demonstrates that the frequency is predominantly determined by the height of the DRA:

$$f_r = \frac{c}{4h\sqrt{\epsilon_r}}, \quad (2)$$

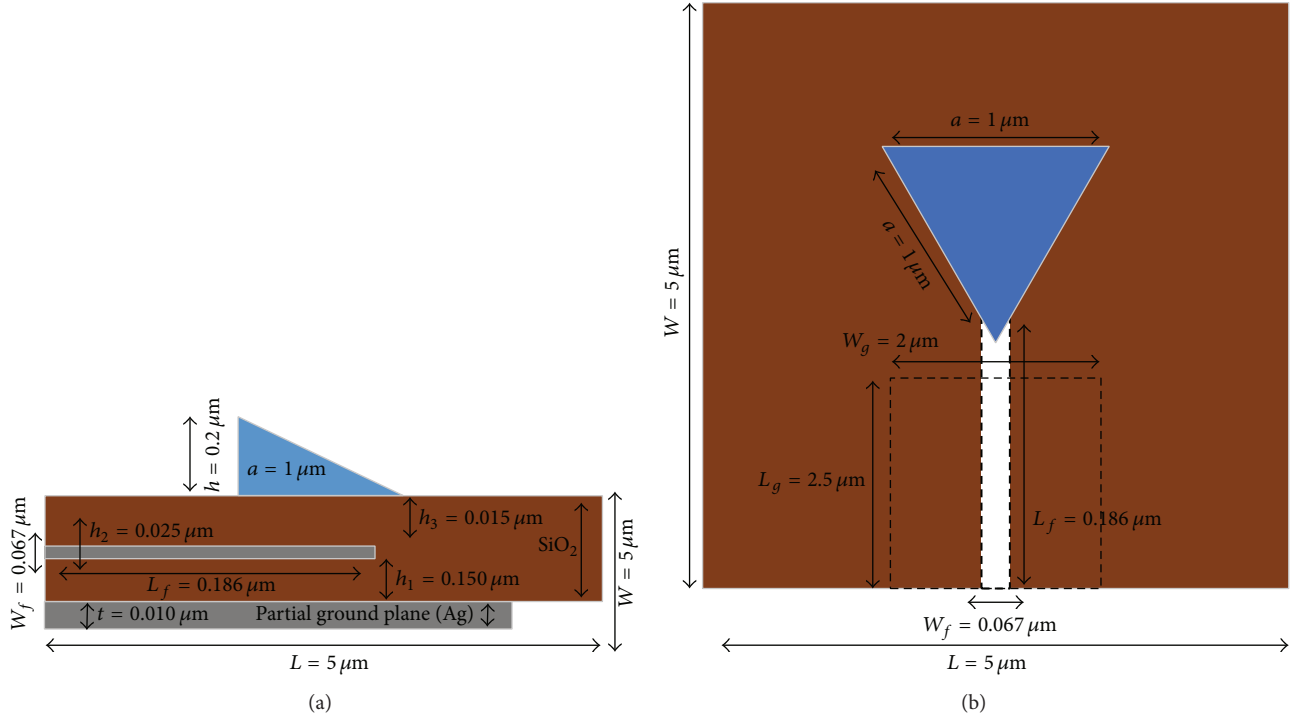


FIGURE 2: (a) Side view of ETDRNA. (b) Top view of ETDRNA with equal side lengths “ $a$ .”

where  $h$  and  $\epsilon_r$  are the height and dielectric constant of triangular DRA.

Since, at optical frequencies, metals appear with a negative permittivity therefore complex permittivity  $\epsilon_{\text{Ag}}$  of silver (Ag) was calculated from (3) explained by the Drude model [32]:

$$\epsilon_{\text{Ag}} = \epsilon_o \left\{ \epsilon_{\infty} - \frac{f_p^2}{[f(f + i\gamma)]} \right\} = -129.17 + j3.28, \quad (3)$$

where  $\epsilon_o = 8.85 \times 10^{-12} [\text{F/m}]$ ,  $\epsilon_{\infty} = 5$ , plasmonic frequency  $f_p = 1.41e^{16} \text{ rad/s}$ ,  $f$  = central frequency, and collision frequency  $\gamma = 2.98e^{13}$ . The proposed model has taken into account the conductive and dielectric losses and has been simulated in commercially available EM simulator CST MWS 2014 based on FIT numerical technique using optical template.

### 3. Parametric Studies

For understanding the role of each geometric design of the proposed dielectric triangular nantenna structure, various parameters were extensively optimized. In order to study the effects on the antenna performance in terms of bandwidth and directivity, the following parameters were studied and analyzed.

**3.1. Nanostrip Feed.** The silver nanostrip characterized by Drude model was optimized in terms of its length and width. The traditional empirical formulas [1] were used as a starting point for the nanostrip design. The nanostrip acts like a

coupling resonator that excites the triangular dielectric place on an upper  $\text{SiO}_2$  substrate with height  $h_3$ . Traditionally at RF frequencies the length of the transmission lines is characterized to the wavelengths ( $\lambda$ ) of incoming and outgoing radiations. However working at the optical frequencies, the traditional RF wavelength characteristics scenario no longer applies as the incident waves are not perfectly reflected back from the metal's surface. Instead, radiation penetrates into the metal giving rise to the excitation of the free electron gas. Hence, at optical frequencies, instead of using the traditional wavelength ( $\lambda$ ) we make use of shorter effective wavelength ( $\lambda_{\text{eff}}$ ) which depends on the material properties [35, 36] given by the following equation for length of a transmission line [37]:

$$\frac{m\lambda_{\text{eff}}}{2} = L(\lambda_0), \quad (4)$$

where (4) shows the relationship between the free space wavelength ( $\lambda_0$ ) and the effective wavelength ( $\lambda_{\text{eff}}$ ) and the order of resonance ( $m$ ). Here effective wavelength is given by

$$\lambda_{\text{eff}} = \frac{\lambda_0}{n_{\text{eff}}}. \quad (5)$$

Typical values of  $n_{\text{eff}}$  have been measured to be in the range of 1.5–3 [38]. In our simulation, for the silver nanostrip design, the selected  $n_{\text{eff}} = 2.8$  [39] resulted in the minimum resonating length of the nanostrip being  $0.27 \mu\text{m}$ . The length  $L_f$  of the nanostrip was optimized from  $0.1 \mu\text{m}$  to  $0.27 \mu\text{m}$  with the best optimized value producing required resonance at 193.5 THz which was at  $L_f = 0.186 \mu\text{m}$  as shown in

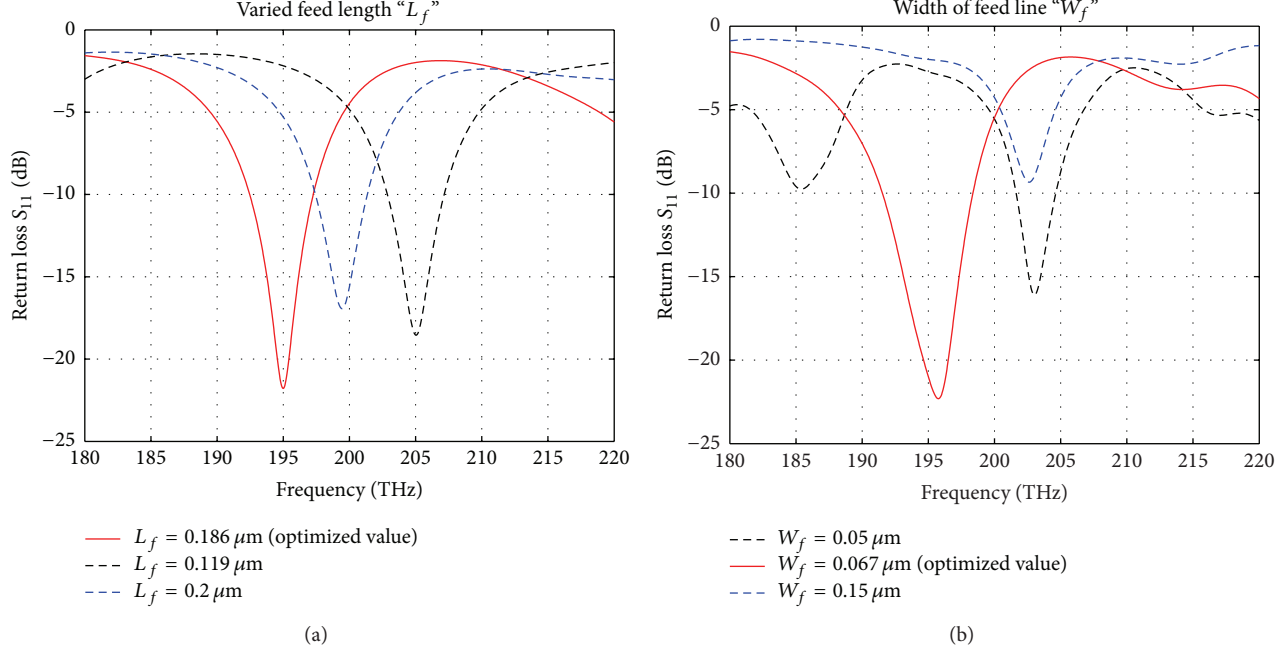


FIGURE 3: Optimized parameters. (a) Length of nanostrip. (b) Width of nanostrip.

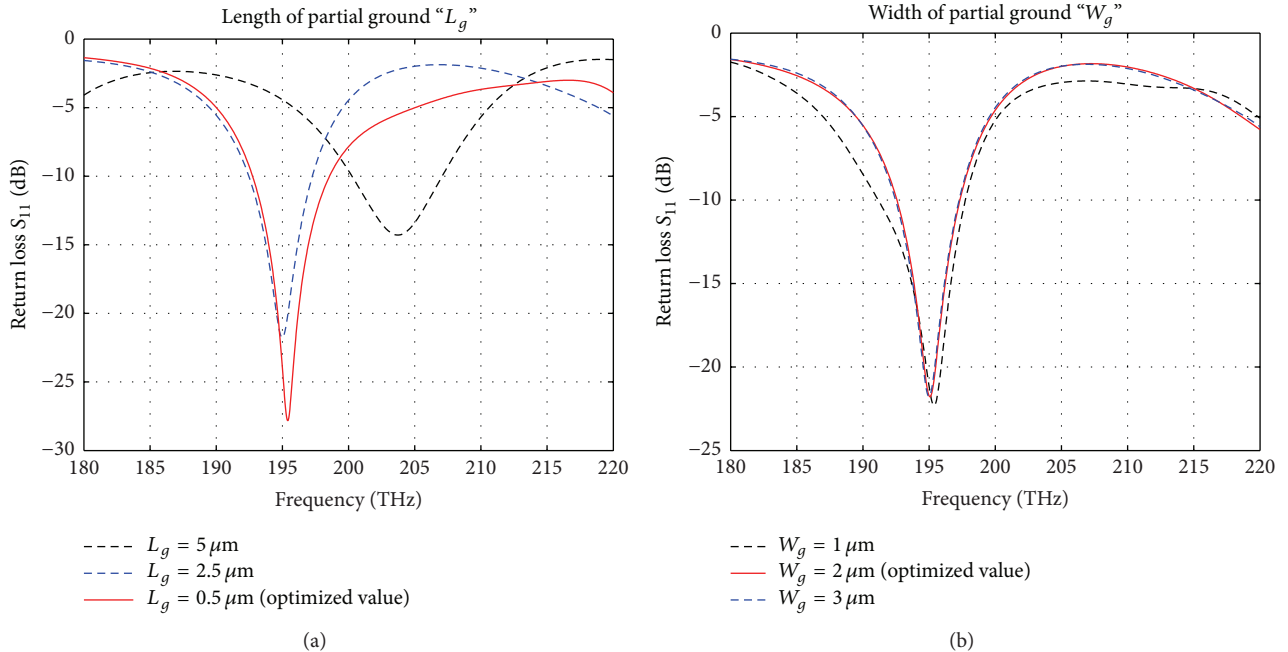


FIGURE 4: Optimized parameters. (a) Length of partial ground. (b) Width of partial ground.

Figure 3(a). The effect of the width " $W_f$ " of the nanostrip was also examined by extensive parametric studies. Initial values were taken from the empirical formulas [1] and optimization was done from  $0.02 \mu\text{m}$  to  $0.28 \mu\text{m}$ . Figure 3(b) shows the best optimized value achieved at resonance of  $-22 \text{ dB}$  with  $W_f = 0.067 \mu\text{m}$ .

**3.2. Partial Ground Plane.** Effects of the ground plane were studied on the nanoantenna design. Initially a finite ground

plane was used to achieve a good radiation pattern with an acceptable bandwidth. The ground plane was then optimized and a partial ground plane was selected with dimensions  $L_g \times W_g = 0.5 \mu\text{m} \times 2 \mu\text{m}$ . Figures 4(a) and 4(b) show the effects of varying the ground plane in terms of its length and width. The optimized results produce a wide impedance bandwidth of 2.5% (192.3 THz–197.3 THz) at a center frequency of 193.5 THz, covering all of the standard optical transmission widow (C-band), with a directivity of 8.6 dB.

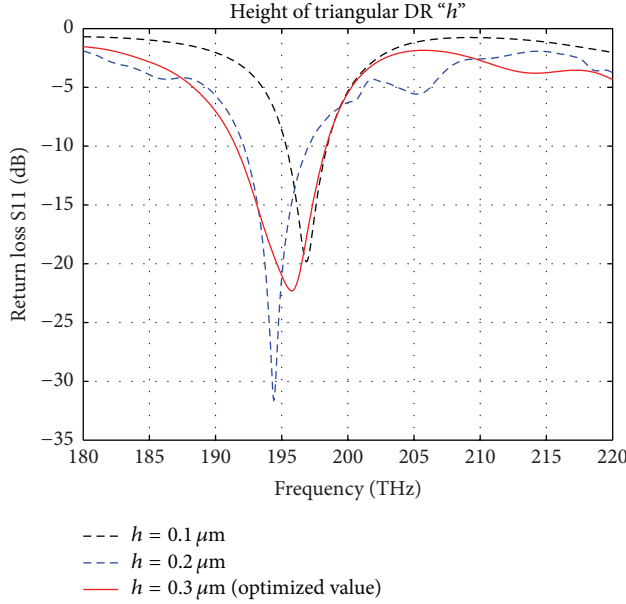


FIGURE 5: Varied height of triangular DR.

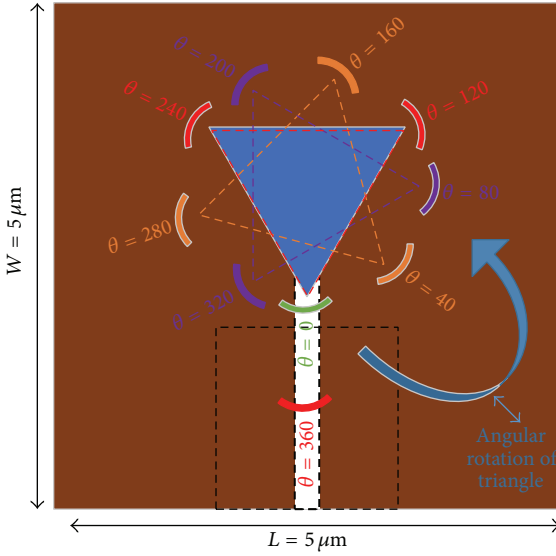


FIGURE 6: Angular rotation of triangular DR.

**3.3. Height of Triangular DR.** Since the height of the triangular DR predominately determines the resonance frequency according to (2), the height  $h$  of the DR was optimized from  $0.1 \mu\text{m}$  to  $0.5 \mu\text{m}$ . Figure 5 shows the best optimized value of  $h = 0.3 \mu\text{m}$  having a resonance at  $-23 \text{ dB}$ .

**3.4. Rotation of Triangular DR.** In order to study the effects of bandwidth, frequency shift, and directivity of the nanoantenna design, the triangular DR was rotated on its axis. The rotation was from  $0^\circ$  to  $360^\circ$  with an angular spacing of  $40^\circ$ . Figure 6 shows the angular rotation of the triangular DR. The tip of the triangle was initially aligned at  $0^\circ$  shown in green color. The DR was then rotated along the counterclockwise

direction with varying angles. It was observed that, with the rotation of the DR, the bandwidth remained the same at 2.5% but the resonant frequency shifted to other bands ( $200 \text{ THz} - 205 \text{ THz}$ ) in the frequency range from  $180 \text{ THz}$  to  $220 \text{ THz}$  as shown in Figure 7(a). Since the triangle is an equilateral one, the angular rotation produces the same shifts at other angles; that is, the shift will be the same at  $0 = 120 = 240 = 360$  degrees as shown in Figure 7(b). The directivity was also affected with the rotation of the triangle as shown in Figure 7(b). It is clear that the effect of the rotation of the triangular DR lowers the directivity to nearly  $3 \text{ dBi}$ .

After performing the above parametric studies, optimized geometric parameters of the proposed ETDRNA, resulting in

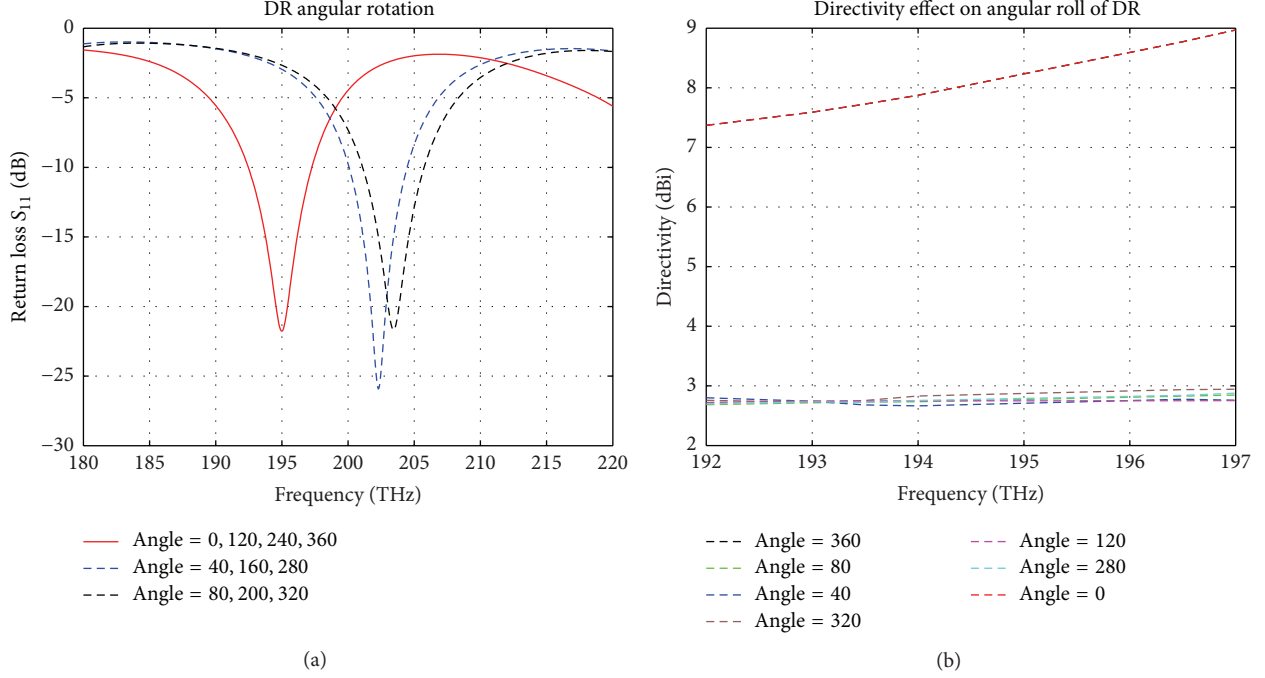
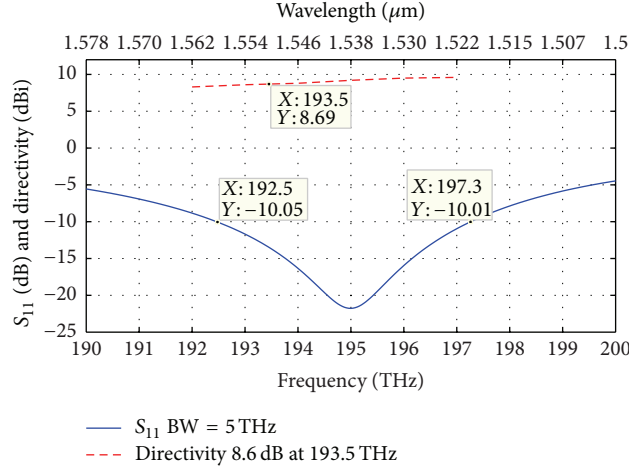


FIGURE 7: (a) Angular rotation effect on resonant frequency. (b) DR's angular rotation effect on directivity.

FIGURE 8: Return loss  $S_{11}$  and directivity of ETDRNA.

a wide impedance bandwidth of 2.5% (192.3 THz–197.3 THz) and a directivity of 8.6 dB, are displayed in Table 1. It was also observed that while keeping the antenna with optimized parameters as listed in Table 1, the simple triangular nantenna structure can act as a tunable resonator when rotated around its axis resulting in usage of applications that work in the wavelengths in the range of 1463 nm–1500 nm. The proposed design, if facility exists, can be fabricated via the techniques mentioned in [6–10]. In our case, the fabrication will follow a bottom-up approach where the quartz or  $\text{SiO}_2$  substrate will have silver deposited on its surface.

#### 4. Results

The simulated return loss ( $S_{11}$ ) and directivity of the nanoantenna are shown in Figure 8. The 3D radiation patterns of the nanoantenna at 192 THz, 193.5 THz, and 197 THz are shown in Figures 9(a)–9(c). The ETDRNA exhibits resonance frequency at 193.5 THz ( $\lambda_0 = 1.55 \mu\text{m}$ ) with maximum dip around -22 dB. The antenna covers most part of the S-band and all the portion of the C-band in optical domain and can be used for relevant optical applications in nanonetworks, high speed optical data transfer, and harvesting energy.

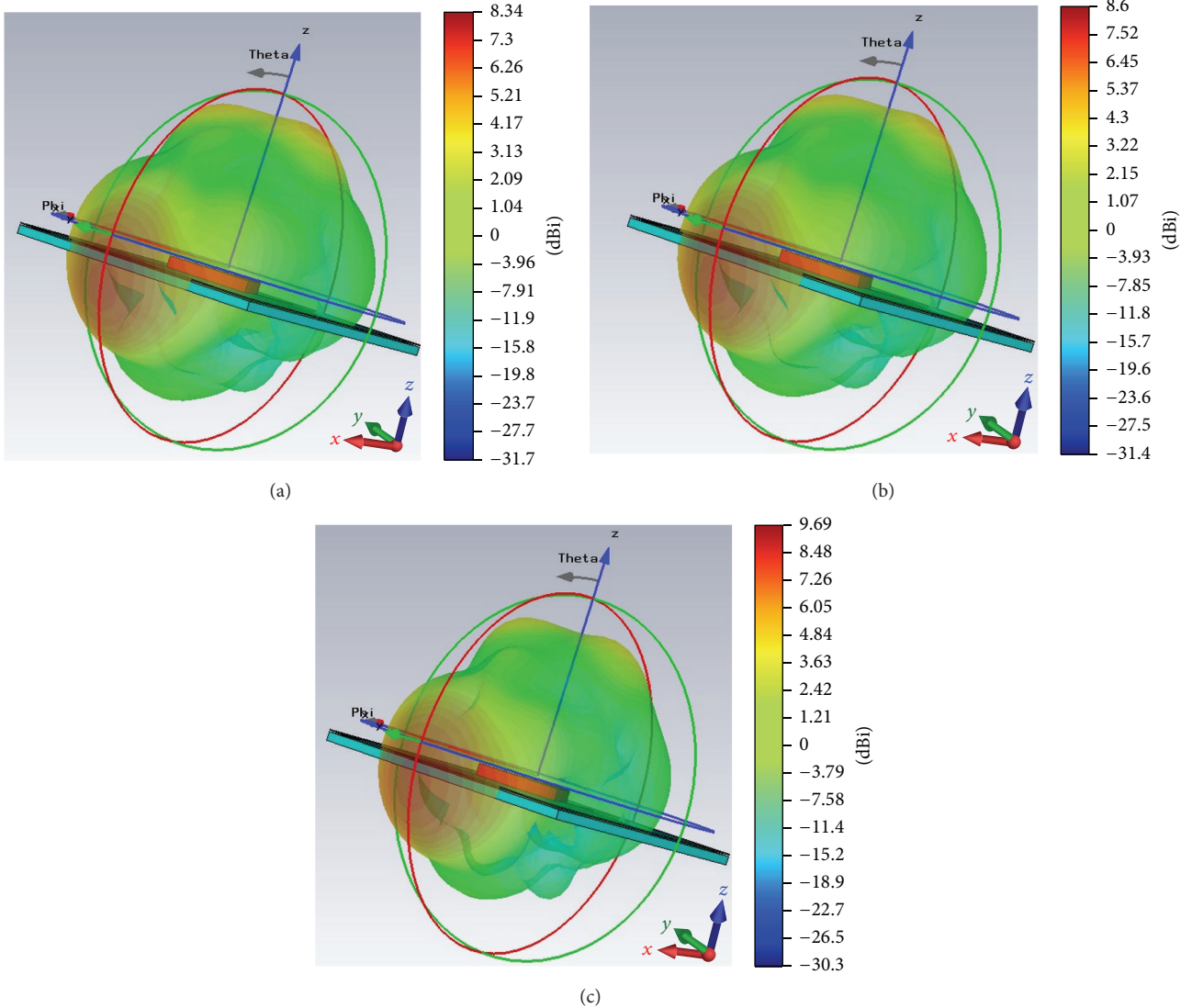


FIGURE 9: (a) 3D end-fire pattern at 192.5 THz. (b) 3D end-fire pattern at 193.5 THz. (c) 3D end-fire pattern at 197 THz.

The directivity of the antenna is 8.6 dBi. Examining the 3D radiation patterns in Figure 9 provides the proof of the ETDRNA radiating in end-fire pattern.

## 5. Conclusion

In this paper, we have proposed an equilateral triangular dielectric resonator nantenna for next-generation green communication that could be in the form of solar energy harvesting at the infra-red range and optical wireless charging and for high speed optical communication applications. The nantenna is composed of a “Ag-SiO<sub>2</sub>-Ag” structure with a nanosilver “Ag” transmission line that excites a triangular dielectric made of “Si” material. The antenna yields a wide impedance bandwidth of 2.58% (192.3 THz–197.3 THz) with a high directive radiation pattern of 8.6 dBi at 193.5 THz (1.55 μm) with an end-fire radiation pattern. At present, the nanofabrication technology is limited and the proposed

TABLE 1: Optimized parameters of ETDRNA.

Parameters	Value (μm)
Feed length $L_f$	0.186
Feed width $W_f$	0.067
Ground length $L_g$	2.5
Ground width $W_g$	2
Height of triangular DR $h$	0.2
Area of triangular side $a$	1
Rotation angle $\theta$	0°

design is a theoretical one, yet we believe that our contribution in the fast growing field of nantennas, with the proposed ETDRNA design, will prove itself to be a promising candidate for next-generation energy harvesting and green sustainable solution applications based on nanotechnology designs.

## Conflict of Interests

The authors declare that there is no conflict of interests regarding the publication of this paper.

## Acknowledgment

This research is supported by King Abdul Aziz City for Science and Technology (KACST) Technology Innovation Center in RF and Photonics for the e-Society (RFTONICS) hosted at King Saud University.

## References

- [1] C. Balanis, *Antenna Theory: Analysis and Design*, John Wiley & Sons, New York, NY, USA, 2005.
- [2] M. H. Alsharif, R. Nordin, and M. Ismail, "Survey of green radio communications networks: techniques and recent advances," *Journal of Computer Networks and Communications*, vol. 2013, Article ID 453893, 13 pages, 2013.
- [3] T. Kuwashima, K. Sekimoto, K. Kawai et al., "Neutralize CO<sub>2</sub> emissions by product contributions," in *Proceedings of the Electronics Goes Green (ECG '12)*, Beijing, China, September 2012.
- [4] G. N. Malheiros-Silveira, L. H. Gabrielli, C. J. Chang-Hasnain, and H. E. Hernandez-Figueroa, "Breakthroughs in photonics 2013: advances in nanoantennas," *IEEE Photonics Journal*, vol. 6, no. 2, Article ID 0700706, 2014.
- [5] M. Dressel and M. Scheffler, "Verifying the Drude response," *Annalen der Physik*, vol. 15, no. 7-8, pp. 535–544, 2006.
- [6] S. H. Choudhury, M. I. Momtaz, and M. A. Matin, "Analytical deduction of the salient properties of a half wavelength J-pole antenna," in *Proceedings of the International Conference on Computational Intelligence and Communication Networks (C/CN '10)*, pp. 32–35, IEEE, Bhopal, India, November 2010.
- [7] A. Alù and N. Engheta, "Hertzian plasmonic nanodimer as an efficient optical nanoantenna," *Physical Review B—Condensed Matter and Materials Physics*, vol. 78, no. 19, Article ID 195111, 2008.
- [8] L. Rosa, K. Sun, and S. Juodkazis, "Sierpiński fractal plasmonic nanoantennas," *Physica Status Solidi—Rapid Research Letters*, vol. 5, no. 5-6, pp. 175–177, 2011.
- [9] L. Novotny and B. Hecht, *Principles of Nano-Optics*, Cambridge University Press, Cambridge, UK, 2006.
- [10] D. Dregely, K. Lindfors, M. Lippitz, N. Engheta, M. Totzeck, and H. Giessen, "Imaging and steering an optical wireless nanoantenna link," *Nature Communications*, vol. 5, article 4354, 2014.
- [11] H. T. Hattori, Z. Li, D. Liu, I. D. Rukhlenko, and M. Premaratne, "Coupling of light from microdisk lasers into plasmonic nano-antennas," *Optics Express*, vol. 17, no. 23, pp. 20878–20884, 2009.
- [12] Z. Li, H. T. Hattori, L. Fu, H. H. Tan, and C. Jagadish, "Merging photonic wire lasers and nanoantennas," *Journal of Lightwave Technology*, vol. 29, no. 18, Article ID 5892863, pp. 2690–2697, 2011.
- [13] H. T. Hattori, Z. Li, and D. Liu, "Driving plasmonic nanoantennas with triangular lasers and slot waveguides," *Applied Optics*, vol. 50, no. 16, pp. 2391–2400, 2011.
- [14] R. D. Richtmyer, "Dielectric resonators," *Journal of Applied Physics*, vol. 10, no. 6, pp. 391–398, 1939.
- [15] A. Okaya and L. F. Barash, "The dielectric microwave resonator," *Proceedings of the IRE*, vol. 50, no. 10, pp. 2081–2092, 1962.
- [16] A. Petosa, A. Ittipiboon, Y. M. M. Antar, D. Roscoe, and M. Cuhaci, "Recent advances in dielectric-resonator antenna technology," *IEEE Antennas and Propagation Magazine*, vol. 40, no. 3, pp. 35–48, 1998.
- [17] K. M. Luk and K. W. Leung, *Dielectric Resonator Antennas*, Research Studies Press, Hertfordshire, UK, 2002.
- [18] R. K. Mongia and P. Bhartia, "Dielectric resonator antennas—a review and general design relations for resonant frequency and bandwidth," *International Journal of Microwave and Millimeter-Wave Computer-Aided Engineering*, vol. 4, no. 3, pp. 230–247, 1994.
- [19] I. E. Hashem, N. H. Rafat, and E. A. Soliman, "Nanocrescent antenna as a transceiver for optical communication systems," in *Proceedings of the IEEE International Symposium on Electromagnetic Compatibility (EMC '14)*, pp. 39–45, IEEE, Raleigh, NC, USA, August 2014.
- [20] M. W. McAllister, S. A. Long, and G. L. Conway, "Rectangular dielectric resonator antenna," *Electronics Letters*, vol. 19, no. 6, pp. 218–219, 1983.
- [21] R. K. Mongia, A. Ittipiboon, Y. M. M. Antar, P. Bhartia, and M. Cuhaci, "Half-split cylindrical dielectric resonator antenna using slot-coupling," *IEEE Microwave and Guided Wave Letters*, vol. 3, no. 2, pp. 38–39, 1993.
- [22] A. A. Kishk, G. Zhou, and A. W. Glisson, "Analysis of dielectric resonator antennas with emphasis on hemispherical structures," *IEEE Antennas and Propagation Magazine*, vol. 36, no. 2, pp. 20–30, 1994.
- [23] H. Y. Lo, K. W. Leung, K. M. Luk, and E. K. N. Yung, "Low profile equilateral-triangular dielectric resonator antenna of very high permittivity," *Electronics Letters*, vol. 35, no. 25, pp. 2164–2166, 1999.
- [24] A. A. Kishk, "A triangular dielectric resonator antenna excited by a coaxial probe," *Microwave and Optical Technology Letters*, vol. 30, no. 5, pp. 340–341, 2001.
- [25] R. L. Bailey, "A proposed new concept for a solar-energy converter," *Journal of Engineering for Power*, vol. 94, no. 2, pp. 73–77, 1972.
- [26] M. Midrio, S. Boscolo, A. Locatelli, D. Modotto, C. De Angelis, and A.-D. Capobianco, "Flared monopole antennas for 10 μm energy harvesting," in *Proceedings of the 13th European Microwave Conference (EuMC '10)*, pp. 1496–1499, September 2010.
- [27] I. Kocakarin and K. Yegin, "Glass superstrate nanoantennas for infrared energy harvesting applications," *International Journal of Antennas and Propagation*, vol. 2013, Article ID 245960, 7 pages, 2013.
- [28] D. Sikdar, W. Cheng, and M. Premaratne, "Optically resonant magneto-electric cubic nanoantennas for ultra-directional light scattering," *Journal of Applied Physics*, vol. 117, no. 8, Article ID 083101, 2015.
- [29] E. Rusak, I. Staude, M. Decker et al., "Hybrid nanoantennas for directional emission enhancement," *Applied Physics Letters*, vol. 105, no. 22, Article ID 221109, 2014.
- [30] S.-W. Qu and Z.-P. Nie, "Plasmonic nanopatch array for optical integrated circuit applications," *Scientific Reports*, vol. 3, article 3172, 2013.
- [31] F. J. Rodríguez-Fortuño, D. Puerto, A. Griol, L. Bellieres, J. Martí, and A. Martínez, "Sorting linearly polarized photons with a single scatterer," *Optics Letters*, vol. 39, no. 6, pp. 1394–1397, 2014.

- [32] P. B. Johnson and R. W. Christy, "Optical constants of the noble metals," *Physical Review B*, vol. 6, no. 12, pp. 4370–4379, 1972.
- [33] R. Sinha, M. Karabiyik, C. Al-Amin, P. K. Vabbina, D. Ö. Güney, and N. Pala, "Tunable room temperature THz sources based on nonlinear mixing in a hybrid optical and THz micro-ring resonator," *Scientific Reports*, vol. 5, article 9422, 2015.
- [34] P. H. Bolivar, M. Brucherseifer, J. G. Rivas et al., "Measurement of the dielectric constant and loss tangent of high dielectric-constant materials at terahertz frequencies," *IEEE Transactions on Microwave Theory and Techniques*, vol. 51, no. 4, pp. 1062–1066, 2003.
- [35] C. Fumeaux, M. A. Gritz, I. Codreanu, W. L. Schaich, F. J. González, and G. D. Boreman, "Measurement of the resonant lengths of infrared dipole antennas," *Infrared Physics & Technology*, vol. 41, no. 5, pp. 271–281, 2000.
- [36] F. Neubrech, T. Kolb, R. Lovrincic et al., "Resonances of individual metal nanowires in the infrared," *Applied Physics Letters*, vol. 89, Article ID 253104, 2006.
- [37] R. L. Olmon and M. B. Raschke, "Antenna-load interactions at optical frequencies: impedance matching to quantum systems," *Nanotechnology*, vol. 23, no. 44, Article ID 444001, 2012.
- [38] F. Neubrech, D. Weber, R. Lovrincic et al., "Resonances of individual lithographic gold nanowires in the infrared," *Applied Physics Letters*, vol. 93, no. 16, Article ID 163105, 2008.
- [39] L. Yousefi and A. C. Foster, "Waveguide-fed optical hybrid plasmonic patch nano-antenna," *Optics Express*, vol. 20, no. 16, pp. 18326–18335, 2012.

## Research Article

# A Multiple Resonant Frequencies Circular Reconfigurable Antenna Investigated with Wireless Powering in a Concrete Block

Shishir Shanker Punjala,<sup>1</sup> Niki Pissinou,<sup>2</sup> and Kia Makki<sup>3</sup>

<sup>1</sup>Tata Consultancy Services, Deccan Park, Madapur, Hyderabad 500081, India

<sup>2</sup>School of Computing and Information Sciences, Florida International University, Miami, FL 33199, USA

<sup>3</sup>School of Engineering and Technology, Miami Dade College, Wolfson Campus, Miami, FL 33132, USA

Correspondence should be addressed to Shishir Shanker Punjala; shesmesh9@gmail.com

Received 4 January 2015; Revised 17 April 2015; Accepted 29 April 2015

Academic Editor: Luis Landesa

Copyright © 2015 Shishir Shanker Punjala et al. This is an open access article distributed under the Creative Commons Attribution License, which permits unrestricted use, distribution, and reproduction in any medium, provided the original work is properly cited.

A novel broadband reconfigurable antenna design that can cover different frequency bands is presented. This antenna has multiple resonant frequencies. The reflection coefficient graphs for this antenna are presented in this paper. The new proposed design was investigated along with RF MEMS switches and the results are also presented. Investigations were carried out to check the efficiency of the antenna in the wireless powering domain. The antenna was placed in a concrete block and its result comparison to that of a dipole antenna is also presented in this paper.

## 1. Introduction

Reconfigurable antennas [1] are preferred in modern wireless communication systems as they provide a single antenna that can be used for multiple application systems. By using switches, the basic characteristics of a reconfigurable antenna such as the operating frequency, bandwidth, polarization, and the radiation pattern can be tuned to a specific application. These basic characteristics are changed by increasing or decreasing the electrical length of the antenna. A frequency reconfigurable antenna [2] also has low isolation problems.

A novel Circular Reconfigurable Antenna is presented in this paper. Its reflection coefficient, radiation pattern, and gain results are also presented in this paper. The application of this antenna is extended to the wireless powering domain. Investigations were carried out placing the Circular Reconfigurable Antenna and a dipole antenna inside a concrete block. In separate instances, a dipole antenna and another Circular Reconfigurable Antenna were placed above the concrete block and the currents on the surface of the antennas were measured. All results presented in this paper were obtained using HFSS.

## 2. CRA

The Circular Reconfigurable Antenna (CRA) shown in Figure 1 contains a circular patch of radius 18.6 mm at the center. Three concentric circular rings are placed around the circular patch. Each concentric circular ring is connected to the next circular ring through four more switches. The concentric circular rings have a radius of 13 mm at a distance of 1 mm around it. This antenna was placed as shown in Figure 1 on top of a substrate of dimensions 148.8 mm × 148.8 mm and thickness 1.5748 mm.

The design equations [3] of a Circular Patch Antenna are given below:

$$a = \frac{F}{\{1 + (2h/\pi\epsilon_r F) [\ln(\pi F/2h) + 1.7726]\}^{1/2}}, \quad (1)$$

where

$$F = \frac{8.791 \times 10^9}{f_r \sqrt{\epsilon_r}}, \quad (2)$$

$a$  is the radius of the Circular Patch Antenna.

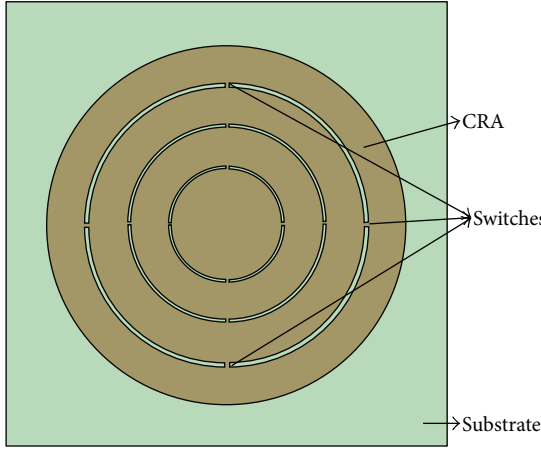


FIGURE 1: The Circular Reconfigurable Antenna (CRA).

The CRA was designed with the idea that if the radius of the antenna could be increased using switches then the resonating frequency of the antenna could also change. The CRA has four iterations. In the first iteration, only the circular patch is radiating and all the switches are open. In the second iteration, the first set of four switches are on. Thus, the first concentric circular ring and the circular patch are radiating. In the third and the fourth iterations, the third and the fourth set of switches are on. Thus, the third and the fourth concentric circular rings are also radiating. Using the above design equations, the central circular patch can be designed for any frequency band (MHz, GHz, or THz) and the concentric rings can be used to vary the frequency of resonance.

### 3. CRA with RF MEMS Switches

In [4], the three-dimensional geometry of shunt capacitive RF MEMS switches was analyzed performing a full wave analysis. The CRA was analyzed in the fourth iteration by using the equivalent lumped circuit [4] model shown in Figure 2 for different geometries. A switch of dimensions [4]  $280\text{ }\mu\text{m} \times 120\text{ }\mu\text{m}$  is used along with the CRA as shown in Figure 3. The equivalent circuit values [4] are inductance of  $5.03\text{ pH}$ , capacitance of  $9.31\text{ pF}$ , and resistance of  $0.034\text{ ohm}$  in the ON state.

### 4. Concrete

The permittivity of a concrete block [1, 5] shown in Figure 4 has been modeled assuming that it is lossy dielectric and that a slab has a real part and an imaginary part. The permittivity of a concrete block shown in Figure 4 can be written as

$$\hat{\epsilon} = \epsilon' - \epsilon'', \quad (3)$$

where  $\epsilon'$  is the real part of complex permittivity of a concrete block and  $\epsilon''$  is the imaginary part of permittivity of a concrete block. By modeling a concrete block as a Debye

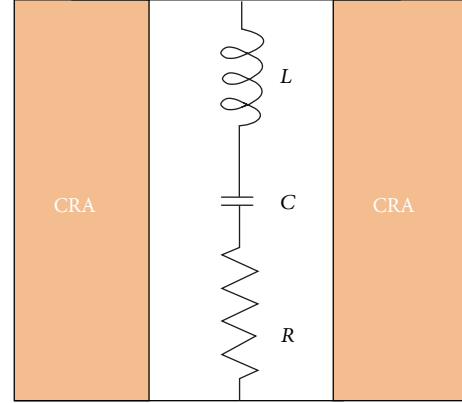


FIGURE 2: Equivalent circuit model of the capacitive RF MEMS switches [7].

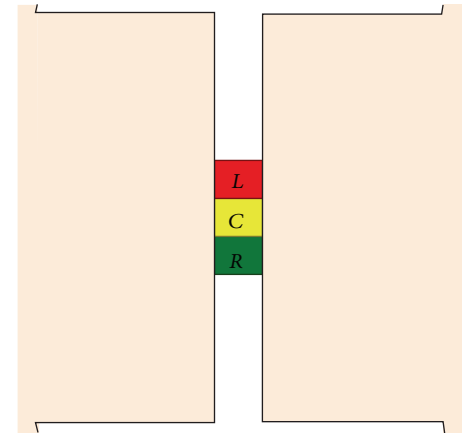


FIGURE 3: RF MEMS switches in the layout of the antenna.

material [1, 5], its frequency dependent complex relative permittivity obeys the following equation:

$$\hat{\epsilon}(\omega) = \epsilon'(\omega) - \epsilon''(\omega). \quad (4)$$

The concrete model used in these investigations contains a moisture content of 12%. A CRA antenna and a dipole were placed inside a concrete block and the surface of the concrete block was excited using another CRA antenna and a dipole antenna.

### 5. Current Consumption of Typical Sensors

A temperature sensor [1, 6] consumes  $300\text{ }\mu\text{A}$  ( $\mu = \text{Micro} = 10^{-6}$ ) for  $50\text{ }\mu\text{Sec}$  for a stable reading every five seconds, and a humidity sensor consumes  $2.8\text{ mA}$  for  $150\text{ msec}$  for a stable reading every thirty seconds. The radio frequency energy incident on the receiving antenna has to be converted to electrical energy [6] to enable wireless powering.

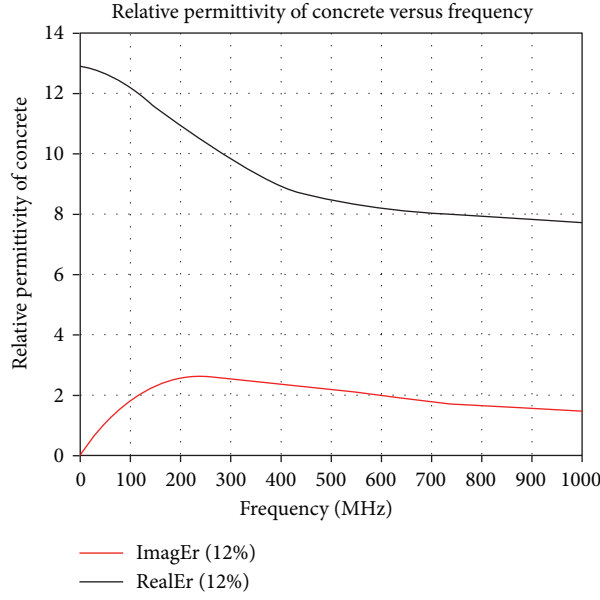
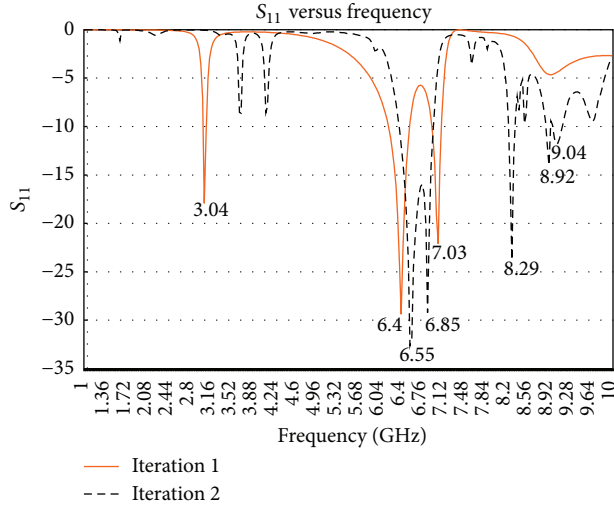
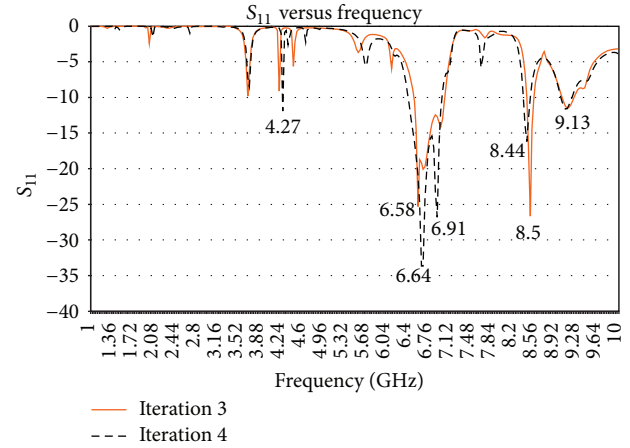


FIGURE 4: Relative permittivity of concrete for 12% moisture content [1, 5].

FIGURE 5:  $S_{11}$  versus frequency (GHz).FIGURE 6:  $S_{11}$  versus frequency (GHz).

## 6. CRA Results

While simulating the CRA, open circuit was used when the switches were off and the patches were shorted when the switches were on. Figures 5 and 6 show the input reflection coefficient  $S_{11}$  for the CRA iterations 1, 2, 3, and 4. The VSWR plots for the CRA iterations 1–4 are shown in Figures 7, 8, 9, and 10. The VSWR values for certain frequencies are very high, so the maximum value of 10 was chosen on the  $y$ -axis. This is the reason the VSWR values which are more than 10 are not visible in Figures 7, 8, 9, and 10. The antenna has a number of resonating frequencies from 3 to 9.5 GHz. The resonating frequency is given at every peak in the input

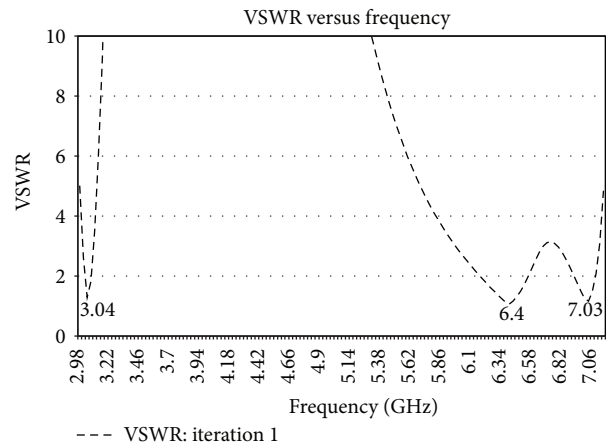


FIGURE 7: VSWR for iteration 1.

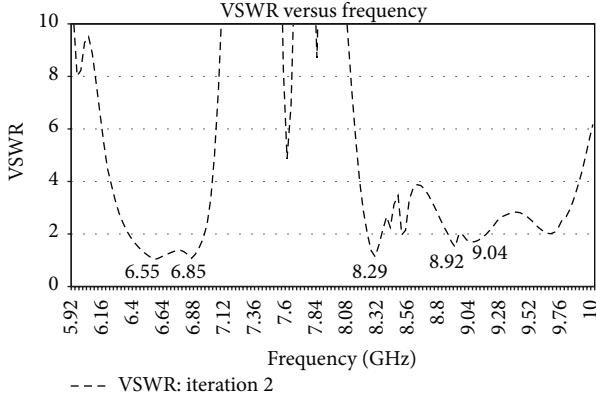


FIGURE 8: VSWR for iteration 2.

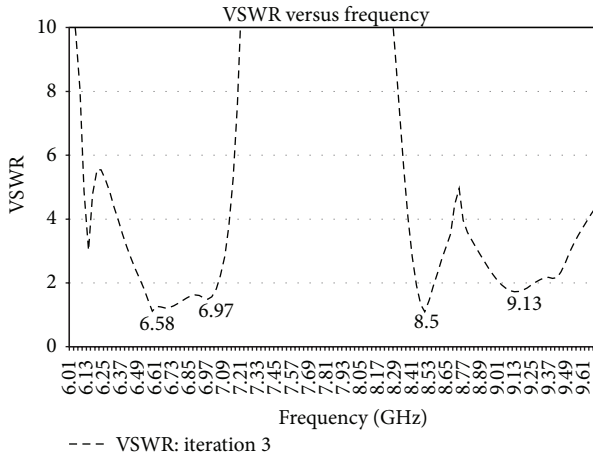


FIGURE 9: VSWR for iteration 3.

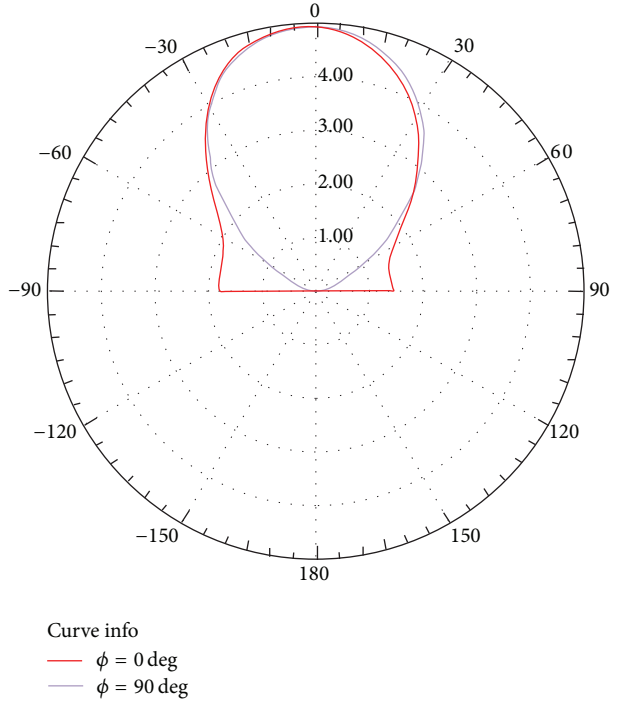


FIGURE 11: Directivity of the CRA for the first iteration at 3.04 GHz.

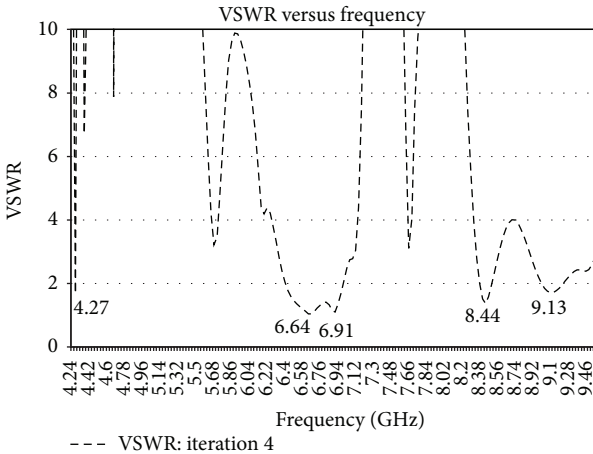


FIGURE 10: VSWR for iteration 4.

reflection coefficient graphs. The VSWR dips below 2 for the corresponding resonating frequency.

As seen in Figures 5, 6, 7, 8, 9, and 10, when an iteration was added to the CRA, the resonating frequencies were

changing. The resonating frequencies for all the iterations are given in Table 1.

The radiation patterns and 3D and 2D gains of the CRA were plotted for 3.04 GHz (iteration 1), 6.55 GHz (iteration 2), 8.5 GHz (iteration 3), and 8.44 GHz (iteration 4) using HFSS and presented in this paper (Figures 11, 12, 13, 14, 15, 16, 17, 18, 19, 20, 21, and 22).

## 7. CRA with RF MEMS Switches Results

The input reflection coefficient  $S_{11}$  for the fourth iteration using RF MEMS switches shown in Figure 3 was plotted. This simulations result shown in Figure 22 was obtained using HFSS and is almost the same as the input reflection coefficient

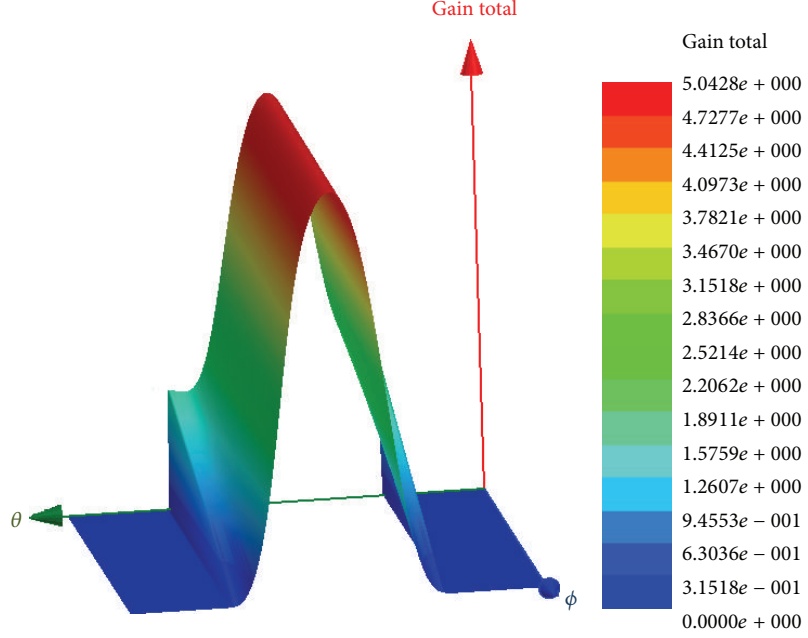


FIGURE 12: 3D gain of the CRA for the first iteration at 3.04 GHz.

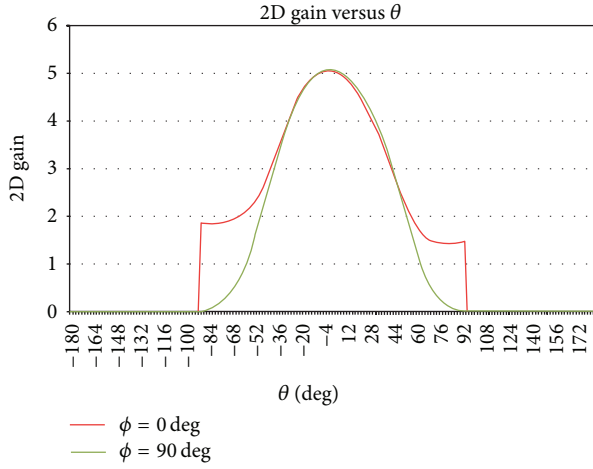


FIGURE 13: 2D gain of the CRA for the first iteration at 3.04 GHz.

TABLE 1: Resonating frequencies of the CRA.

Iteration	Number of resonating frequencies	Resonating frequencies (GHz)
1	3	3.04, 6.4, 7.03
2	4	6.55, 6.85, 8.92, 9.04
3	5	6.58, 6.67, 6.97, 8.5, 9.13
4	4	4.27, 6.64, 6.91, 8.44, 9.13

$S_{11}$  for the CRA in the fourth iteration from 6 to 10 GHz. A resonant frequency of 4.27 GHz is however missing. These results confirm the theory that circuit elements can be used in HFSS to simulate RF MEMS switches [4, 7] in the ON state (Figure 23).

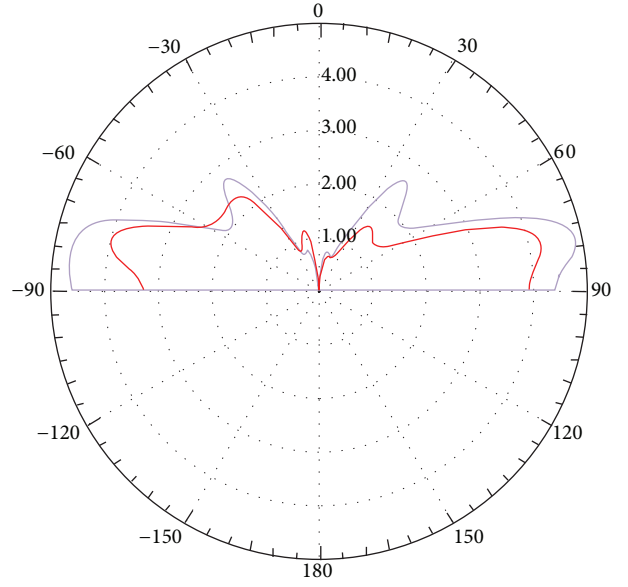


FIGURE 14: Directivity of the CRA for the second iteration at 6.55 GHz.

## 8. Wireless Powering in a Concrete Block

Three cases were chosen as shown in Table 2. A concrete block of 300 mm × 300 mm × 23 mm was chosen. The receiver antenna was placed 20 mm inside the concrete block of 12% humidity. A transmitting antenna was placed 100 mm outside

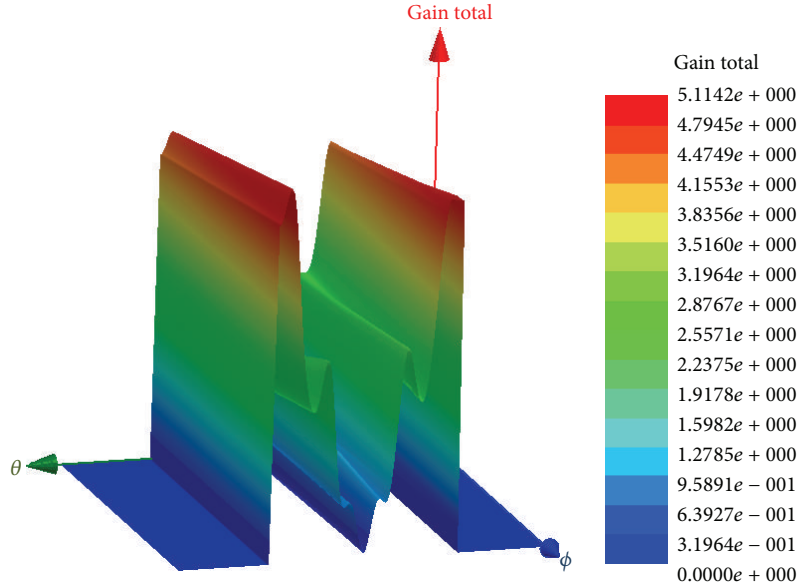


FIGURE 15: 3D gain of the CRA for the second iteration at 6.55 GHz.

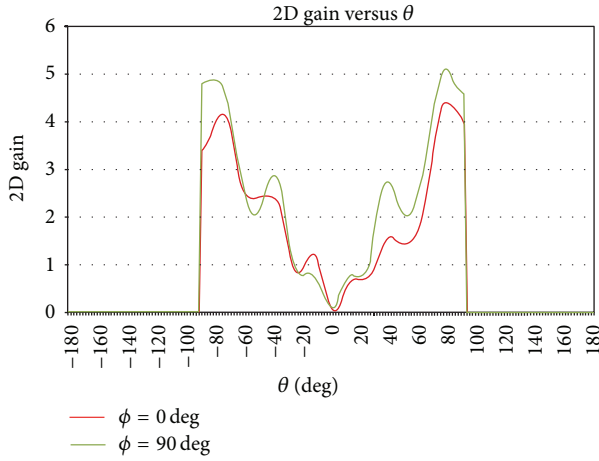


FIGURE 16: 2D gain of the CRA for the second iteration at 6.55 GHz.

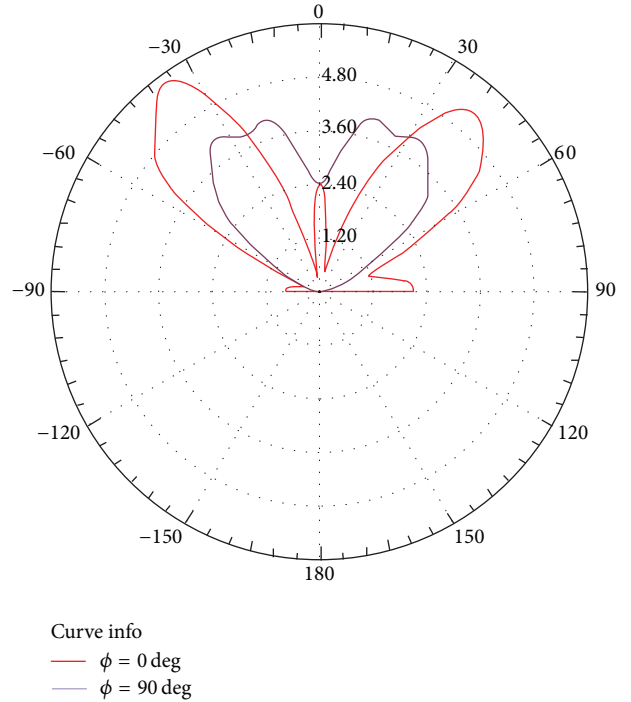


FIGURE 17: Directivity of the CRA for the third iteration at a frequency of 8.5 GHz.

TABLE 2: The three cases.

Case	Frequency (GHz)	Transmitter	Receiver
1	0.5	Dipole	Dipole
2	0.5	Dipole	CRA
3	6.64	CRA	CRA

the concrete block. This arrangement is shown in Figure 24. As stated earlier, the concrete block was simulated in HFSS as a Debye model [1, 5]. The attenuation of the concrete block is very high at high frequencies [8, 9]. The dipole used was designed to resonate at a frequency of 500 MHz and the best resonant frequency of 6.64 GHz (iteration 4) shown in Figure 6 was used for the CRA. An input peak current of 10.75798 A was provided to the transmitter using HFSS. The

currents measured using HFSS on the surface of the receiver antenna are shown in Table 3.

Even though the CRA in Case 3 is being excited by a very high frequency of 6.64 GHz, the received current shown in Table 3 is almost the same as Case 1. The received current was shown to be more than sufficient to power sensors. The use of the CRA antenna is allowing typical wireless sensors

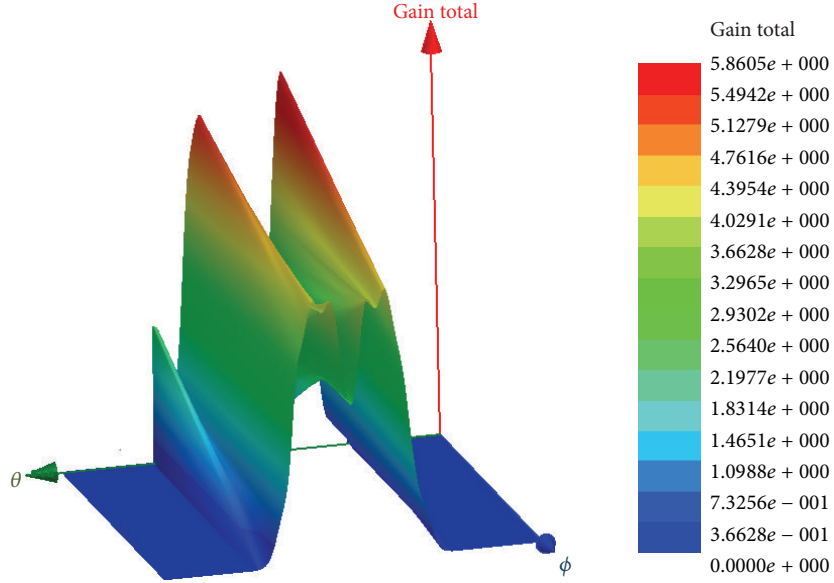


FIGURE 18: 3D gain of the CRA for the third iteration at 8.5 GHz.

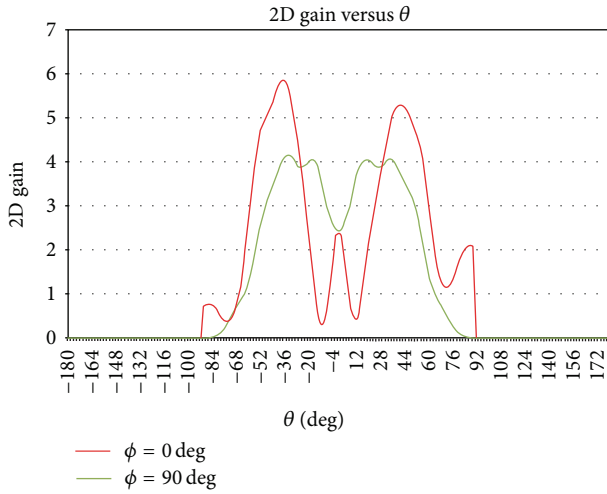


FIGURE 19: 2D gain of the CRA for the third iteration at 8.5 GHz.

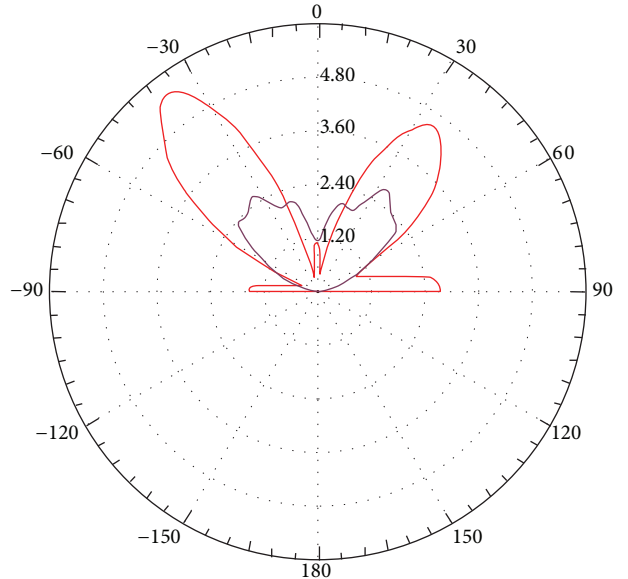


FIGURE 20: Directivity of the CRA for the fourth iteration at 8.44 GHz.

TABLE 3: Received currents.

Case	Input peak current (A)	Received peak current (A)
1	10.75798	0.3756
2	10.75798	0.0238
3	10.75798	0.3176

shown in Section 5 to be powered at high frequencies which in earlier publication results [1, 9] was shown to be very difficult.

## 9. Conclusions

The CRA antenna can be designed for any frequency band. The gain and the radiation pattern of the CRA antenna can be changed by using the switches and changing the iterations.

The input reflection coefficient  $S_{11}$  was shown with RF MEMS switches and the ability of the antenna was verified. The CRA antenna can also be used to power sensors at low as well as high frequencies. The currents received in a concrete slab by the CRA have been presented for the first time in this paper.

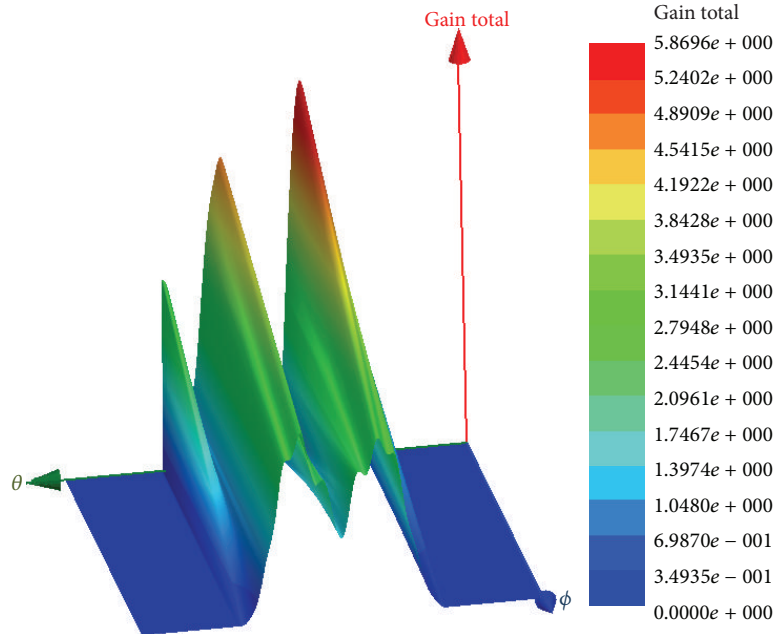


FIGURE 21: 3D gain of the CRA for the fourth iteration at 8.44 GHz.

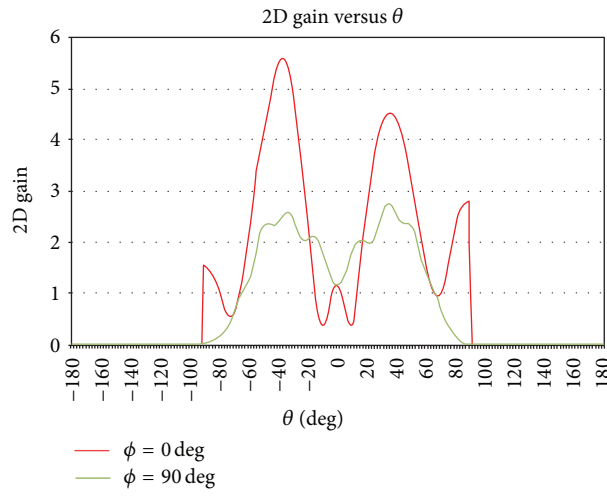


FIGURE 22: 2D gain of the CRA for the fourth iteration at 8.44 GHz.

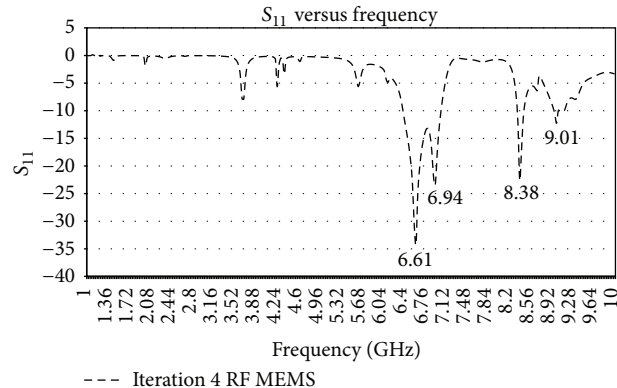


FIGURE 23:  $S_{11}$  (RF MEMS switches) versus frequency (GHz).

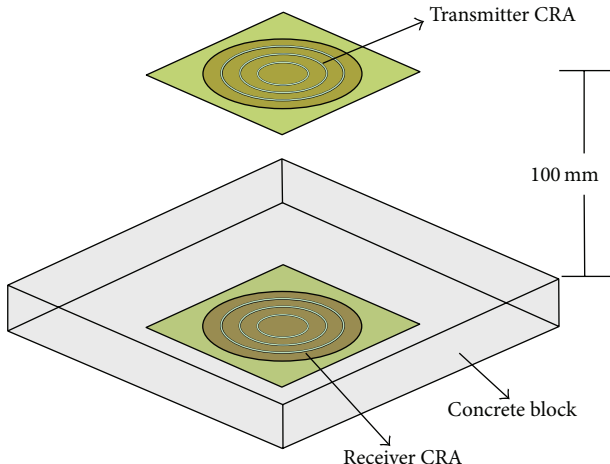


FIGURE 24: Case 3 layout.

## Conflict of Interests

The authors declare that there is no conflict of interests regarding the publication of this paper.

## Acknowledgment

This work was supported by EIS, Tata Consultancy Services, Pune.

## References

- [1] S. S. Punjala, *Effective reconfigurable antenna designs to enhance performance and enable wireless powering* [FIU Electronic Theses and Dissertations], Florida International University, 2009.
- [2] C. Y. Rhee, J. H. Kim, W. J. Jung, T. Park, B. Lee, and C. W. Jung, "Frequency-reconfigurable antenna for broadband airborne applications," *IEEE Antennas and Wireless Propagation Letters*, vol. 13, pp. 189–192, 2014.
- [3] A. Constantine, *Antenna Theory Analysis and Design*, Wiley, 3rd edition, 2005.
- [4] J. Y. Qian, G. P. Li, and F. de Flaviis, "A parametric model of low-noise RF MEMS capacitive switches," in *Proceedings of the Asia-Pacific Microwave Conference (APMC '01)*, vol. 3, pp. 1020–1023, December 2001.
- [5] L. Sandrolini, U. Reggiani, and A. Ogunsola, "Modelling the electrical properties of concrete for shielding effectiveness prediction," *Journal of Physics D: Applied Physics*, vol. 40, no. 17, pp. 5366–5372, 2007.
- [6] S. A. Bhalerao, A. V. Chaudhary, R. B. Deshmukh, and R. M. Patrikar, "Powering wireless sensor nodes using ambient RF energy," in *Proceedings of the IEEE International Conference on Systems, Man and Cybernetics (SMC '06)*, pp. 2695–2700, IEEE, Taipei, Taiwan, October 2006.
- [7] G. H. Huff and J. T. Bernhard, "Integration of packaged RF MEMS switches with radiation pattern reconfigurable square spiral microstrip antennas," *IEEE Transactions on Antennas and Propagation*, vol. 54, no. 2, pp. 464–469, 2006.
- [8] S. S. Punjala and K. Makki, "Wireless powering of sensors in free space and concrete medium," in *Proceedings of the 13th International Symposium on Antenna Technology and Applied Electromagnetics and the Canadian Radio Sciences Meeting (ANTEM/URSI '09)*, pp. 1–4, February 2009.
- [9] S. S. Punjala, "Wireless powering of sensors inside concrete," in *Proceedings of the International Conference on Advanced Technologies for Communications (ATC '08)*, pp. 254–257, October 2008.

## Research Article

# High Gain Superstrate Loaded Membrane Antenna Based on Substrate Integrated Waveguide Technology

**Hamsakutty Vettikalladi**

*Department of Electrical Engineering, King Saud University, P.O. Box 800, Riyadh 11421, Saudi Arabia*

Correspondence should be addressed to Hamsakutty Vettikalladi; hvettikalladi@ksu.edu.sa

Received 10 December 2014; Accepted 16 February 2015

Academic Editor: Chih-Hua Chang

Copyright © 2015 Hamsakutty Vettikalladi. This is an open access article distributed under the Creative Commons Attribution License, which permits unrestricted use, distribution, and reproduction in any medium, provided the original work is properly cited.

The design and the results of a single slot coupled substrate integrated waveguide (SIW) fed membrane antenna loaded with a superstrate layer are presented for 94 GHz communication system. The membrane antenna is designed using ANSYS HFSS and consists of 6 layers. The microstrip patch antenna (MPA) placed on the top pyralux substrate layer is excited by means of a longitudinal rectangular slot placed over the SIW structure in the bottom pyralux substrate. The simulated antenna impedance bandwidth is found to be 5 GHz (91.5–96.5 GHz) with a gain of 7 dBi. In order to improve the gain a superstrate layer is added above the membrane antenna. The maximum gain achieved is 14.4 dBi with an efficiency of 77.6% at 94 GHz. The results are verified using CST Microwave Studio and are found to be in good agreement.

## 1. Introduction

During the last decade significant advances in millimeter wave technologies have been made to cope with the increasing interest. The millimeter-wave (mmW) technology has gained a lot of attention in recent years. The W-band (75–110 GHz) window centered at 94 GHz is in focus due to its unique property of high transmission through atmospheric barriers like smoke, thin dielectrics, and clouds [1] as well as for the development of high resolution imaging applications and ultra broadband wireless communications [2]. Furthermore, the shorter wavelength at mmW permits the production of compact systems for various advance communication systems such as remote sensing, radio astronomy, cloud radar, automotive collision warning, and multi gigabits per second point to point communications.

The general requirements for mmW antennas concerns wide/ultrawide impedance bandwidth, high radiation efficiency, high gains, and compatibility with other RF communications modules. One of the suitable technologies for mmW antennas is substrate integrated circuits (SICs) [3–5]. In principle the SICs are used to synthesize and convert non-planar structures and 3D geometries into planar form which

makes SICs very attractive for millimeter wave applications [6]. Any nonplanar structure can be converted to its equivalent planar structure utilizing SICs technologies such as substrate integrated waveguide (SIW) [2]. The substrate integrated waveguide (SIW) [3–5] is the most matured and popular structure in family of SICs. Several advantages of a rectangular waveguide such as high power handling, high Q-factor, and electrical shielding are attained in SIW technology. Furthermore, the radiation leakage can be ignored in the SIW structures having metallic via placed in close proximity, resulting in propagation characteristics similar to metallic rectangular waveguides [7]. The SIW based structures can be implemented by various manufacturing processes such as conventional printed circuit board process (PCB) [8, 9], multilayer PCB process [10], photoimageable thick film technology [11], and low-temperature cofired ceramic (LTCC) technique. There are many techniques to improve the gain, either by using large arrays [12, 13], which in turn increases losses from the feed network especially at the high frequencies, or by using superstrates [14, 15]. This technique is simple and efficient to improve the gain.

In this paper we present the design and the results of a superstrate loaded multilayer membrane antenna based on

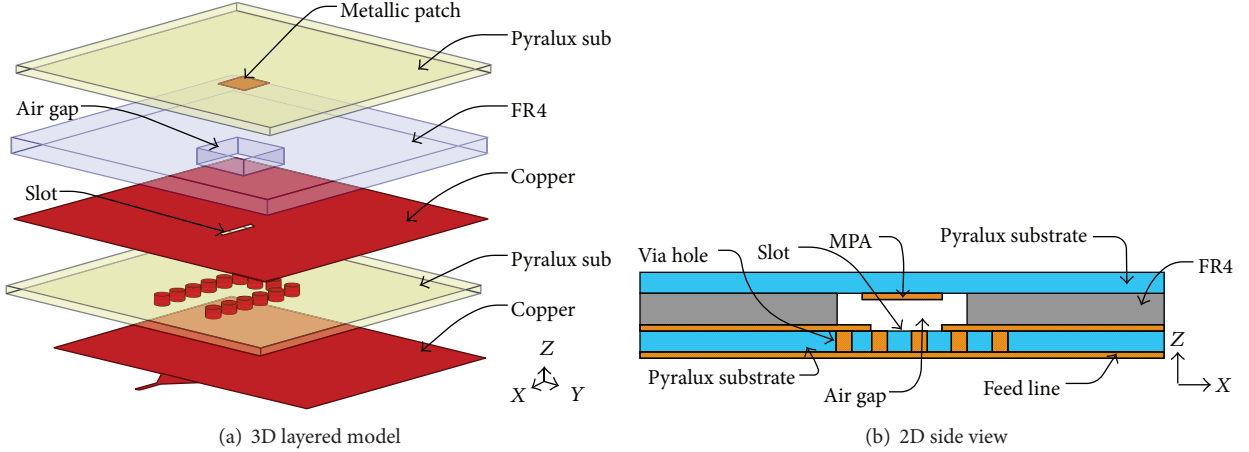


FIGURE 1: Proposed membrane antenna geometry.

SIW technology operating at 94 GHz. The available low cost, low loss DuPont pyralux TK185018R, and FR4 substrates are utilized in the proposed membrane base antenna structure and a high permittivity RT-duroid 6010ML substrate for the superstrate material. The ANSYS HFSS is utilized for modelling and the optimization of proposed antenna, whereas CST Microwave studio is used for validation of the results.

## 2. SIW Fed Base Membrane Antenna

**2.1. Design and Configuration.** The single element SIW based structure of the proposed membrane antenna with 6 layers is shown in Figure 1. The two substrates are utilized in design, that is, pyralux substrate with  $\epsilon_r = 2.4$  and loss tangent ( $\tan \delta$ ) = 0.002 and FR4 substrates with  $\epsilon_r = 4.4$  and loss tangent ( $\tan \delta$ ) = 0.02. The losses are incorporated in simulation. As shown in Figure 1(a) the top layer consists of a microstrip patch antenna (MPA) etched below the pyralux substrate. The second layer consists of the FR-4 substrate with an air cavity to support the top substrate layer. An air gap is drilled on the second layer to enhance the bandwidth of the antenna. We used the FR4 substrate because it is very cheap, low in loss, and compatible with mass production PCB technology electronics. The bottom three layers makes up a SIW slot antenna, where rectangular slot [16] in the top metallic layer of SIW is utilized to excite the MPA through the air gap made within the FR4 layer. The metallic via holes are made with in the bottom layer of pyralux substrate to form the SIW structure. The proposed membrane antenna structure in XZ plane is shown in Figure 1(b) for a better understanding of various layers. All copper layers used in proposed antenna structure have thickness of  $18\ \mu\text{m}$ , while the thickness of pyralux and FR-4 is taken to be  $50\ \mu\text{m}$  and  $100\ \mu\text{m}$ , respectively.

The distance between two rows of metallic via holes along with the dielectric between them determines the cutoff frequency. The SIW design generally works in  $\text{TE}_{n0}$  mode and does not support propagation of TM modes. For the dielectric filled waveguide (DFW) with same cutoff frequency, the

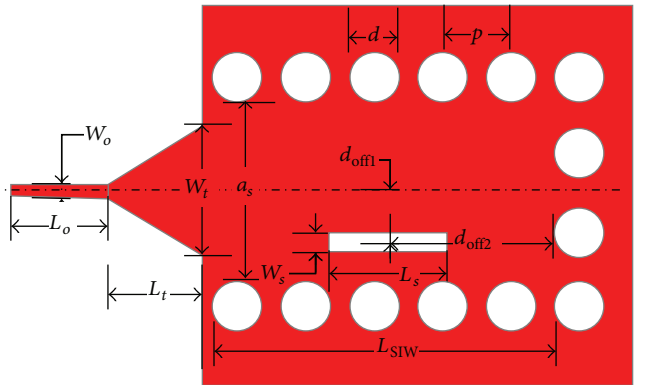


FIGURE 2: Top view of SIW antenna along with rectangular slot.

broad side dimension of waveguide, that is,  $a_d$ , is found by [17]

$$a_d = \frac{a}{\sqrt{\varepsilon_r}}, \quad (1)$$

where  $\epsilon_r$  is the dielectric constant of substrate and dimensions of “ $a$ ” are taken from the standard WR-10 waveguide (i.e., 2.54 mm). Once the dimension  $a_d$  for DFW is known, we can use the following equation to find the separation distance, that is,  $a_s$ , between the via rows of SIW [18]:

$$a_s = a_d + \frac{d^2}{0.95 p}, \quad (2)$$

where  $d$  is the diameter of metallic via holes connecting the upper and lower metallic layers of the bottom pyralux substrate. The via diameter ( $d$ ) is taken by  $d = \lambda_g/5$  and pitch, that is, centre to centre distance between the via holes, is taken by  $p < 2d$  [19].

In Figure 2 the top view of proposed membrane antenna along with longitudinal slot placed on the top ground plane of SIW structure is shown. Usually the distance from the short circuited end of SIW to the centre of slot, that is,  $d_{off2}$ , is

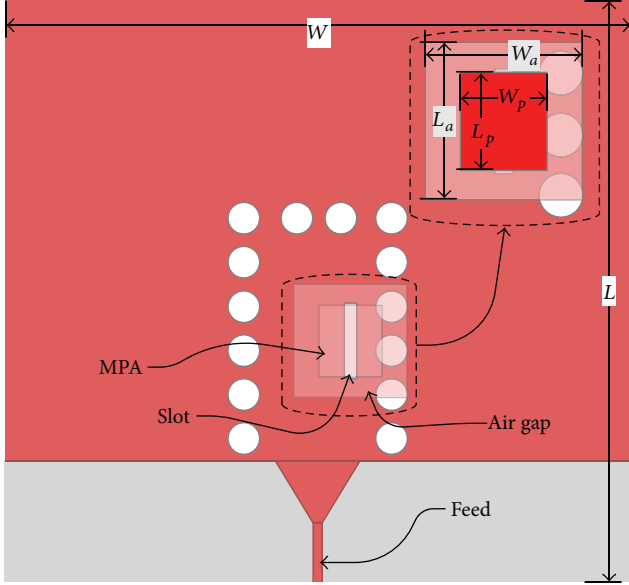


FIGURE 3: Top view of proposed membrane antenna geometry.

a quarter or odd multiple of quarter of the guided wavelength. Initially, this distance is chosen to be three quarter of the guided. Furthermore, the slot offset, that is,  $d_{\text{off}1}$ , is optimized for proper excitation of longitudinal slot as well as the metallic patch antenna on the top layer. The initial dimension for longitudinal slot length is taken by [17]

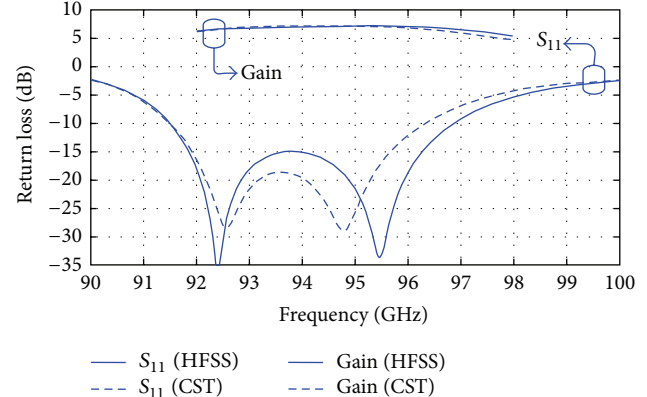
$$L_s = \frac{\lambda_o}{\sqrt{2(\epsilon_r + 1)}}. \quad (3)$$

The pyralux substrate with patch on top layer is supported by a layer of FR4 substrate having an optimized air gap of  $1.8 \text{ mm} \times 1.8 \text{ mm}$  under the MPA. The optimized dimensions for MPA are found to be  $1.12 \times 0.99 \text{ mm}$ . The total size of antenna is found to be  $10 \text{ mm} \times 10 \text{ mm}$ . A conventional  $50 \Omega$  microstrip line is utilized as a feed element in the proposed antenna. The microstrip to SIW transition consisting of a tapered microstrip is also optimized for proper impedance matching. The detailed view of proposed single membrane antenna along with various important design parameters for MPA and air gap in FR-4 substrate are well explained in [20] and in Figure 3.

The optimum dimension for the proposed membrane antenna structure is  $W_o = 0.145 \text{ mm}$ ,  $W_t = 1.34 \text{ mm}$ ,  $L_o = 1 \text{ mm}$ ,  $L_t = 0.9 \text{ mm}$ ,  $d = 0.5 \text{ mm}$ ,  $p = 0.7 \text{ mm}$ ,  $a_s = 1.5 \text{ mm}$ ,  $W_s = 0.2 \text{ mm}$ ,  $L_s = 1.225 \text{ mm}$ ,  $L = 3.5 \text{ mm}$ ,  $d_{\text{off}1} = 0.55 \text{ mm}$ ,  $d_{\text{off}2} = 1.4125 \text{ mm}$ ,  $L_a = 1.85 \text{ mm}$ ,  $W_a = 1.85 \text{ mm}$ ,  $L_p = 1.15 \text{ mm}$ ,  $W_p = 1.05 \text{ mm}$ ,  $L = 10 \text{ mm}$ , and  $W = 10 \text{ mm}$ .

**2.2. Results and Discussion.** The proposed antenna structure is simulated and optimized using ANSYS High Frequency Structure Simulator (HFSS<sup>®</sup>). The results are further verified by simulating the proposed antenna structure in CST Microwave Studio.

A comparison between the simulation results of  $S_{11}$  and gain obtained from HFSS and CST are given in Figure 4.

FIGURE 4: Simulated return loss  $S_{11}$  and realized gain.

The two resonances at 92.4 GHz and 95.5 GHz are due to presence of slot and patch in antenna geometry, respectively, which are kept in close proximity to achieve wide impedance bandwidth. The FR-4 support with air gap plays an important role in merging the two resonances to achieve a wide impedance bandwidth. The antenna impedance bandwidth is found to be 5.4 GHz (91.5–96.9 GHz) from HFSS while from CST the impedance bandwidth is found to be approximately 4.9 GHz (91.5–96.4 GHz). The gain is found to be 7 dBi at the center frequency of 94 GHz. The peak gain of 7.5 dB is found at 95.5 GHz. Furthermore, the antenna gain remains above 6.7 dB in whole frequency band of operation.

The antenna radiation pattern in both E-plane (horizontal plane) and H-plane (vertical plane) remains similar throughout the whole frequency band of operation. The comparison of 2D radiation patterns obtained from HFSS and CST at 92, 94, and 96 GHz in both vertical plane ( $\varphi = 90^\circ$ ) and horizontal plane ( $\varphi = 0^\circ$ ) plane is shown in Figures 5 and 6, respectively. By increasing the ground plane size the small ripples in E-plane radiation pattern can be reduced, which are mainly due to diffraction of the limited ground plane. The cross polarization ratio of less than  $-20 \text{ dB}$  is achieved in E- and H-plane radiation patterns, respectively. The antenna 3 dB beam width is found to be  $50^\circ$  and  $45^\circ$  in E- and H-plane, respectively.

From the above results, it is noted that the peak gain obtained is only 7.5 dBi which is not enough for the point to point communication at 94 GHz. So we added a superstrate layer to improve the gain.

### 3. Improvement of Gain with Superstrate Layer

Side view of proposed antenna with superstrate layer is shown in Figure 7. It consists of the base antenna as explained in Section 2 and a dielectric superstrate layer is added above it. The material used for the superstrate is Roger RT-duroid 6010ML ( $\epsilon_r = 10.2$ , and  $\tan(\delta) = 0.003$ ). A Rohacell foam layer of permittivity 1.05 is sandwiched between base antenna and superstrate as a support. The thickness  $t$ , dimension  $S$ ,

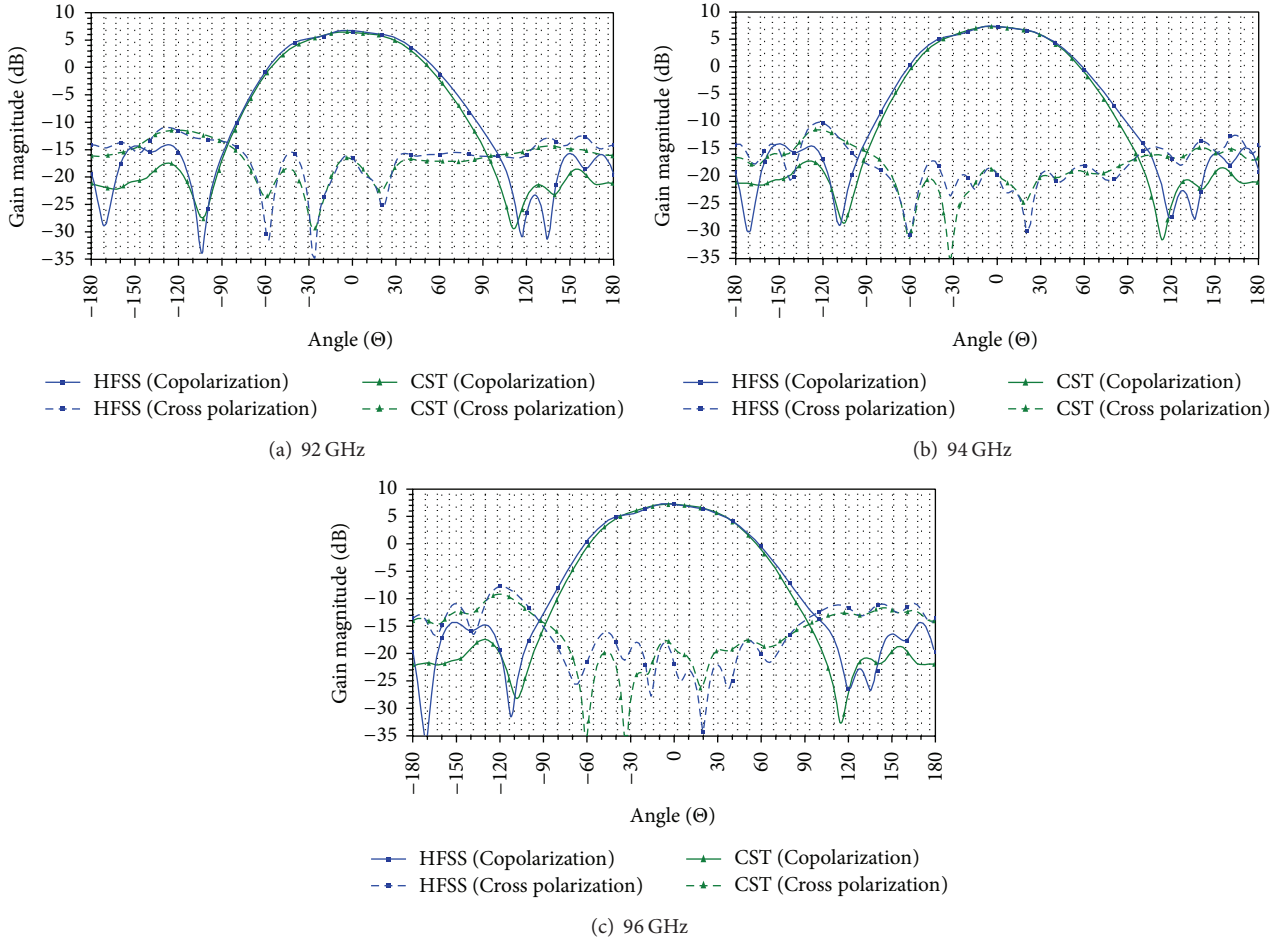


FIGURE 5: 2D radiation pattern in H-plane with co- and cross polarization.

and the height of the superstrate  $h$  are studied and optimised as explained below.

The variation of  $S_{11}$  and gain with different superstrate thickness ( $t = 0.127, 0.254$ , and  $0.635$  mm) with a constant height of  $h = 0.55\lambda_0$  and size  $S = 3.125 \times 3.125\lambda_0 = 10 \times 10$  mm $^2$  is shown in Figure 8. It is noted that even though the maximum gain is achieved for a superstrate thickness of  $t = 0.635$  as compared to  $t = 0.127\lambda_0$ , the side lobe level (SLL) is worst as investigated in Figure 9. This poor SLL with large thickness of the material may be due to the surface waves at this high frequency. Hence we took the commercially available thickness  $t = 0.127$  mm as the superstrate material. The side lobe levels in this case are less than  $-15$  dB in the whole frequency band of interest.

Figure 10 shows the variation of return loss ( $S_{11}$ ) and gain for different superstrate heights,  $h = 0.5\lambda_0, 0.55\lambda_0, 0.6\lambda_0$ , respectively, with a superstrate size of  $S = 3.125 \times 3.125\lambda_0$ . It is clear from the figure that the maximum gain with worst bandwidth is achieved for a superstrate height of  $h = 0.55\lambda_0$ , while for the good desired bandwidth of 92 GHz–96 GHz is achieved with a height of  $h = 0.6\lambda_0$  and is the best one. The high gain at  $h = 0.55\lambda_0$  is because of the narrow bandwidth. We took the height  $h = 0.6\lambda_0$  for the next optimisation simulation.

The variation of the superstrate size  $S$  for an optimised height of  $h = 0.6\lambda_0$  is studied as shown in Figure 11. It is clear that the maximum gain of 14.4 dBi with good bandwidth of 92 GHz–96 GHz is achieved for a superstrate size of  $S = 2\lambda_0 \times 2\lambda_0$ .

The comparison of CST and HFSS results of return loss ( $S_{11}$ ), gain, and directivity of the optimised dimension is given in Figure 12. The 2:1 VSWR bandwidth is noted to be 92 GHz–96 GHz (i.e., 4.25% impedance bandwidth) with a maximum gain of 14.4 dBi and a directivity of 15.5 dBi at 94 GHz, hence a radiation efficiency of 77.6%. The results are in a good agreement between the CST and HFSS simulations. There is a gain enhancement of 7.2 dBi with the loaded superstrate layer as compared to without superstrate.

The E-plane and H-plane radiation characteristics by using CST and HFSS simulations are shown in Figures 13(a) and 13(b), respectively. The simulated results for the frequencies at 92 GHz, 94 GHz, and 96 GHz, respectively, are presented. Both simulation results are in good agreement. E-plane has the side lobe of level  $-14.8$  dB and 3 dB beam width of  $27.9^\circ$  at 94 GHz. The H-plane has the side lobe of level  $-22.1$  dB and 3 dB beam width of  $25.1^\circ$  at the same frequency. There is a cross polar level of less than  $-25$  dB at all frequencies in both planes.

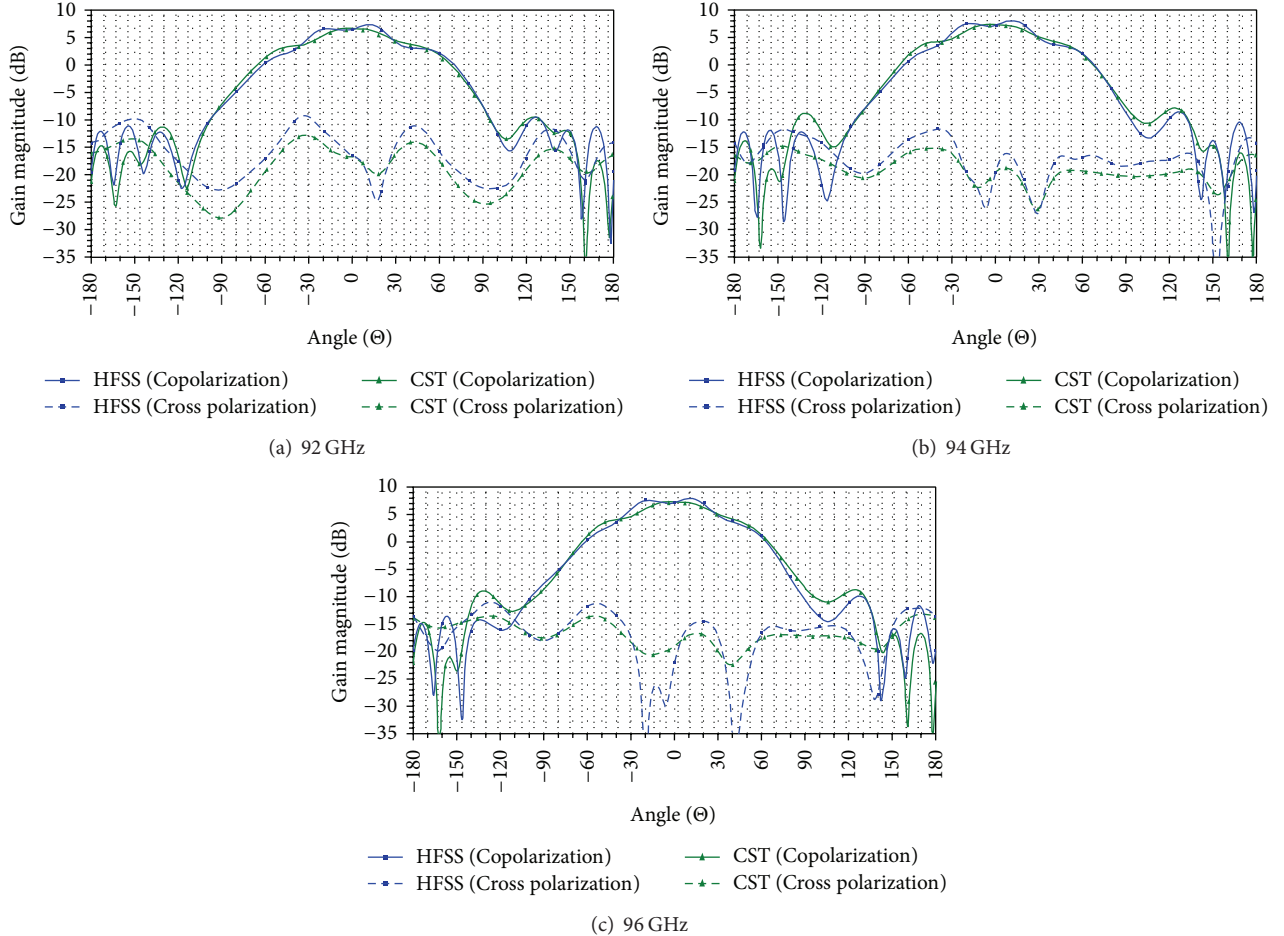


FIGURE 6: 2D radiation pattern in E-plane with co- and cross polarization.

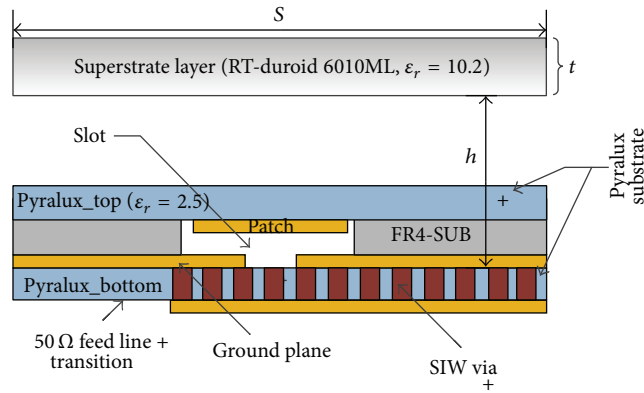


FIGURE 7: Cutting plane of a membrane antenna with superstrate layer, ground plane size  $10 \times 10 \text{ mm}^2$ .

#### **4. Conclusion**

The design and the results of a superstrate loaded membrane antenna based on SIW technology are presented. A microstrip patch antenna along with a longitudinal slot is utilized to achieve a wide impedance bandwidth of 5 GHz at centre frequency of 94 GHz. The gain of the antenna for

the single element is found to be above 6.5 dB in whole frequency band of operation and is further improved to a maximum of 14.4 dBi with an addition of superstrate layer. Furthermore, similar antenna radiation patterns are achieved in whole frequency band of operation. The proposed antenna finds applications in 94 GHz point-point communication systems.

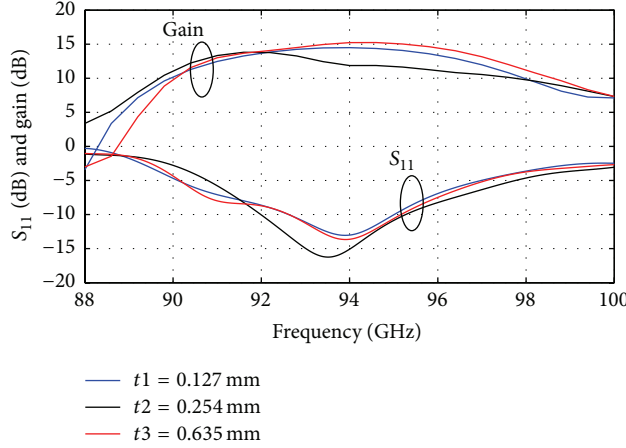


FIGURE 8: Simulated results of  $S_{11}$  and gain with various superstrate thickness for a fixed height  $h = 0.55\lambda_0$ , and size of the superstrate  $S = 3.125 \times 3.125\lambda_0$ .

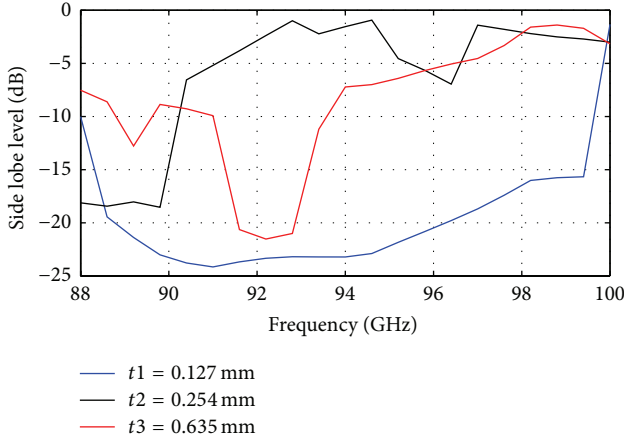


FIGURE 9: The variation of side lobe level of the antenna with the variation of the thickness of the superstrate.

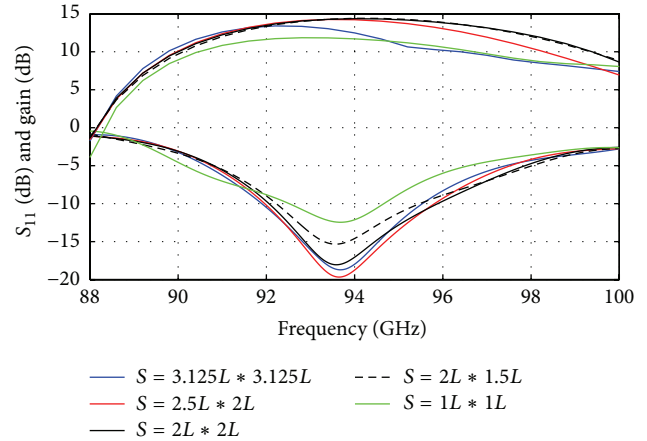


FIGURE 11: Variation of  $S_{11}$  and gain for different dimensions size  $S$  with a fixed superstrate height of  $h = 0.6\lambda_0$ .

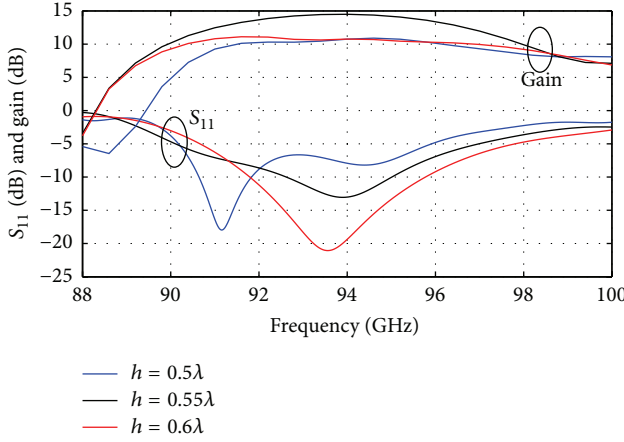


FIGURE 10: Variation of  $S_{11}$  and gain with a superstrate dimension of  $= 3.125 \times 3.125\lambda_0$ , and with different heights of  $h = 0.5\lambda_0$ ,  $h = 0.55\lambda_0$ , and  $h = 0.6\lambda_0$ .

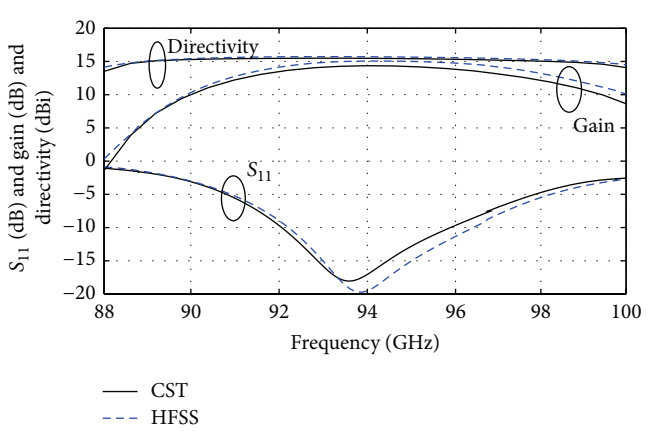


FIGURE 12: Results of  $S_{11}$ , gain, and directivity over frequency with an optimised superstrate dimension  $S = 2 \times 2\lambda_0$ , an optimised height  $h = 0.6\lambda_0$ , and an optimised thickness  $t = 0.127$  mm.

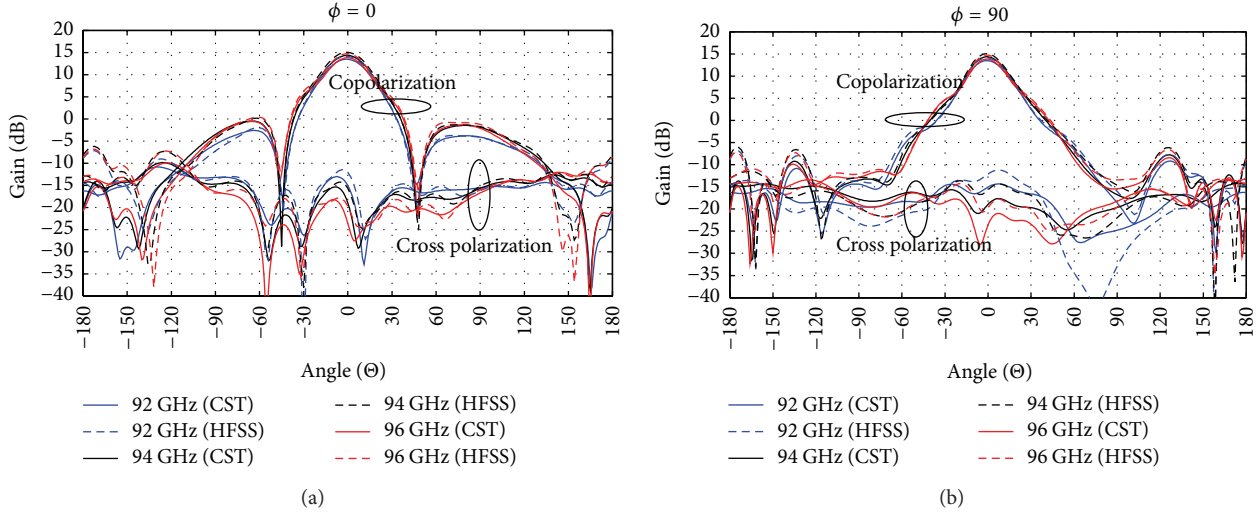


FIGURE 13: Simulated (a) E-plane and (b) H-plane radiation characteristics of superstrate antenna for an optimised superstrate dimension  $S = 2\lambda_0 \times 2\lambda_0$ , height  $h = 0.6\lambda_0$ , and thickness  $t = 0.127$  mm.

## Conflict of Interests

The author declares that there is no conflict of interests regarding the publication of this paper.

## Acknowledgment

The author would like to thank the Deanship of Scientific Research, Research Center at College of Engineering, King Saud University, for funding this research work.

## References

- [1] E. S. Roseblum, "Atmosphere absorption of 10-400 KMQS radiation: summary and biography up to 1961," *Microwave Journal*, vol. 4, pp. 91–96, 1961.
- [2] K. Wu, Y. J. Cheng, T. Djerafi, and W. Hong, "Substrate-integrated millimeter-wave and terahertz antenna technology," *Proceedings of the IEEE*, vol. 100, no. 7, pp. 2219–2232, 2012.
- [3] J. Hirokawa and M. Ando, "Single-layer feed waveguide consisting of posts for plane tem wave excitation in parallel plates," *IEEE Transactions on Antennas and Propagation*, vol. 46, no. 5, pp. 625–630, 1998.
- [4] D. Deslandes and K. Wu, "Single-substrate integration technique of planar circuits and waveguide filters," *IEEE Transactions on Microwave Theory and Techniques*, vol. 51, no. 2, pp. 593–596, 2003.
- [5] D. Deslandes and K. Wu, "Accurate modeling, wave mechanisms, and design considerations of a substrate integrated wave-guide," *IEEE Transactions on Microwave Theory and Techniques*, vol. 54, no. 6, pp. 2516–2526, 2006.
- [6] K. Wu, D. Deslandes, and Y. Cassivi, "The substrate integrated circuits—a new concept for high frequency electronics and optoelectronics," in *Proceedings of the 6th International Conference on Telecommunications in Modern Satellite, Cable and Broadcasting Service (TELSIKS '03)*, vol. 1, pp. 3–5, October 2003.
- [7] M. Bozzi, A. Georgiadis, and K. Wu, "Review of substrate-integrated waveguide circuits and antennas," *IET Microwaves, Antennas and Propagation*, vol. 5, no. 8, pp. 909–920, 2011.
- [8] L. Yan, W. Hong, G. Hua, J. Chen, K. Wu, and T. J. Cui, "Simulation and experiment on SIW slot array antennas," *IEEE Microwave and Wireless Components Letters*, vol. 14, no. 9, pp. 446–448, 2004.
- [9] W. Hong, B. Liu, G. Q. Luo et al., "Integrated microwave and millimeter wave antennas based on SIW and HMSIW technology," in *Proceedings of the IEEE International Workshop on Antenna Technology: Small and Smart Antennas Metamaterials and Applications (iWAT '07)*, pp. 69–72, March 2007.
- [10] H. Nakano, R. Suga, Y. Hirachi, J. Hirokawa, and M. Ando, "60 GHz post-wall waveguide aperture antenna with directors made by multilayer PCB process," in *Proceedings of the 5th European Conference on Antennas and Propagation (EUCAP '11)*, pp. 3113–3116, Rome, Italy, April 2011.
- [11] D. Stephens, P. R. Young, and I. D. Robertson, "W-band substrate integrated waveguide slot antenna," *Electronics Letters*, vol. 41, no. 4, pp. 165–167, 2005.
- [12] S.-S. Oh, J. Heo, D.-H. Kim, J.-W. Lee, M.-S. Song, and Y.-S. Kim, "Broadband millimeter-wave planar antenna array with a waveguide and microstrip-feed network," *Microwave and Optical Technology Letters*, vol. 42, no. 4, pp. 283–287, 2004.
- [13] J. Navarro, "Wide-band, low-profile millimeter-wave antenna array," *Microwave and Optical Technology Letters*, vol. 34, no. 4, pp. 253–255, 2002.
- [14] S. M. Meriah, E. Cambiaggio, R. Staraj, and F. T. Bendimerad, "Gain enhancement for microstrip reflectarray using superstrate layer," *Microwave and Optical Technology Letters*, vol. 46, no. 2, pp. 152–154, 2005.
- [15] H. Vettikalladi, O. Lafond, and M. Himdi, "High-efficient and high-gain superstrate antenna for 60-GHz indoor communication," *IEEE Antennas and Wireless Propagation Letters*, vol. 8, pp. 1422–1425, 2009.
- [16] W. M. Abdel-Wahab and S. Safavi-Naeini, "Wide-bandwidth 60-GHz aperture-coupled microstrip patch antennas (MPAs) fed by substrate integrated waveguide (SIW)," *IEEE Antennas and Wireless Propagation Letters*, vol. 10, pp. 1003–1005, 2011.

- [17] S. Moitra, A. Kumar Mukhopadhyay, and A. Kumar Bhattacharjee, "Ku-Band substrate integrated waveguide (SIW) slot array antenna for next generation networks," *Global Journal of Computer Science and Technology Network, Web & Security*, vol. 13, no. 5, 2013.
- [18] Y. Cassivi, L. Perregrini, P. Arcioni, M. Bressan, K. Wu, and G. Conciauro, "Dispersion characteristics of substrate integrated rectangular waveguide," *IEEE Microwave and Wireless Components Letters*, vol. 12, no. 9, pp. 333–335, 2002.
- [19] K. Wu, D. Deslandes, and Y. Cassivi, "The substrate integrated circuits—a new concept for high-frequency electronics and optoelectronics," in *Proceedings of the 6th International Conference on Telecommunications in Modern Satellites, Cable and Broadcasting Services (TELSIKS '03)*, Niš, Serbia, October 2003.
- [20] H. Vettikalladi, M. K. Saleem, and M. A. S. Alkanhal, "Millimeter wave antenna based on substrate integrated waveguide for 94 GHz communication systems," in *Proceedings of the International Workshop on Antenna Technology (iWAT '14)*, Sydney, Australia, March 2014.

## Research Article

# A Miniaturized Triple Band Monopole Antenna for WLAN and WiMAX Applications

**Yingsong Li<sup>1</sup> and Wenhua Yu<sup>2</sup>**

<sup>1</sup>*College of Information and Communications Engineering, Harbin Engineering University, Harbin 150001, China*

<sup>2</sup>*2COMU, Inc., 4031 University Drive, Suite 100, Fairfax, VA 22030, USA*

Correspondence should be addressed to Yingsong Li; liyingsong@ieee.org

Received 4 February 2015; Accepted 15 April 2015

Academic Editor: Atsushi Mase

Copyright © 2015 Y. Li and W. Yu. This is an open access article distributed under the Creative Commons Attribution License, which permits unrestricted use, distribution, and reproduction in any medium, provided the original work is properly cited.

A miniaturized triple band monopole antenna with a small size is proposed and its performance is investigated both numerically and experimentally for worldwide interoperability for microwave access (WiMAX) and wireless local area network (WLAN) applications. The three resonance frequencies are realized by using a toothbrush-shaped patch (TSP), a meander line (ML), and an inverted U-shaped patch (IUSP). The center frequencies of the triple bands can be controlled by adjusting the dimensions of the TSP, ML, and IUSP. Simulated and measured results are presented to demonstrate that the proposed triband monopole antenna with a good impedance bandwidth and omnidirectional radiation patterns is well suitable for WLAN and WiMAX communication applications.

## 1. Introduction

With the development of the wireless techniques, the demand for low profile, light weight, ease of implementation, and low cost broadband antennas is attractive for short distance communication devices [1, 2]. Worldwide interoperability for microwave access (WiMAX) and wireless local area network (WLAN) are very popular wireless communication systems and have been widely studied and applied in mobile devices in recent years [1–4]. To improve the performance and make the antenna functional in a complicated and diverse WLAN and WiMAX environment, the antennas should cover multiple frequency bands and can provide stable omnidirectional radiation patterns and gains to render it suitable for WLAN (2.4–2.484, 5.15–5.35, and 5.725–5.825 GHz) and WiMAX (3.3–3.69 and 5.25–5.85 GHz) communication systems. Moreover, WLAN and WiMAX may be used simultaneously in the same system. Thus, it is necessary to design a single antenna to cover multiple bands. Several planar printed monopole antennas using slot structures and toothbrush patch have been proposed and well designed to achieve a wide-band property or a dual-band function for meeting wide-band communication applications [5–8]. However, some of these

antennas cannot meet the ever-increasing multiple band communication requirements. In order to serve more communication systems, several multiband monopole antennas with meander lines have been presented in [9–12]. However, some of these reported multiband antennas cannot be integrated into portable devices as an internal antenna owing to their large sizes or complex structures. In addition, microstrip fed monopole antennas have been widely studied and applied to modern portable terminals owing to their simple structures and ease of fabrication and debugging [10, 13]. However, most of these monopole antennas are large in size.

In this paper, we propose a compact triband monopole antenna for WLAN and WiMAX operations. By using a toothbrush-shaped patch (TSP), a meander line (ML), and an inverted U-shaped patch (IUSP), three resonance frequencies can be obtained to operate at 2.4/3.5/5.2/5.5/5.8 GHz bands. The parameter effects on the impedance bandwidth are investigated by using the HFSS. Simulated and measured results show that the proposed antenna possesses controllable triband characteristics and good omnidirectional radiation patterns which make it suitable for WLAN and WiMAX communication applications.

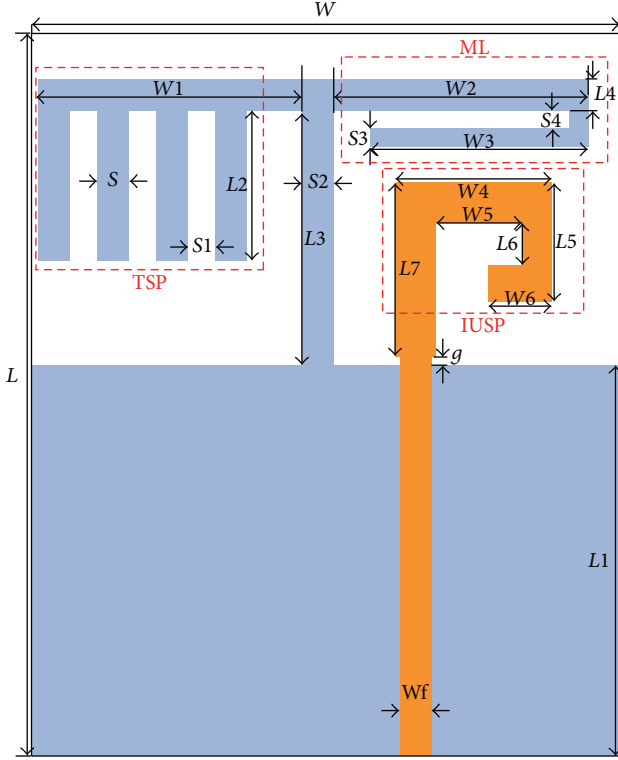
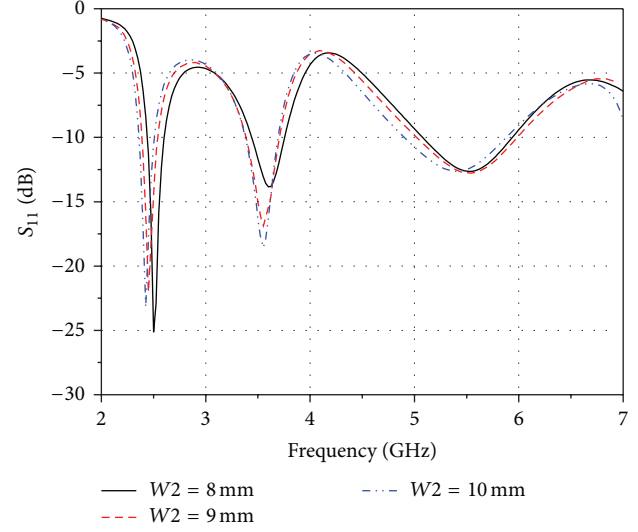


FIGURE 1: Configuration of the proposed triband antenna.

## 2. Antenna Design

Figure 1 depicts the proposed triband monopole antenna, which is fabricated on a FR4 substrate with a relative permittivity of 4.4, a loss tangent of 0.002, and a thickness of 0.8 mm. The proposed antenna consists of a TSP, a ML, and an IUSP. The 50-Ohm microstrip-fed structure is comprised of a feed signal strip line with a width of  $W_f = 1.4$  mm and a partial ground plane. In this design, the TSP and ML are connected with the partial ground plane and are printed at the bottom of the FR4 substrate, while the IUSP is connected with microstrip feed signal strip line and is deigned on top of the FR4 substrate. The ML is used to generate a resonance frequency at 2.4 GHz for lower WLAN band communication application. The TSP is designed to produce a resonance frequency at 3.5 GHz to meet the WiMAX communication requirements, while the higher WLAN bands are obtained by using the IUSP, which aims to give a resonance at 5.5 GHz to cover a wide bandwidth of 5.15–5.825 GHz. The center resonance frequencies are tunable by adjusting the dimensions of the TSP, ML, and IUSP to make them suitable for WLAN and WiMAX communication applications. The proposed antenna has been investigated and optimized by the HFSS. The optimized parameters of the antenna are listed as follows:  $L = 30$  mm,  $W = 20$  mm,  $L_1 = 20$  mm,  $L_2 = 4.2$  mm,  $L_3 = 6.85$  mm,  $L_4 = 1$  mm,  $L_5 = 4.3$  mm,  $L_6 = 1.6$  mm,  $L_7 = 5.1$  mm,  $W_1 = 8.5$  mm,  $W_2 = 9$  mm,  $W_3 = 6.8$  mm,  $W_4 = 5$  mm,  $W_5 = 2.35$  mm,  $W_6 = 1.8$  mm,  $S = 1$  mm,

FIGURE 2: Effects of the parameter  $W_2$  on the return loss.

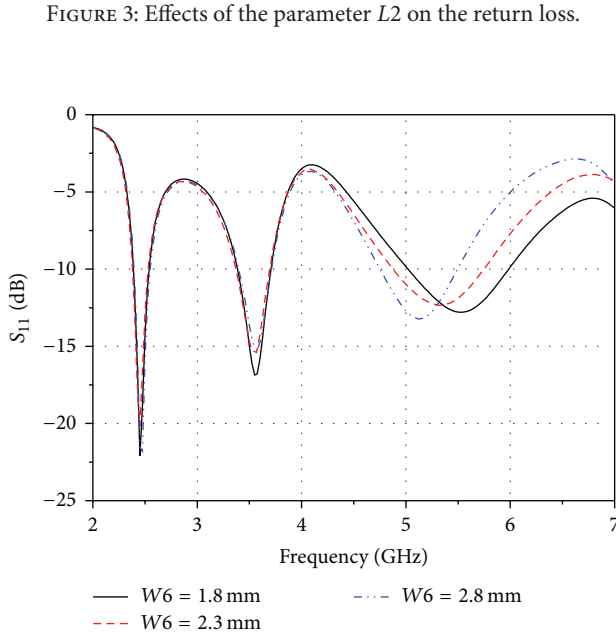
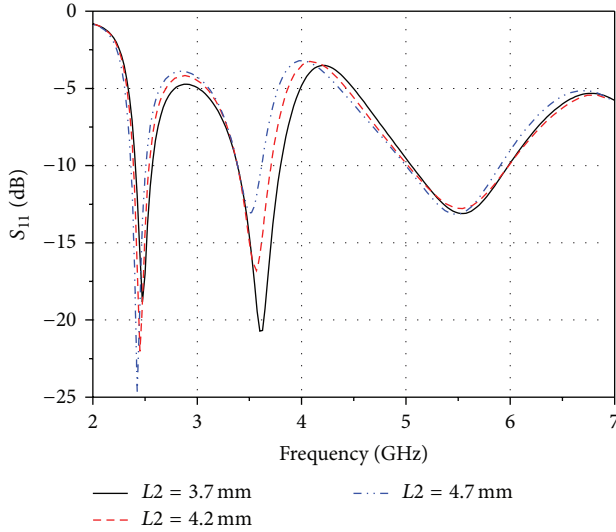
$S_1 = 1$  mm,  $S_2 = 1$  mm,  $S_3 = 0.65$  mm,  $S_4 = 0.4$  mm, and  $g = 0.2$  mm.

## 3. Results and Discussion

In order to fully understand the proposed triband antenna, the key parameters  $L_2$ ,  $W_2$ , and  $W_6$  are selected to investigate their effects on the impedance bandwidth. The effects of  $W_2$  on the impedance bandwidth of the proposed antenna are shown in Figure 2. It is observed from the figure that the center frequency of the lower WLAN band at 2.4 GHz shifts from 2.5 GHz to 2.42 GHz, which can be tuned within a wide frequency range. In this case, the other two resonance frequencies are slightly changed. This is because the increased  $W_2$  increases the total length of the ML and hence extends the resonance length which makes the 2.4 GHz WLAN band move to the low frequency. Moreover, the ML is connected to the partial ground plane, which may affect the current distribution on the partial ground plane, which, in turn, slightly affects resonance characteristic of the TSP. Thus, the WiMAX band at 3.5 GHz has a slight fluctuation.

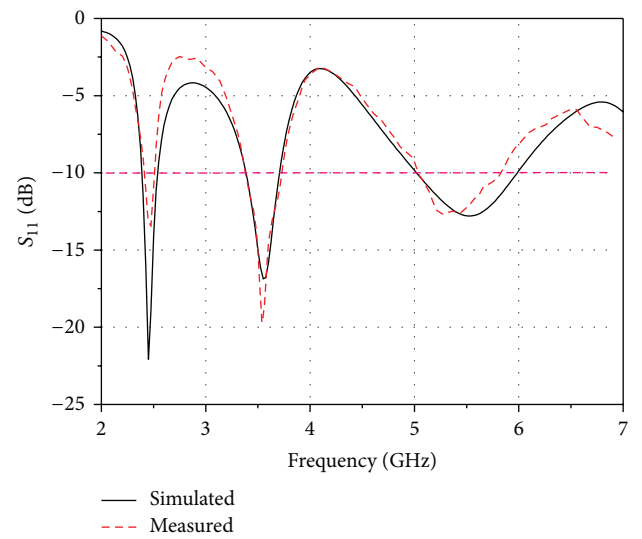
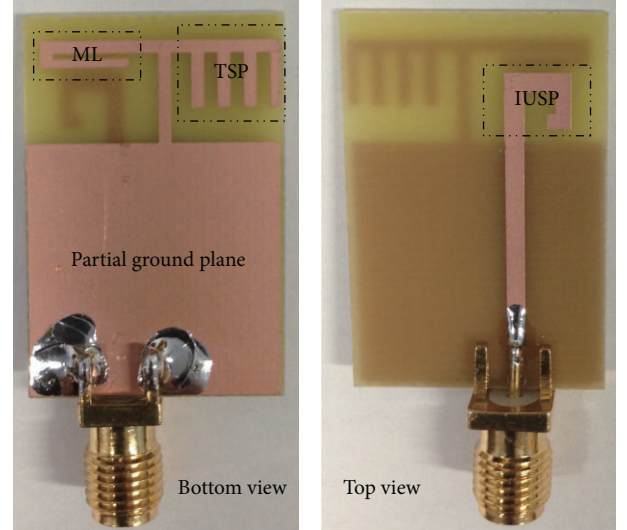
Figure 3 depicts the parameter effects on the impedance bandwidth with varying  $L_2$ . It can be seen from Figure 3 that the resonance frequency at 3.5 GHz moves to the low frequency with an increase of  $L_2$  ranging from 3.7 mm to 4.7 mm. Additionally, the 2.4 GHz WLAN band also slightly moves to the low frequency, which is due to the fact that the TSP might affect the ML via the common partial ground plane. The increased  $L_2$  not only extends the resonance length of the toothbrush-shaped patch but also changes the current distribution on the partial ground plane. Thus, we can conclude that TSP mainly determines the resonance frequency of 3.5 GHz WiMAX band.

Figure 4 illustrates the performance of the parameter  $W_6$ . It is observed that the upper WLAN band at 5.5 GHz moves to the low frequency with an increase of  $W_6$ . As  $W_6$  increases from 1.8 mm to 2.8 mm, the center frequency of



the upper WLAN band moves from 5.55 GHz to 5.15 GHz. This is because the increased  $W_6$  prolongs the total length of IUSP and hence increases the current path on the IUSP. Therefore, the center resonance frequency shifts to the low frequency. In addition, the impedance bandwidth of the highest resonance frequency becomes narrower with the increment of  $W_6$ . When  $W_6$  is equal to 1.8 mm, the upper WLAN band has a bandwidth of 1 GHz, which can cover the entire 5.15–5.825 GHz WLAN band.

In order to verify the performance of the proposed tri-band antenna, the designed antenna has been optimized, manufactured, and measured. The phototype of the fabricated antenna is shown in Figure 5. The measured  $S_{11}$  of the proposed tri-band antenna, as shown in Figure 6, is obtained by using Agilent N5224A vector network analyzer. It can



be seen that the proposed antenna has three resonance frequencies at 2.4 GHz, 3.5 GHz, and 5.5 GHz, which can cover the lower WLAN and WiMAX and the upper WLAN bands for  $S_{11} < -10$  dB. The bandwidths of the proposed antenna at the desired bands are 140 MHz, 310 MHz, and 840 MHz, respectively. On the other hand, the measured  $S_{11}$  agrees well with the simulated one, which helps to validate the effectiveness of the HFSS simulation. However, there are some deficiencies between the measured  $S_{11}$  and the simulated one, which may be caused by the fabrication tolerance and manual welding inaccuracies. The radiation patterns at 2.45 GHz, 3.5 GHz, and 5.5 GHz of the proposed tri-band antenna are obtained in an anechoic chamber, as shown in Figure 7. We can see that the proposed tri-band antenna can provide nearly omnidirectional radiation patterns in the  $H$ -plane and a figure-of-eight radiation pattern in

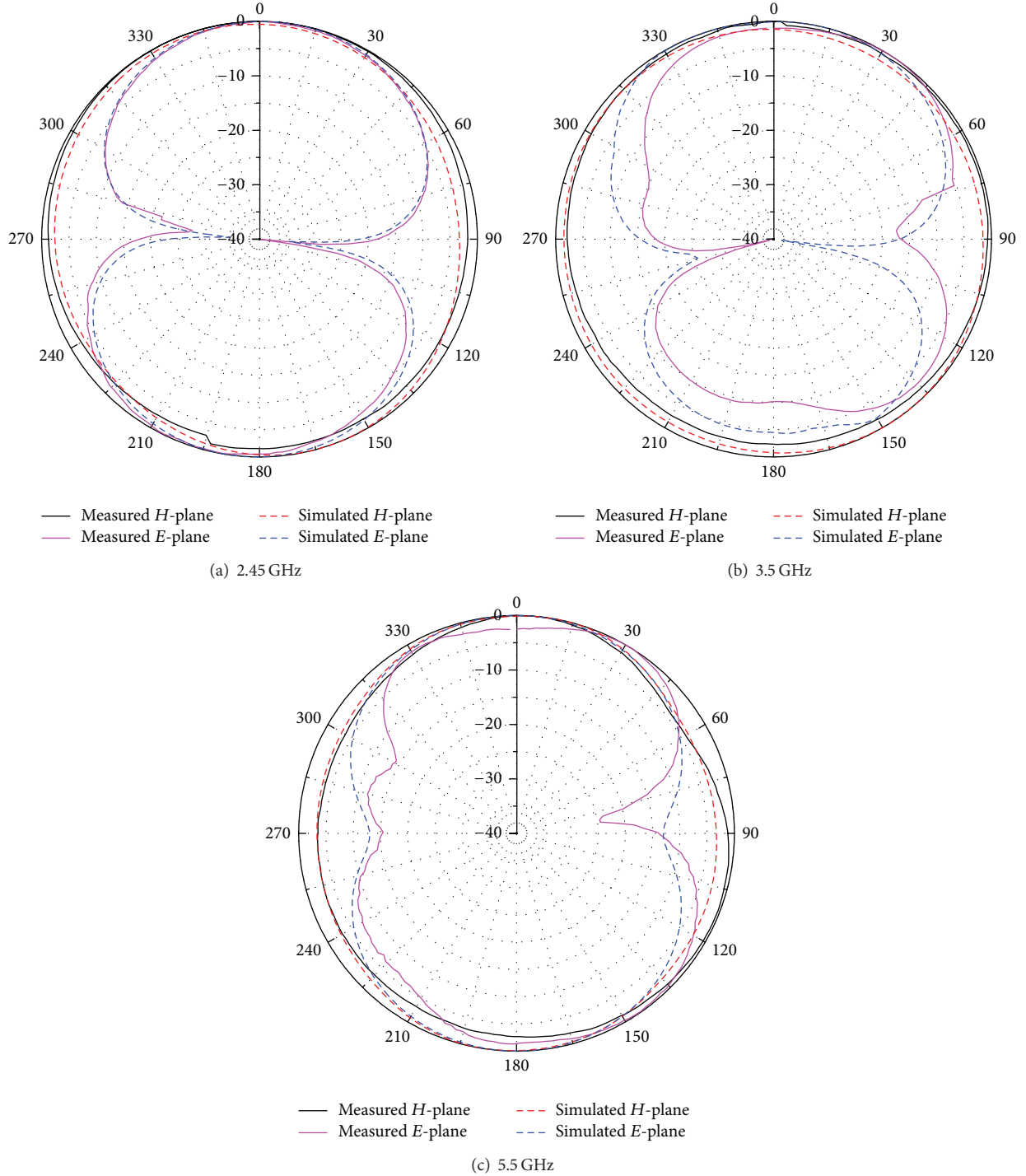


FIGURE 7: Radiation patterns of the proposed tri-band antenna.

the  $E$ -plane. The gains are obtained by comparing the proposed antenna with a standard horn antenna in an anechoic chamber. The peak gains at the 2.45 GHz, 3.5 GHz, and 5.5 GHz are 1.3 dBi, 2.2 dBi, and 3.0 dBi, respectively.

Table 1 compares the proposed antenna with previously proposed multiband antennas with respect to the size and the operating bands. We note that a few previously

proposed antennas can provide triple bands to cover the 2.4/3.5/5.2/5.5/5.8 GHz. Although some of the early reported antennas have smaller sizes than our proposed antenna [1, 6, 11], they cannot cover all the above mentioned operating bands. As for our proposed antenna with an excellent triple band characteristic, it has a smaller size than those of the previously proposed triple antennas in [4, 9].

TABLE 1: Comparisons of several existing multiband antennas.

References	Dimensions	Operating bands
[1]	17 × 12	2.4/5.8 GHz
[3]	22 × 29	2.4/3.5/5.2/5.8 GHz
[6]	11 × 6.7	5.8 GHz
[9]	38 × 25	2.4/3.5/5.2/5.5/5.8 GHz
[11]	17 × 12	3.5/5.8 GHz
Proposed antenna	30 × 20	2.4/3.5/5.2/5.5/5.8 GHz
[2]	40 × 20	2.4/5.2/5.8 GHz
[4]	37 × 18	2.4/3.5/5.2/5.5/5.8 GHz
[7]	30 × 50	2.4/5.2/5.8 GHz
[8]	38 × 30	2.4/5.2/5.8 GHz
[10]	40 × 20	2.4/5.2/5.8 GHz
[12]	20 × 35	2.4/5.5/5.8 GHz

## 4. Conclusion

A compact microstrip-fed triband monopole antenna has been proposed and its performance has been investigated both numerically and experimentally. The toothbrush-shaped patch, meander line, and inverted U-shaped patch have been employed to generate the desired 2.4 GHz, 3.5 GHz, and 5.5 GHz bands for WLAN and WiMAX communication applications. The proposed antenna has a small size and can provide triple wide operating bands. The numerical and experimental results demonstrated that the designed triband antenna can provide three tunable operating bands and good omnidirectional radiation patterns, which makes it suitable for integrating into portable devices.

## Conflict of Interests

The authors declare that there is no conflict of interests regarding the publication of this paper.

## Acknowledgments

This work was partially supported by a grant from Pre-Research Fund of the 12th Five-Year Plan (no. 4010403020102) and Fundamental Research Funds for the Central Universities (nos. HEUCFD1433, HEUFCF1508).

## References

- [1] Y. Li, W. Li, and Q. Ye, "A compact asymmetric coplanar strip-fed dual-band antenna for 2.4/5.8 GHz wlan applications," *Microwave and Optical Technology Letters*, vol. 55, no. 9, pp. 2066–2070, 2013.
- [2] X. L. Sun, L. Liu, S. W. Cheung, and T. I. Yuk, "Dual-band antenna with compact radiator for 2.4/5.2/5.8 GHz WLAN applications," *IEEE Transactions on Antennas and Propagation*, vol. 60, no. 12, pp. 5924–5931, 2012.
- [3] A. Mehdipour, A.-R. Sebak, C. W. Trueman, and T. A. Denidni, "Compact multiband planar antenna for 2.4/3.5/5.2/5.8-GHz wireless applications," *IEEE Antennas and Wireless Propagation Letters*, vol. 11, pp. 144–147, 2012.
- [4] H. Zhai, Z. Ma, Y. Han, and C. Liang, "A compact printed antenna for triple-band WLAN/WiMAX applications," *IEEE Antennas and Wireless Propagation Letters*, vol. 12, pp. 65–68, 2013.
- [5] X. D. Yang, Y. S. Li, and C. Y. Liu, "A toothbrush-shaped patch antenna for millimeter-wave communication," *Journal of Electromagnetic Waves and Applications*, vol. 23, no. 1-2, pp. 31–37, 2009.
- [6] C.-P. Lai, S.-C. Chiu, and S.-Y. Chen, "Miniaturization of CPW-fed slot antennas using reactive terminations and truncated bilateral ground plane," *IEEE Antennas and Wireless Propagation Letters*, vol. 11, pp. 1072–1075, 2012.
- [7] C.-Y. Huang and E.-Z. Yu, "A slot-monopole antenna for dual-band WLAN applications," *IEEE Antennas and Wireless Propagation Letters*, vol. 10, pp. 500–502, 2011.
- [8] K. G. Thomas and M. Sreenivasan, "Compact triple band antenna for WLAN/WiMAX applications," *Electronics Letters*, vol. 45, no. 16, pp. 811–813, 2009.
- [9] J. Pei, A.-G. Wang, S. Gao, and W. Leng, "Miniaturized triple-band antenna with a defected ground plane for WLAN/WiMAX applications," *IEEE Antennas and Wireless Propagation Letters*, vol. 10, pp. 298–301, 2011.
- [10] S. Verma and P. Kumar, "Compact triple-band antenna for WiMAX and WLAN applications," *Electronics Letters*, vol. 50, no. 7, pp. 484–486, 2014.
- [11] A. Khaleghi, "Dual band meander line antenna for wireless LAN communication," *IEEE Transactions on Antennas and Propagation*, vol. 55, no. 3, pp. 1004–1009, 2007.
- [12] Y. Li, W. Li, and R. Mittra, "A compact ACS-FED dual-band meandered monopole antenna for WLAN and WiMAX applications," *Microwave and Optical Technology Letters*, vol. 55, no. 10, pp. 2370–2373, 2013.
- [13] Y. S. Li, X. D. Yang, Y. Bai, and T. Jiang, "Dual-band antenna handles WLAN/WiMAX," *Microwaves & RF*, vol. 50, no. 1, pp. 80–88, 2011.

## Research Article

# A Low-Profile and Compact Split-Ring Antenna with Horizontally Polarized Omnidirectional Radiation

Kittima Lertsakwimarn,<sup>1</sup> Chuwong Phongcharoenpanich,<sup>1</sup> and Takeshi Fukusako<sup>2</sup>

<sup>1</sup>*Faculty of Engineering, King Mongkut's Institute of Technology Ladkrabang, 1, Chalongkrung Road, Ladkrabang, Bangkok 10520, Thailand*

<sup>2</sup>*Graduate School of Science and Technology, Kumamoto University, 2-39-1 Kurokami, Chuo-ku, Kumamoto 860-8555, Japan*

Correspondence should be addressed to Kittima Lertsakwimarn; wimand.mai@gmail.com

Received 25 August 2014; Accepted 22 October 2014

Academic Editor: Guo Qing Luo

Copyright © 2015 Kittima Lertsakwimarn et al. This is an open access article distributed under the Creative Commons Attribution License, which permits unrestricted use, distribution, and reproduction in any medium, provided the original work is properly cited.

This paper presents a low-profile and compact printed antenna having an omnidirectional radiation pattern with horizontal polarization to the ground. The proposed antenna consists of an inner small fed ring, an outer coupled split ring, and a ground plane. The overall dimension of the proposed antenna is  $45\text{ mm} \times 50.5\text{ mm} \times 11.6\text{ mm}$  ( $0.138\lambda_0 \times 0.155\lambda_0 \times 0.036\lambda_0$ ). The  $-10\text{-dB}$   $|S_{11}|$  of the antenna covers the 920-MHz RFID band, and the gain is about 1.45 dBi in the parallel direction to the ground plane. The measured results show good agreements with the simulated results. Furthermore, the reasons for the low-profile structure and the omnidirectional radiation pattern are also discussed.

## 1. Introduction

Antennas with horizontally polarized omnidirectional radiation pattern in the azimuth plane can be applied to many applications such as base stations and wireless communications. Such antennas are useful for, especially, polarization diversity being combined with vertically polarized omnidirectional antennas. The Alford loop antenna in the wire type was firstly reported to achieve an omnidirectional horizontal polarization [1]. Several modifications of the Alford loop antenna have been presented in [2, 3]. Other techniques for achieving omnidirectional pattern and horizontal polarization have also been studied. For example, four flag-shaped radiators are connected to four tapered strip lines terminated with a small circular patch at the centers on both sides of a substrate [4]. A series-fed array of loop antennas, which consists of four  $\mu$ -negative transmission lines (MNG-TL), was presented in [5]. However, many wireless devices require compact and light weight antenna elements with a low-profile structure [6].

Low-profile antennas installed on a back conductor can effectively reduce the electrical effect from backing material such as IC-chip, electrical circuits, and coupling with other

antennas [7]. Many low-profile antennas, such as disk loaded monopoles, tend to be vertically polarized radiations [6–11]. In [6], a loop structure can be miniaturized by using inductors. A loop-shaped inverted-F wire antenna (LIFA) has been presented in [9]. In [10], a vertically polarized cavity-backed composite slot loop antenna (CBCSLA) with omnidirectional radiation in the horizontal plane having extremely small height is presented. An inductively coupled capacitively loaded monopole antenna (ICCLMA) consisting of two metal layers, a feeding pin, and a shorting pin has been presented for achieving a high-gain, low-profile, and miniaturized characteristics with vertically polarized omnidirectional radiation [11]. In [8], a folded monopole antenna with capacitively coupled parasitic elements in the same plane is studied. However, as far as the authors know, no research has studied the compact and low-profile antenna having horizontally polarized omnidirectional radiation pattern.

Small antennas such as short dipoles or small loops have usually small resistance and large reactance components in impedance. Therefore, it is difficult for such antennas to be matched to the required impedance such as  $50\Omega$  [12]. Several small antennas with impedance matching techniques have been reported considering the above situations of

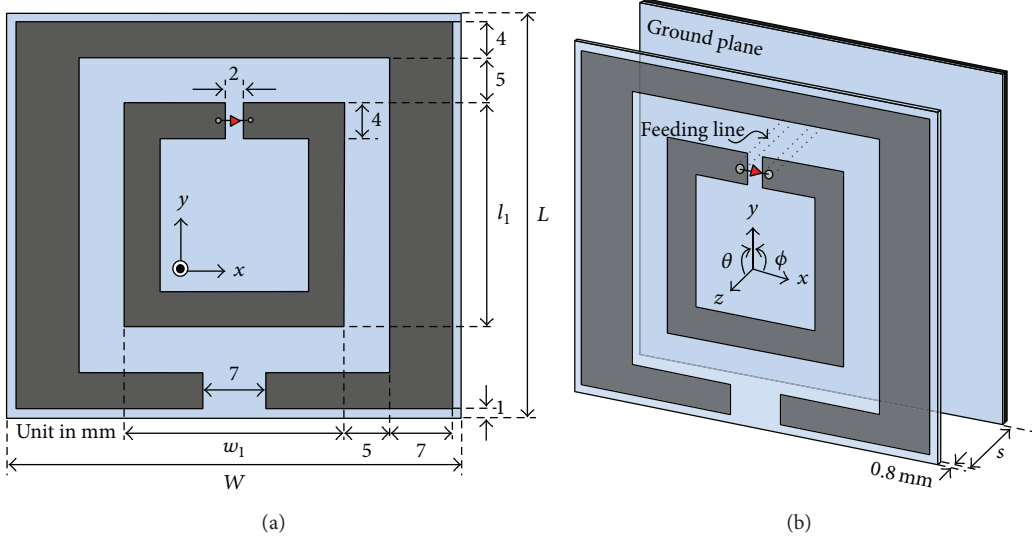


FIGURE 1: Geometry of the proposed antenna with ground plane: (a) front view and (b) perspective view.

impedance. A small loop antenna is a simple structure to achieve horizontally polarized omnidirectional radiation pattern with a uniform current distribution acting as a magnetic dipole. However, it is still faced with a difficulty in impedance matching because the small loop has small radiation resistance and large reactance [5, 13]. For solving this problem, printed split-ring antennas (SRAs) consisting of a small inner fed ring and an outer coupled split ring element are presented to match the impedance [14–16]. However, these antennas have neither a ground plane nor a backing conductor.

In this paper, a compact, planar, and low-profile SRA having a ground plane is proposed for radiating horizontal polarization in omnidirection. With the advantages of low-profile structure, a low-profile polarization diversity antenna can be achieved by combining the SRA with a low-profile vertically polarized monopole antenna for base station and RFID reader applications [17]. The performances of SRA with and without ground plane are demonstrated, and the mechanisms for the performances are also explained by observing the electric field (e-field) distribution.

## 2. Antenna Structure

The proposed antennas are designed and simulated using the CST MW Studio [18] throughout this paper. Figure 1 shows the proposed antenna structure consisting of a substrate, parallel feeding lines, and a ground plane. On the substrate, a fed inner ring and a coupled outer split ring are printed on a dielectric substrate of Arlon Diclad522 ( $\epsilon_r = 2.6$ ,  $\tan \delta = 2.0 \times 10^{-4}$ ) with 0.8 mm thickness. The dimensions are 45 mm ( $0.138\lambda_0$ ) in length ( $L$ ) and 50.5 mm ( $0.155\lambda_0$ ) in width ( $W$ ). The length and width of the inner and outer rings are optimized so as to resonate at the UHF RFID band around 920 MHz. The dimensions of the proposed antenna with and without ground plane are shown in Table 1. The SRA structure can reduce the overall size of the antenna because

TABLE 1: The structural parameters.

Parameter	Without GND	With GND
$W$	50.0 mm	50.5 mm
$L$	45.5 mm	45.0 mm
$w_1$	24.0 mm	25.0 mm
$l_1$	25.5 mm	24.5 mm

the capacitive coupling between the two rings makes the resonance at a low frequency [7, 19]. In Figure 1, a ground plane with the same size as the substrate has been installed. The air interval  $s$  between the substrate and ground plane is chosen as 10 mm ( $0.036\lambda_0$ ) as shown in Figure 1(b) considering the impedance matching. When  $s > 10$  mm having the ground plane with the same dimension as the upper element substrate, the impedance bandwidth is narrower than 15 MHz, which is a sufficient value for some applications such as RFID and mobile telecommunications. The effects of variation in the size of ground plane and the air interval will be discussed in Section 5. In addition, we can sufficiently regard the antenna with  $s = 10$  mm as low profile. Furthermore, we can make sure that the vertical component is suppressed in such a situation that the vertical component may be easily radiated. Photographs of the fabricated antennas are shown in Figure 2. Since the ground plane of the antenna is small, a bazooka balun has been equipped to suppress the leakage current on the coaxial cable.

## 3. Results and Discussions

**3.1. Antenna without Ground Plane.** In this section, an SRA without the ground plane is considered with almost the same dimensions as shown in Table 1. The antenna is fed through the bazooka balun because the feeding point should be balanced. Figure 3 shows the simulated and measured results of  $|S_{11}|$ . The simulated and measured  $-10\text{-dB } |S_{11}|$

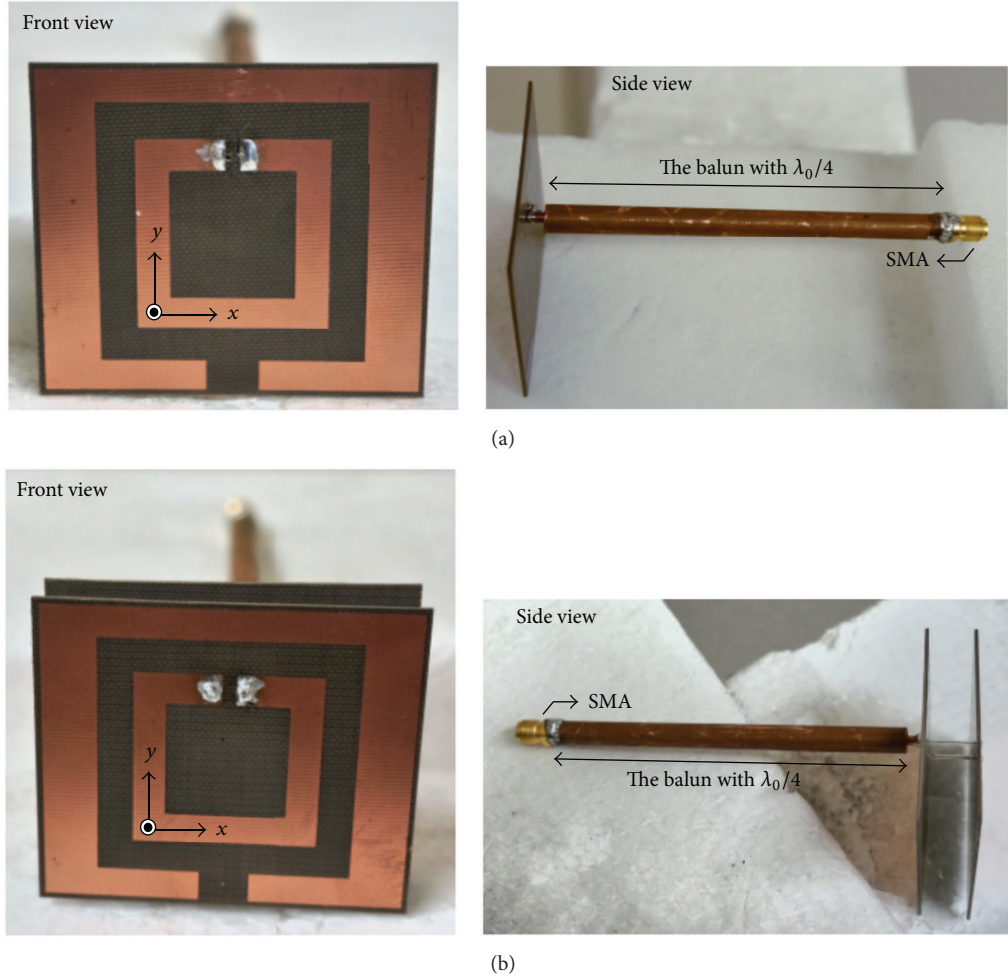


FIGURE 2: Photograph of fabricated prototype antenna (a) without ground plane and (b) with ground plane in perspective views and side views. Each structure has the feeding cable and the balun.

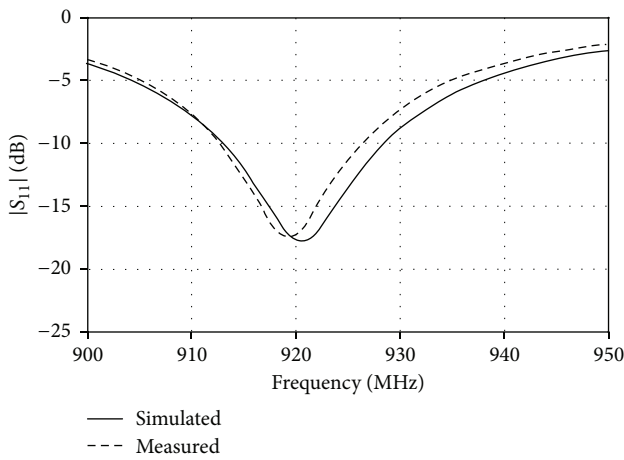


FIGURE 3: Simulated and measured  $|S_{11}|$  characteristics.

bands can cover the UHF RFID band (920–925 MHz) with 1.5% and 1.3% bandwidth, respectively.

Figure 4 shows the simulated and measured radiation patterns of  $E_\phi$  and  $E_\theta$  in the  $x$ - $y$ ,  $y$ - $z$ , and  $x$ - $z$  planes at

920 MHz. The simulated and measured cross-polarizations of  $E_\theta$  are lower by 20 dB than the co-polarizations of  $E_\phi$  in omnidirection of the  $x$ - $y$  and  $y$ - $z$  planes and has the maximum gain of 1.7 dBi along the  $+y$ -direction at 920 MHz. The antenna provides nearly omnidirectional patterns in these two planes.

**3.2. Antenna with Ground Plane.** The ground plane with the same size as the upper substrate is installed. The simulated and measured results of  $|S_{11}|$  are shown in Figure 5. Comparing Figure 5 with Figure 3, the simulated and measured bandwidth is decreased by 0.5% each after installing the ground plane. The simulated and measured gains along  $+y$ -direction at 920 MHz are 1.45 dBi and 1.1 dBi, respectively, and the radiation efficiency is 99%. However, as shown in Figure 6, the polarization and the radiation patterns are unchanged essentially from the pattern in Figure 4 as far as using this size of ground plane. Polarization is still parallel to the substrate and ground, and the radiation pattern is still omnidirectional. Moreover, the ground plane has only a small effect on the antenna gain. The mechanisms for obtaining the results can be explained from the e-field distributions in the next section.

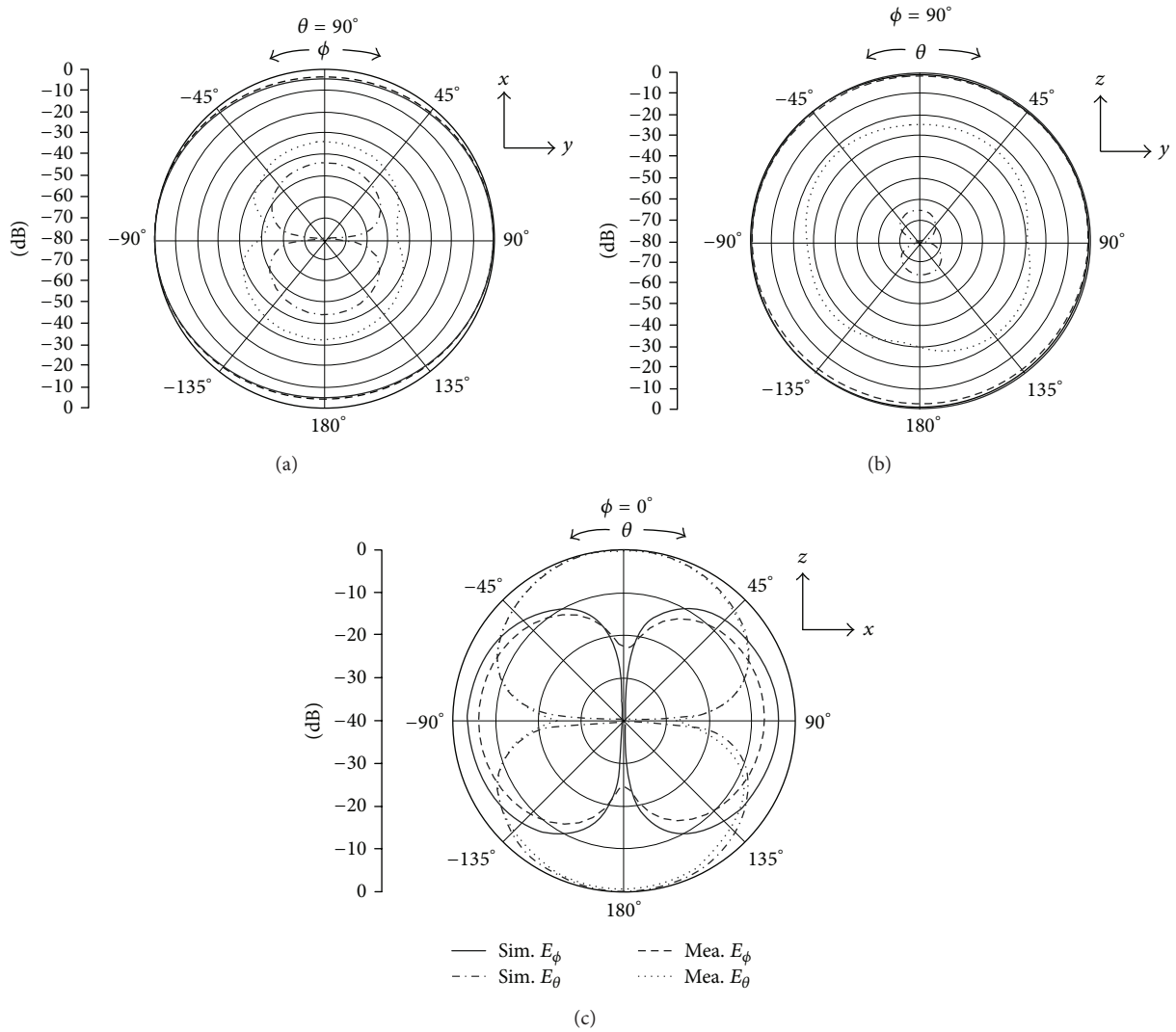


FIGURE 4: Radiation patterns at 920 MHz in the (a)  $x$ - $y$  plane, (b)  $y$ - $z$  plane, and (c)  $x$ - $z$  plane.

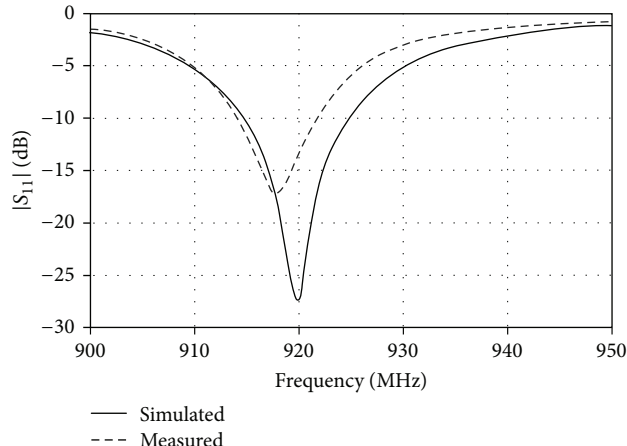
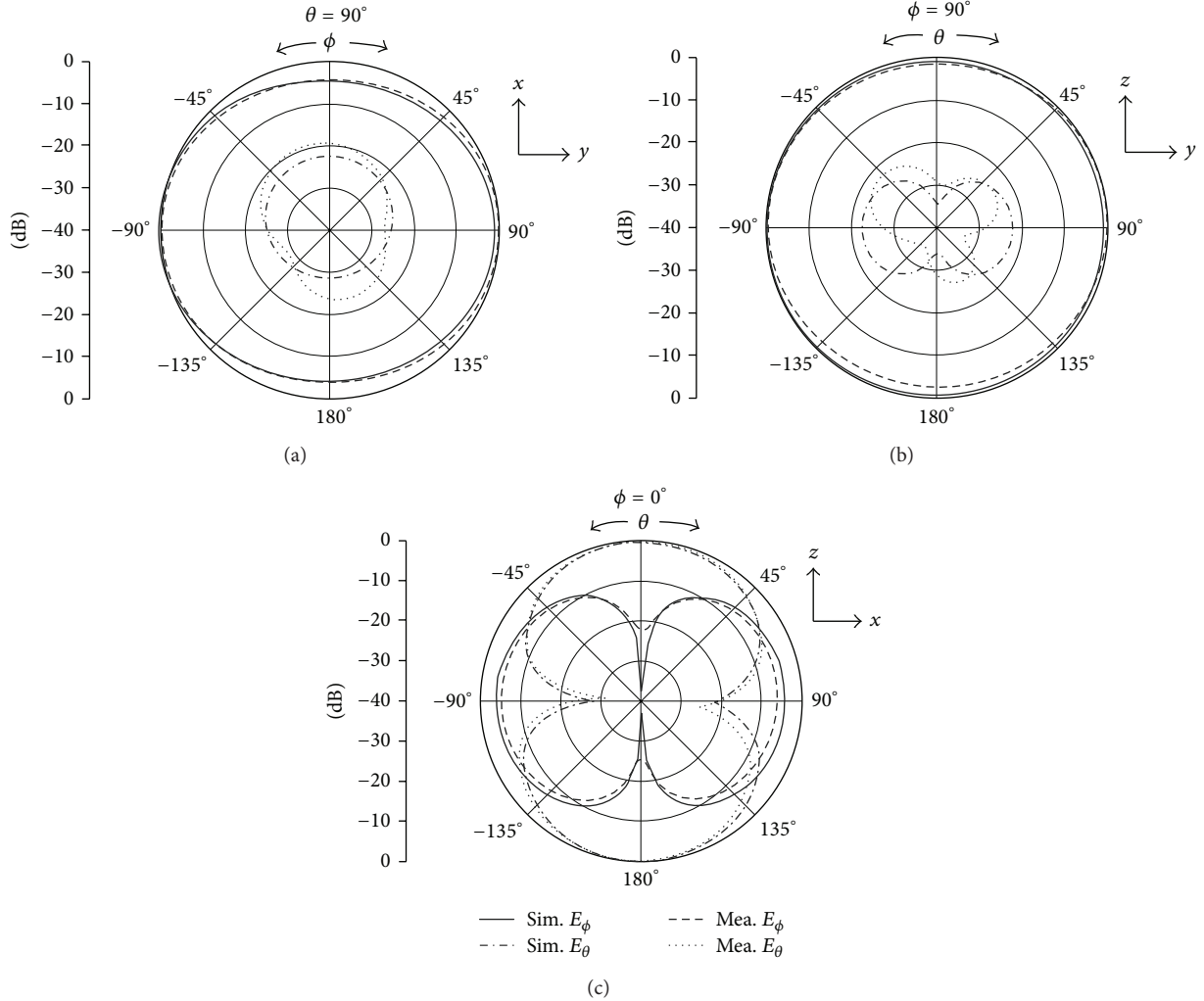


FIGURE 5: Simulated and measured  $|S_{11}|$  characteristics.

FIGURE 6: Radiation patterns at 920 MHz in the (a)  $x$ - $y$  plane, (b)  $y$ - $z$  plane, and (c)  $x$ - $z$  plane.

#### 4. Radiation Mechanism of Horizontally Polarized Omnidirectional Radiation Pattern

The radiation mechanism of horizontal polarization from the low-profile antenna is discussed in this section. From the results in Section 3, the proposed antennas with and without ground plane can radiate horizontal polarization to the ground or substrate. The mechanisms for the behavior are explained by discussing the distributions of e-field. The e-field distributions of the SRA without the ground plane in the  $x$ - $y$  plane are shown in Figure 7 at  $\omega t = 0^\circ$  and  $90^\circ$ , where the voltage at the feeding point is assumed to be  $V = V_0 \sin \omega t$ . For  $\omega t = 0^\circ$ , the e-field distribution on the SRA structure shows weak strength as shown in Figure 7(a). At  $\omega t = 90^\circ$ , the strongest e-field distribution can be found around in the two rings of the antenna. Many of the e-field vectors are parallel to  $x$ -direction as shown in Figure 7(b).

Next, the SRA structure with the ground plane is discussed. Figure 8 shows the e-field distribution in the  $x$ - $y$

plane at  $\omega t = 0^\circ$  and  $90^\circ$ . At  $\omega t = 0^\circ$ , the e-field shows asymmetric distribution to the  $y$ - $z$  plane but the strength is weak. At  $\omega t = 90^\circ$ , similar e-field distribution to that in Figure 7 can be observed as shown in Figure 8(b).

From the results, the antenna can radiate horizontal polarization either with or without the ground plane. Figure 9 shows the e-field distributions in the  $x$ - $z$  plane at distances of 20 mm from the center of substrate along the  $y$ -axis at  $\omega t = 0^\circ$  and  $90^\circ$ . At  $\omega t = 0^\circ$ , the e-field distribution is very weak as shown in Figure 9(a). At  $\omega t = 90^\circ$ , the e-field strength is symmetrical about the  $y$ - $z$  plane at the center of the ground, and the vertical  $z$ -components to the ground plane is mainly observed. Each e-field distribution in the left- or right-half part in Figure 9 has the opposite direction to the e-field in the other part. This results in canceling the radiation of vertical  $z$ -component in the far field. Therefore, the low-profile antenna can radiate horizontal polarization to the ground plane, even if the ground plane is installed.

The omnidirectional radiation pattern can be explained by the e-field distribution in the  $x$ - $y$  plane at  $\omega t = 90^\circ$  as shown in Figure 10. The e-field behavior is explained here

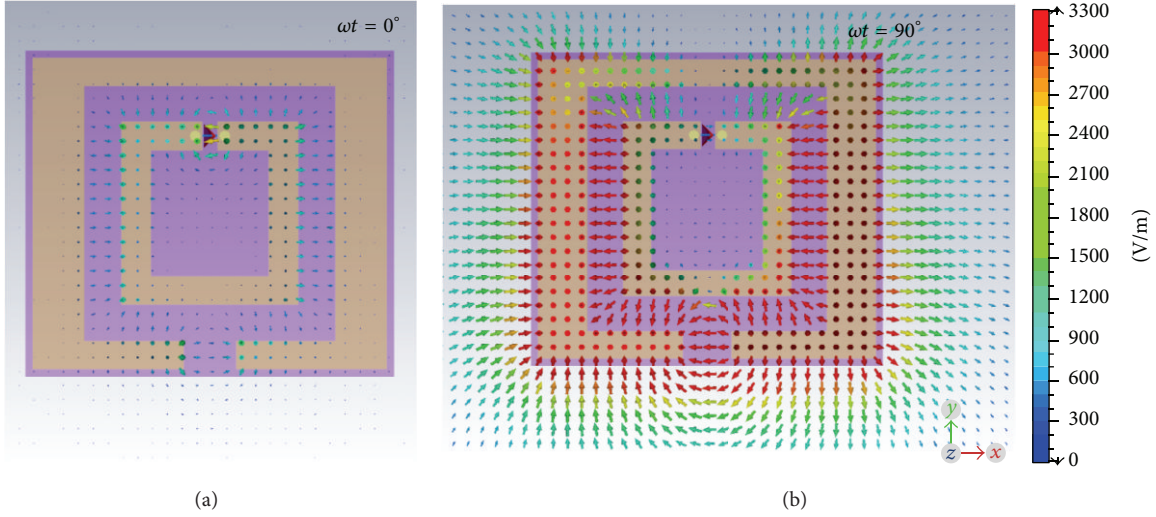


FIGURE 7: Electric field distributions of the antenna without ground plane in the  $x$ - $y$  plane on the element surface at 920 MHz with (a)  $\omega t = 0^\circ$  and (b)  $\omega t = 90^\circ$ .

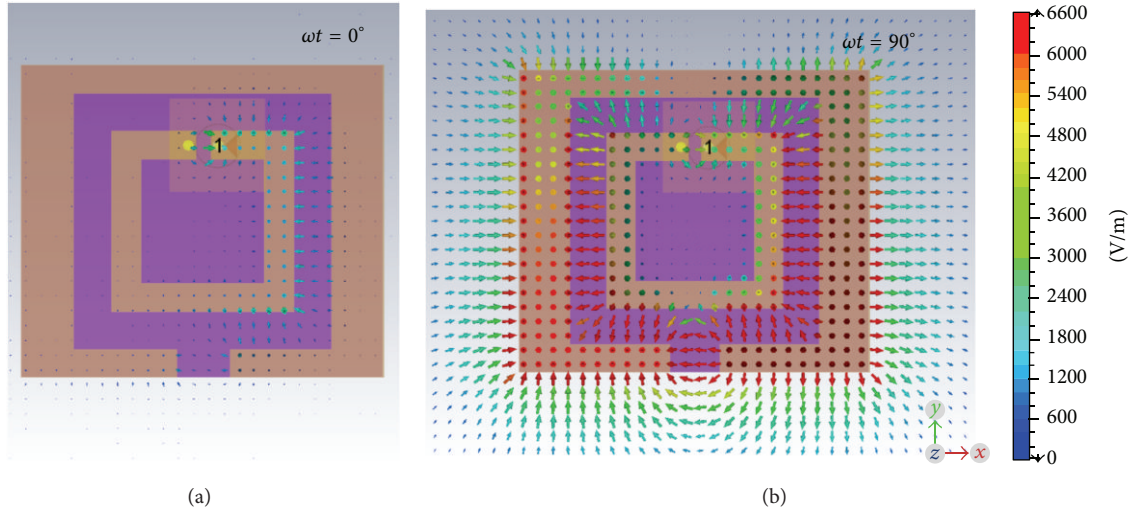


FIGURE 8: Electric field distributions of the antenna with ground plane in the  $x$ - $y$  plane on the element surface at 920 MHz with (a)  $\omega t = 0^\circ$  and (b)  $\omega t = 90^\circ$ .

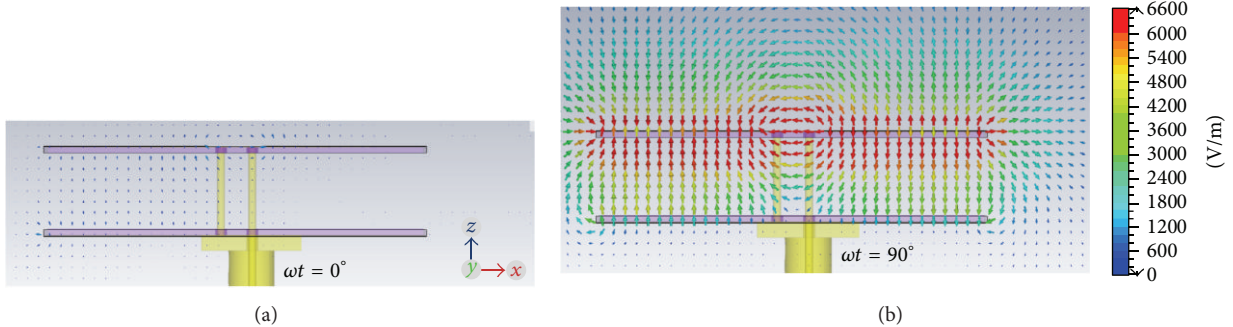


FIGURE 9: Electric field distribution in the  $x$ - $z$  plane at a distance of 20 mm from the center of substrate along the  $y$ -axis (a) at  $\omega t = 0^\circ$  and (b) at  $\omega t = 90^\circ$ .

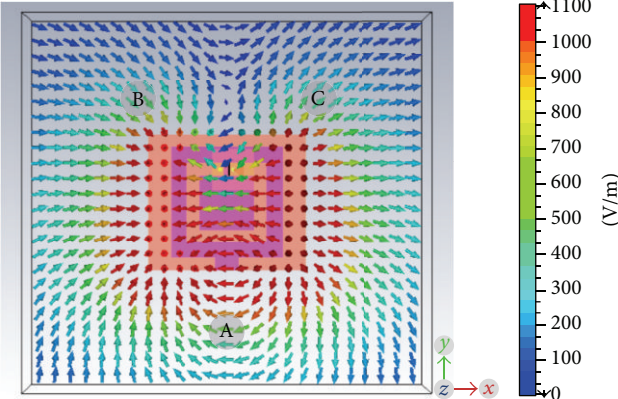


FIGURE 10: Electric field distribution in the  $x$ - $y$  plane at a distance of 7 mm above the surface of the upper substrate at  $\omega t = 90^\circ$ .

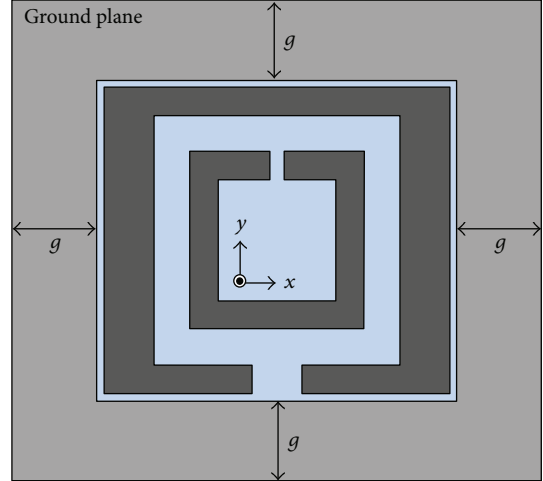


FIGURE 11: Direction of extension parameter  $g$ .

using the points A, B, and C in the figure. At the point A, strong e-field distribution directed parallel to  $x$ -direction is observed. The e-field at point B goes into the antenna element, and the e-field at C goes out of the element. The e-fields at points B and C are continuously connected in the far region. Given the fact that e-field is always continuous at a boundary, we can understand that the e-field distribution in Figure 10 has a continuous distribution in the far region surrounding the antenna. Considering the behaviors of e-field at the points A, B, and C, the e-field finally forms a vortex-like e-field distribution which is parallel to the  $x$ - $y$  plane at  $\omega t = 90^\circ$ ; however, showing such distribution in farther region is difficult because the simulating computer has an insufficient memory size. As a result, we can understand that the proposed antenna can have the horizontally polarized omnidirectional radiation pattern.

Similarly, we can observe the other omnidirectional radiation pattern in the  $y$ - $z$  plane. As seen in the Figures 8 and 10, we can find that the e-field is parallel to  $x$  direction around the antenna. On the other hand, as discussed with Figure 9, the radiation of e-field directed to  $\pm z$ -directions is cancelled in the far field. These behaviors contribute to radiating the omnidirectional pattern in the  $y$ - $z$  plane.

## 5. Effects of Structural Parameters

The proposed antenna has low-profile structure and horizontal polarization to the ground plane. This section discusses the effects on the antenna performance of the ground plane size and the air interval between the substrate and the ground plane.

**5.1. Effects of Ground Plane Size.** The effect of the ground plane size is discussed. The ground plane is extended in all directions in the  $x$ - $y$  plane by parameter  $g$  as shown in Figure 11. The simulated input impedance characteristics and  $|S_{11}|$  as a function of  $g$  are shown in Figure 12. From the results in Figure 12(a), the kink size gets gradually magnified when expanding  $g$ . As a result, we can see that the

ground plane size is affecting the impedance of the proposed antenna.

The simulated radiation patterns in the  $y$ - $z$  plane at the respective resonant frequencies with several  $g$  values are shown in Figure 13. With an increase in  $g$  from 0 to 40 mm, the radiation pattern becomes bidirectional pattern when  $g = 40$  mm as shown in Figure 13(a). At the same time, the cross-polarization in  $\pm z$ -direction ( $\phi = 90^\circ, 0^\circ, 180^\circ$ ) becomes strongest when  $g = 40$  mm but is still lower by 20 dB than the co-polarization as shown in Figure 13(b). Similarly, the cross-polarization in  $\pm y$ -direction is not changed significantly.

The e-field distribution in the  $x$ - $z$  plane with a larger ground size of  $g = 40$  mm is shown in Figure 14. Compared to Figure 9(b), the e-field is spread from the element edges with the extension of  $g$ . This effect of edge yields the e-field directed to diagonal directions in  $x$ - $z$  plane; therefore, the diagonal e-field arrows have components in  $z$ - and  $x$ -directions. The  $z$ -component of e-field around either the left or the right edge is directed to the opposite direction in the  $z$ -direction to the  $z$ -component around the other edge. This results in canceling out each other in the far field. Therefore, the vertical  $z$ -component to the ground is not radiated. On the other hand, with an increase in  $g$ , the  $x$  components of e-field around both edges gradually get stronger at close positions of  $< \lambda/4$  to the ground plane. Therefore, the input impedance is reduced and gets difficult to be matched well to  $50 \Omega$  as shown in Figure 12. For good impedance matching, the horizontal component should be reduced or the ring elements should not exist at a close position to the ground plane.

**5.2. Effects of Air Interval between the Substrates.** In the case of the antenna with the ground plane,  $|S_{11}|$  characteristics and radiation patterns are not changed significantly compared to the structure without ground plane. In Figure 15, the impedance characteristics without ground plane are shown with a dotted line at the right side of the Smith Chart circumference. When the ground plane is installed, the kink

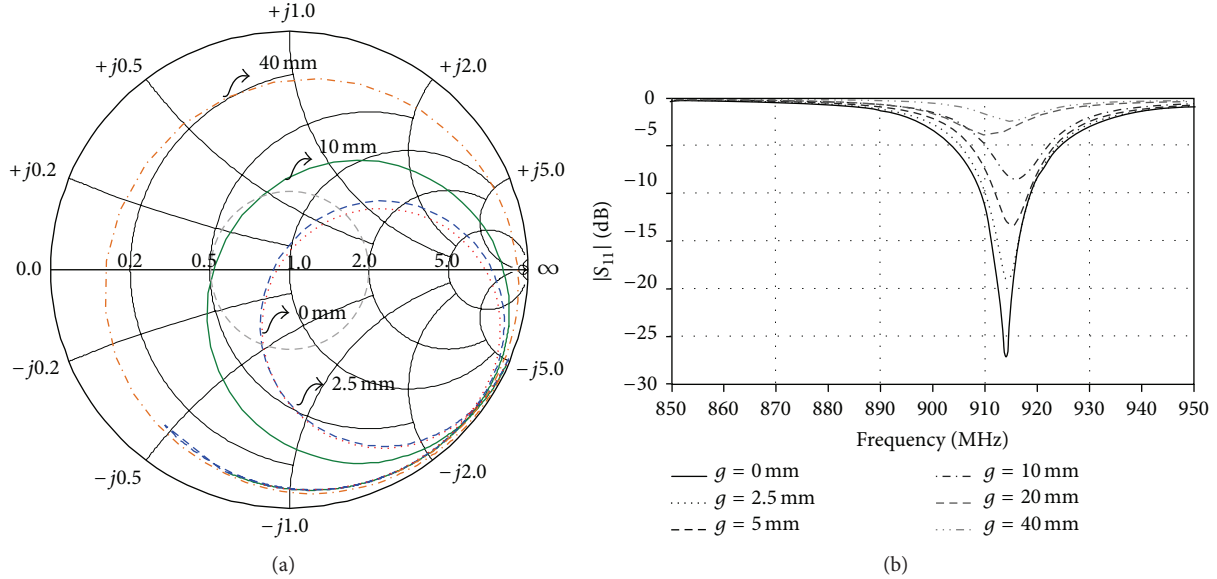


FIGURE 12: Simulated (a) input impedance characteristics and (b)  $|S_{11}|$  characteristics as a function of  $g$ .

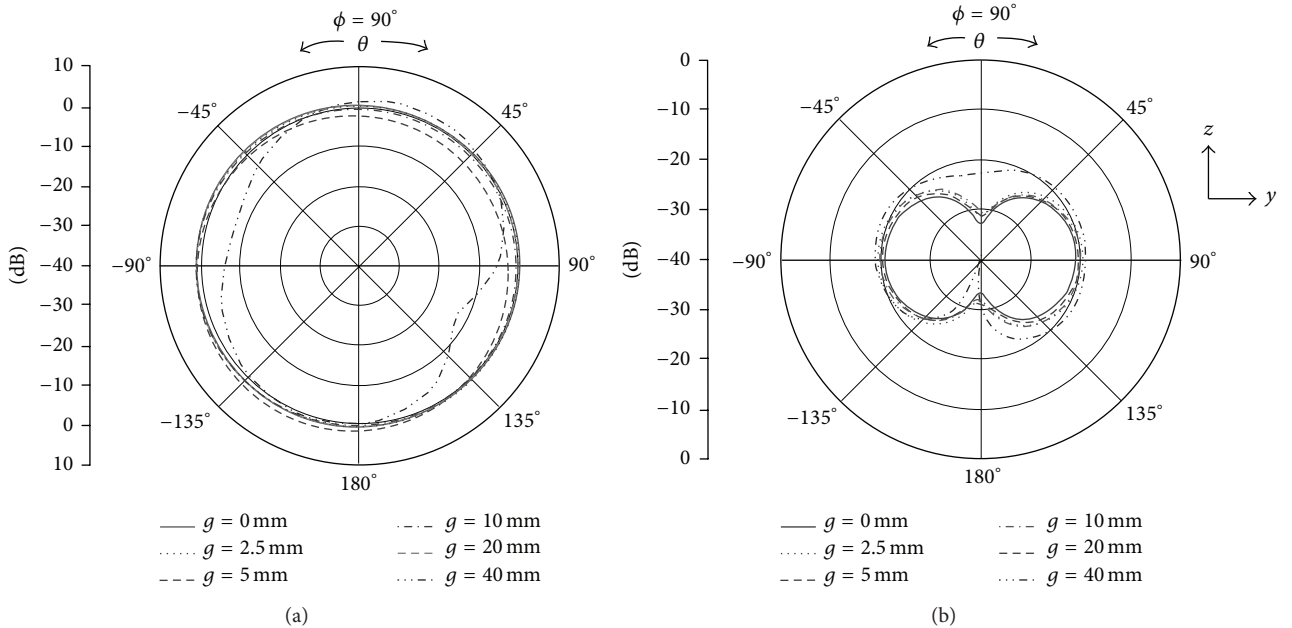


FIGURE 13: Simulated radiation patterns in the  $y$ - $z$  plane at respective resonant frequencies as a function of  $g$  (a) copolarization ( $E_\phi$ ), (b) cross-polarization ( $E_\theta$ ).

is shifted a little (solid line) along the circumference clockwise as shown in Figure 15. The shift is due to the two parallel feeding lines which have capacitive characteristics because, as shown with the dashed line in Figure 15, the impedance is close to the impedance with no ground plane when the parallel feeding lines are removed.

The effect of the air interval  $s$  is discussed keeping  $g = 0$  mm. The simulated input impedance characteristics are shown in Figure 16 as a function of  $s$ . When  $s = 0$  mm, the input impedance is too small resulting in the small kink

around the circumference of the Smith Chart (dotted line). When the  $s$  is increased from 3 mm to 13 mm, the kink becomes larger to achieve  $VSWR < 2$  around the resonant frequency after being shifted clockwise along the circumference of the Smith Chart. Figure 17 shows the simulated radiation patterns in the  $y$ - $z$  plane at the respective resonant frequencies of 1489, 887, 913, 924, and 898 MHz with an increase in  $s$  from 0 to 13 mm; however, the pattern is not changed significantly in the range from  $s = 3$  to 10 mm. The co- and cross-polarizations are not significantly changed

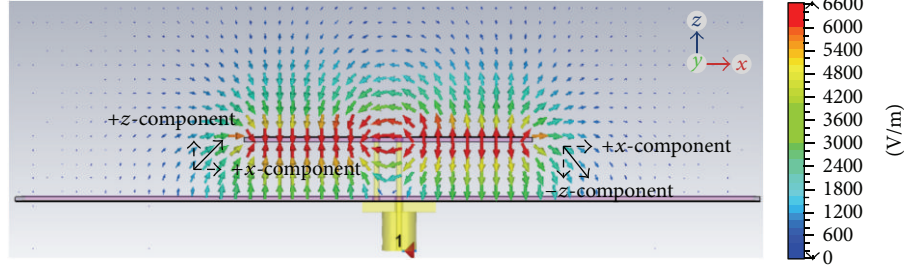


FIGURE 14: Electric field distribution in the  $x$ - $z$  plane at distances of 20 mm from the center of substrate along the  $y$ -axis at  $\omega t = 90^\circ$  for  $g = 40$  mm.

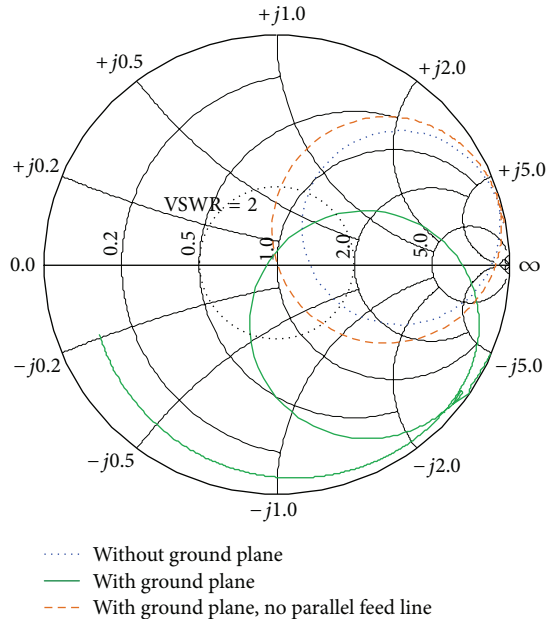


FIGURE 15: Effect of the ground and the parallel feeding line on the simulated input impedance characteristics.

except when  $s = 0$  mm. As a result, the impedance is not sensitive to  $s$  in the range of around 3 to 10 mm, and the low-profile structure is available in this range. This is because, as discussed in Section 4, the contribution to radiation of the e-field from the interval is finally canceled out. Considering the e-field behavior in the interval, this behavior is also the reason why the impedance is not sensitive to the difference between the two structures with and without the ground plane as shown in Figure 15. However, when  $s < 3$  mm, the horizontal components of e-field get weaker because they are parallel to the ground plane; therefore, the impedance is affected by such a small  $s$  value.

Finally, the effect of the environment surrounding the antenna is discussed. As far as  $s \geq 3$  mm, the SRA with a small ground plane size of  $g \leq 10$  mm has similar performance to the antenna without ground plane. Hence, the characteristics of SRA are not sensitive to the small ground plane. This indicates that the SRA can be installed on compact handset applications keeping the same characteristics as that without

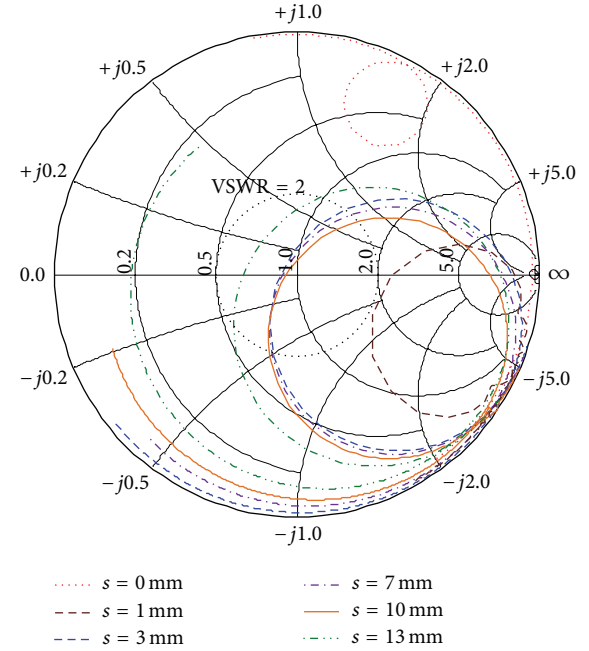


FIGURE 16: Simulated input impedance characteristics as a function of  $s$ .

ground plane. On the other hand, when  $g > 10$  mm (large ground planes) and  $s = 10$  mm, the antenna has small impedance around the resonant frequency with a large kink in Smith Chart, as shown in Figure 12(a). A decrease in  $s$  from 10 mm to 1 mm yields a smaller kink as shown in Figure 16. As shown in Figure 18 for  $g = 40$  mm and  $s = 1$  mm, as an extreme example, the input impedance can be matched well to  $50 \Omega$  with  $|S_{11}| < -10$  dB. The use of a larger ground plane has also advantages such as reducing the effects of the backing material on the antenna characteristics; however we have to note that the bandwidth is narrower in this case.

## 6. Conclusion

This paper has proposed a compact and low-profile SRA with horizontally polarized omnidirectional radiation pattern. The

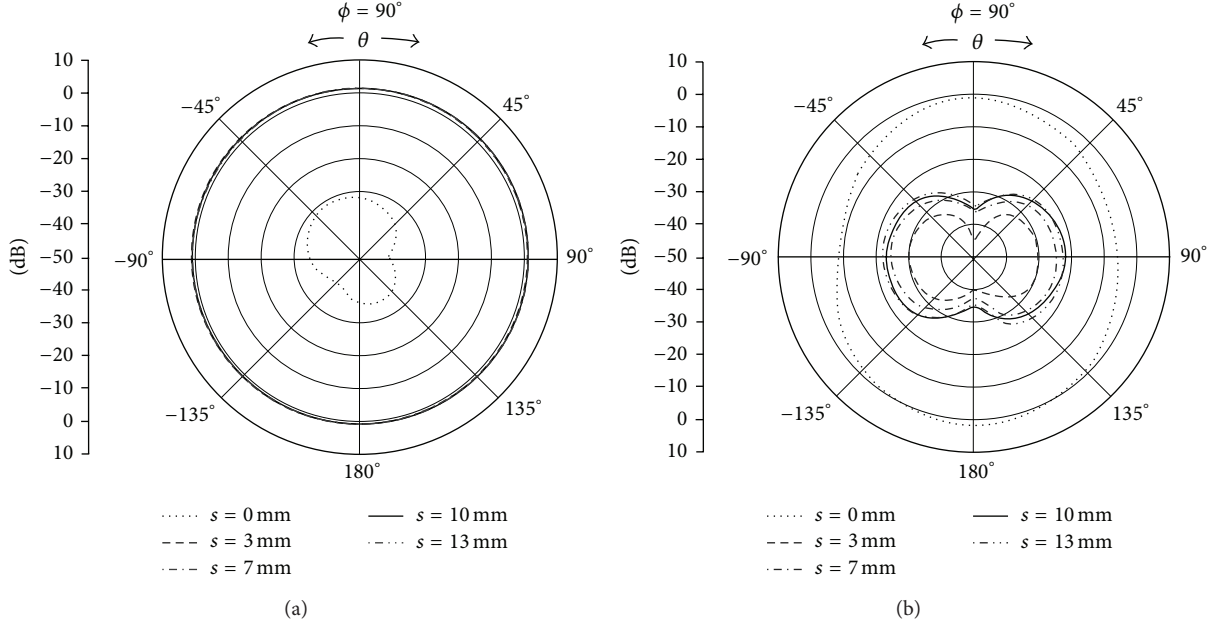


FIGURE 17: Simulated radiation patterns in the  $y$ - $z$  plane at respective resonant frequencies as a function of  $s$  (a) copolarization ( $E_\phi$ ) and (b) cross-polarization ( $E_\theta$ ).

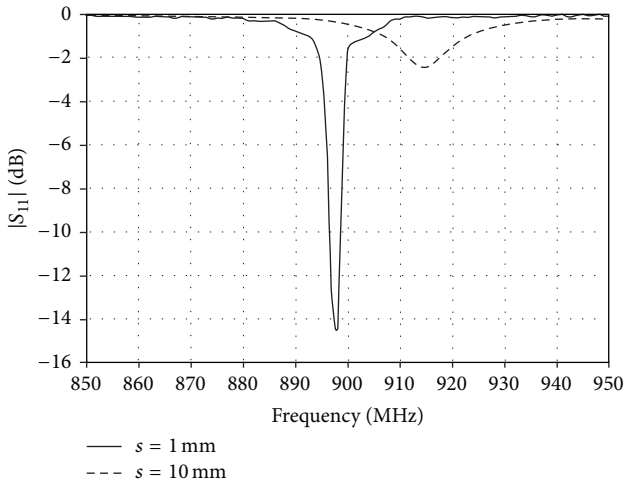


FIGURE 18: Simulated  $|S_{11}|$  characteristics for a large ground plane with  $g = 40$  mm.

simulated and measured results show that the antenna can radiate horizontal polarization and has approximately omnidirectional radiation pattern. The mechanism for achieving the low-profile structure and obtaining horizontally polarized omnidirectional radiation pattern can be explained by observing the electric field distributions.

## Conflict of Interests

The authors declare that there is no conflict of interests regarding the publication of this paper.

## Acknowledgment

This work is supported by the Thailand Research Fund (TRF) through the Royal Golden Jubilee Ph.D. Program under Grant no. PHD/0324/2552.

## References

- [1] A. Alford and A. G. Kandoian, "Ultra-high frequency loop antenna," *Transaction on the American Institute of Electrical Engineers (AIEE)*, vol. 59, no. 12, pp. 843–848, 1940.
- [2] C.-C. Lin, L.-C. Kuo, and H.-R. Chuang, "A horizontally polarized omnidirectional printed antenna for WLAN applications," *IEEE Transactions on Antennas and Propagation*, vol. 54, no. 11, pp. 3551–3556, 2006.
- [3] C.-H. Ahn, S.-W. Oh, and K. Chang, "A dual-frequency omnidirectional antenna for polarization diversity of MIMO and wireless communication applications," *IEEE Antennas and Wireless Propagation Letters*, vol. 8, pp. 966–969, 2009.
- [4] Y. Yu, F. Jolani, and Z. Chen, "A wideband omnidirectional horizontally polarized antenna for 4G LTE applications," *IEEE Antennas and Wireless Propagation Letters*, vol. 12, pp. 686–689, 2013.
- [5] K. Wei, Z. Zhang, Z. Feng, and M. F. Iskander, "A MNG-TL loop antenna array with horizontally polarized omnidirectional patterns," *IEEE Transactions on Antennas and Propagation*, vol. 60, no. 6, pp. 2702–2710, 2012.
- [6] D. H. Lee, A. Chauraya, Y. Vardaxoglou, and W. S. Park, "A compact and low-profile tunable loop antenna integrated with inductors," *IEEE Antennas and Wireless Propagation Letters*, vol. 7, pp. 621–624, 2008.
- [7] Y. Saito and T. Fukusako, "Low-profile and electrically small meander-line antenna using a capacitive feed structure," *IEEE*

*Antennas and Wireless Propagation Letters*, vol. 11, pp. 1281–1284, 2012.

- [8] J. Oh and K. Sarabandi, “Low profile vertically polarized omnidirectional wideband antenna with capacitively coupled parasitic elements,” *IEEE Transactions on Antennas and Propagation*, vol. 62, no. 2, pp. 977–982, 2014.
- [9] M. Kim and H. Arai, “Low-profile loop-shaped inverted-F wire antenna with dual-mode operation,” *IEEE Antennas and Wireless Propagation Letters*, vol. 7, pp. 62–65, 2008.
- [10] W. Hong and K. Sarabandi, “Low profile miniaturized planar antenna with omnidirectional vertically polarized radiation,” *IEEE Transactions on Antennas and Propagation*, vol. 56, no. 6, pp. 1533–1540, 2008.
- [11] J. Oh and K. Sarabandi, “Low profile, miniaturized, inductively coupled capacitively loaded monopole antenna,” *IEEE Transactions on Antennas and Propagation*, vol. 60, no. 3, pp. 1206–1213, 2012.
- [12] G. Breed, “Basic principles of electrically small antennas,” *Journal of High Frequency Electronics*, pp. 50–53, 2007.
- [13] C. A. Balanis, *Antenna Theory: Analysis and Design*, Wiley-Interscience, Hoboken, NJ, USA, 3rd edition, 2005.
- [14] M. Polivka, A. Holub, M. Vyhnanik, and M. Svanda, “Impedance properties and radiation efficiency of electrically small double and triple split-ring antennas for UHF RFID applications,” *IEEE Antennas and Wireless Propagation Letters*, vol. 12, pp. 221–224, 2013.
- [15] Y. J. Kim and H. M. Lee, “Electrically small square loop antenna with a capacitive split ring resonator cover structure,” *Microwave and Optical Technology Letters*, vol. 51, no. 3, pp. 831–835, 2009.
- [16] S.-H. Lim, Y.-C. Oh, H. Lim, Y.-S. Lee, and N.-H. Myung, “Analysis and design of a UHF RFID tag antenna with a split ring resonator,” in *Proceedings of the International Workshop on Antenna Proceedings (iWAT '08)*, pp. 446–449, Chiba, Japan, March 2008.
- [17] X. Quan and R. Li, “A broadband dual-polarized omnidirectional antenna for base stations,” *IEEE Transactions on Antennas and Propagation*, vol. 61, no. 2, pp. 943–947, 2013.
- [18] CST Microwave Studio, <http://www.cst.com/>.
- [19] K. Lertsakwimarn, R. Suwalak, and C. Phongcharoenpanich, “A compact loop antenna with parasitic split ring for UHF RFID application,” in *Proceedings of the Progress in Electromagnetics Research Symposium (PIERS '13)*, pp. 219–222, Taipei, Taiwan, March 2013.